IDŐJÁRÁS

QUARTERLY JOURNAL
OF THE HUNGARIAN METEOROLOGICAL SERVICE

CONTENTS

VOL. 126 * NO. 2 * APRIL – JUNE 2022

IDŐJÁRÁS

Quarterly Journal of the Hungarian Meteorological Service

Editor-in-Chief
LÁSZLÓ BOZÓ

Executive Editor
MÁRTA T. PUSKÁS

Editorial Office: Kitaibel P.u. 1, H-1024 Budapest, Hungary
P.O. Box 38, H-1525 Budapest, Hungary
E-mail: journal.idojaras@met.hu
Fax: (36-1) 346-4669

Indexed and abstracted in Science Citation Index Expanded^{TM} and Journal Citation Reports/Science Edition
Covered in the abstract and citation database SCOPUS®
Included in EBSCO's databases

Subscription by mail:
IDŐJÁRÁS, P.O. Box 38, H-1525 Budapest, Hungary
E-mail: journal.idojaras@met.hu

DOI:10.28974/idojaras.2022.2.1

IDŐJÁRÁS
Quarterly Journal of the Hungarian Meteorological Service
Vol. 126, No. 2, April – June, 2022, pp. 159–184

Joint examination of climate time series based on a statistical definition of multidimensional extreme

Tamás Szentimrey [1] and **Beatrix Izsák**[2, 3,*]

[1]*Varimax Limited Partnership, Budapest, Hungary*

[2]*Hungarian Meteorological Service,*
Kitabel Pál Street 1, H-1024, Budapest, Hungary

[3] *ELTE Faculty of Science,*
Doctoral School of Earth Sciences, Budapest, Hungary

**Corresponding author E-mail: izsak.b@met.hu*

(Manuscript received in final form March 25, 2022)

Abstract— The joint examination of the climate time series may be efficient methodology for the characterization of extreme weather and climate events. In general, the main difficulties are connected with the different probability distribution of the variables and the handling of the stochastic connection between them.

The first problem can be solved by the standardization procedures, i.e., to transform the variables into standard normal ones. For example, there are the Standardized Precipitation Index (SPI) series for the precipitation sums assuming gamma distribution, or the standardization of temperature series assuming normal distribution. In case of more variables, the problem of stochastic connection can be solved on the basis of the vector norm of the transformed variables defined by their covariance matrix.

We will present the developed mathematical methodology and some examples for its meteorological applications.

Key-words: climate time series, vector variables, multidimensional extreme, transformation of vector components, vector norm by matrix, correlation matrix, SPI (Standardized Precipitation Index), STI (Standardized Temperature Index), SPTI (Standardized Precipitation and Temperature Index), hypothesis testing, extreme subsystems

1. Introduction

In the case of joint examination of several climate time series, extreme values can no longer be interpreted by the simple concepts of maximum and minimum values. However, among the element sets or vectors, there may obviously be some that are considered natural, and there may be some that seem unusual to us. The latter can also be conceivable without any extraordinariness of the individual elements, but their co-occurrence can already be considered an extreme phenomenon. Moreover, it can be assumed that the examination of such multidimensional extremes is a more effective tool for examining and characterizing climate change than dealing only with one-dimensional cases.

We began to deal with this topic and the development of the mathematical foundations more than twenty years ago (*Szentimrey*, 1999), and we have carried out a number of such examinations during this time (*Szentimrey et al.*, 2014). Now we want to present a summary of the mathematical results and give some examples for their meteorological applications.

2. Problems of the concept of multidimensional extreme

2.1 Statistical model

Let $\mathbf{X}(t) = [X_1(t), \ldots, X_N(t)]^T$ $(t = 1,2, \ldots, n)$ be a multidimensional time series, which are totally independent and identically distributed probability vector variables. The distribution functions of the components are $F_j(x)$ $(j = 1,2, \ldots, N)$, the vector of expectations is $\mathrm{E}(\mathbf{X}(\mathrm{t})) = \mathbf{E} = [E_1, \ldots, E_N]^T$ $(t = 1,2, \ldots, n)$, and the vector of standard deviations is $\mathrm{D}(\mathbf{X}(\mathrm{t})) = \mathbf{D} = [D_1, \ldots, D_N]^T$ $(t = 1,2, \ldots, n)$.

2.2 "Basic" questions, problems

- The joint examination of the vector components may be efficient for the characterization of extreme events. In general the main difficulties are connected with their different probability distribution and the handling of the stochastic connection between them.
- Which vector variable can be considered extreme?
- How can be tested the null hypothesis of the identical distribution of the vector variables on the basis of the analysis of extremes?
- How can be explained the extremity by the subsystems of the components?

2.3 Transformation of the vector components

One of the problems is that the vector components have different probability distributions and scales. This, however, can be solved by some transformation procedure.
The transformed vector variables are

$$\mathbf{Z}(t) = \mathbf{h}(\mathbf{X}(t)) = [h_1(X_1(t)),\ldots,h_N(X_N(t))]^T \qquad (t = 1,2,..,n)\ ,$$

where we assume that, $\mathrm{P}\left(X_j(t) \in \left(a_j, b_j\right)\right) = 1$, and $h_j(x)$ is a strictly monotonically increasing function on interval $\left(a_j, b_j\right)$ $(j = 1,2,\ldots\ldots,N)$.

Remark 2.3.1

If the components were examined separately, the use of the variables $X_j(t)$ or $Z_j(t) = h_j\left(X_j(t)\right)$ $(t = 1,2,\ldots\ldots,n)$ would be equivalent in respect of extremity. However, at the joint examination it is important that none of the components play a dominant role, so the “similarity” of the distributions should be aimed.

2.4 Postulates to the definition of multidimensional extreme

Let $\mathbf{Z}(\mathrm{t}) = \mathbf{h}(\mathbf{X}(t))(t = 1,2,..,n)$ be transformed vector variables according to Section 2.3.

i. $\mathbf{X}(t_e)$ is extreme, i.e., extreme realization, if and only if $\mathbf{Z}(t_e) = \mathbf{h}(\mathbf{X}(t_e))$ is extreme. This postulate can be accepted because of the deterministic cause-and-effect relationship.

ii. Let us assume that, there exist $h_j(x)$ $(j = 1,2,\ldots\ldots,N)$, that fulfil $Z_j(t) = = h_j\left(X_j(t)\right) \in N(0,1)$, i.e., they are standard normal variables. Then, according to the above $\boldsymbol{X}(t_e)$ is extreme, if and only if $\mathbf{Z}(t_e) = = [\mathrm{Z}_1(t_e),\ldots,\mathrm{Z}_\mathrm{N}(t_e)]^\mathrm{T}$is extreme.

iii. Let us assume further that, the joint distribution of the vector components $Z_1(t),\ldots,Z_N(t)$ is also normal, i.e., $\mathbf{Z}(t) \in N(\mathbf{0},\mathbf{R})$, where $\mathbf{R} = \mathrm{E}(\mathbf{Z}(t)\mathbf{Z}(t)^\mathrm{T})$ is the correlation matrix assuming the existence of the inverse matrix $\mathbf{R}^{-1}$. Then the joint density function is $g(\boldsymbol{z}) = (2\pi)^{-\frac{N}{2}}|\mathbf{R}|^{-\frac{1}{2}}\exp\left(-\frac{1}{2}\ \mathbf{z}^\mathrm{T}\mathbf{R}^{-1}\mathbf{z}\right)$.

This means, the density function $g(\boldsymbol{z})$ is a strictly monotonous decreasing function of the $\boldsymbol{R}^{-1}$-norm $\|\mathbf{z}\|_{\mathbf{R}^{-1}} = (\mathbf{z}^\mathrm{T}\mathbf{R}^{-1}\mathbf{z})^{\frac{1}{2}}$. Consequently, $\boldsymbol{Z}(t_e)$ is extreme, if and only if $\|\mathbf{Z}(t_e)\|_{\mathbf{R}^{-1}} = \max\limits_{1\leq \mathrm{t} \leq \mathrm{n}} \|\mathbf{Z}(t)\|_{\mathbf{R}^{-1}}$.

2.5 Definition of the multidimensional extreme

In summary, the multidimensional extreme can be defined as follows.

Definition 2.5.1

Let $\mathbf{X}(t) = [X_1(t),\ldots.,X_N(t)]^T (t = 1,2,\ldots..,n)$ be totally independent and identically distributed probability vector variables.
Let us assume that $h_j(x)$ are strictly monotonous increasing functions on the intervals (a_j, b_j) where $\mathrm{P}\left(X_j(t) \in (a_j, b_j)\right) = 1$ $(j = 1,2,\ldots..,N)$.
Let us assume further that the components of the vector variables $\mathbf{Z}(t) = \mathbf{h}(\mathbf{X}(t)) = [h_1(X_1(t)),\ldots.,h_N(X_N(t))]^T$ $(t = 1,2,\ldots..,n)$ are standard normal, i.e., $Z_j(t) = h_j(X_j(t)) \in N(0,1)$ $(j = 1,2,..,N)$, and their common correlation matrix $\mathbf{R} = \mathrm{E}(\mathbf{Z}(t)\mathbf{Z}(t)^{\mathrm{T}})$ has the inverse matrix $\mathbf{R}^{-1}(t = 1,2,\ldots..,n)$.
Then, $\mathbf{X}(t_e)$ is extreme, if and only if $\|\mathbf{Z}(t_e)\|_{\mathbf{R}^{-1}} = \max\limits_{1\leq t\leq n} \|\mathbf{Z}(t)\|_{\mathbf{R}^{-1}}$, where $\|\mathbf{Z}(t)\|_{\boldsymbol{R}^{-1}} = (\mathbf{Z}(t)^{\mathrm{T}}\mathbf{R}^{-1}\mathbf{Z}(t))^{\frac{1}{2}}$ is the $\mathbf{R}^{-1}$-norm of vector variable $\mathbf{Z}(t)$.

3. Examples for the transformation of climate data series and standard indexes

Various type of climate data can be transformed for standard normal distributed variable on the basis of the following well known theorem.

Theorem 3.1

Let us assume that $\mathrm{P}\left(X_j(t) \in (a_j, b_j)\right) = 1$, moreover, the distribution function $F_j(x)$ of variable $X_j(t)$ is strictly monotonous increasing and continuous on the interval (a_j, b_j) $(j = 1,2,\ldots..,N)$. Then $h_j(x) = \Phi^{-1}(F_j(x))$ is also strictly monotonous increasing and continuous function on the interval (a_j, b_j), furthermore, $Z_j(t) = h_j(X_j(t)) \in N(0,1)$ $(j = 1,2,\ldots..,N)$, where $\Phi(x)$ is the standard normal distribution function.

Proof.

$$\mathrm{P}(Z_j(t) < z)=\mathrm{P}(h_j(X_j(t)) < z)=\mathrm{P}\left(\Phi^{-1}\left(F_j(X_j(t))\right) < z\right) = \mathrm{P}\left(F_j(X_j(t)) < \Phi(z)\right) =$$
$$= \mathrm{P}\left(X_j(t) < F_j^{-1}(\Phi(z))\right) = F_j\left(F_j^{-1}(\Phi(z))\right) = \Phi(z).$$

3.1 Annual precipitation sum

$X_1(t) \in \Gamma(p,\lambda) \qquad (t = 1,2,\ldots\ldots,n)$ and
$Z_1(t) = \Phi^{-1}\big(G(X_1(t))\big) \in N(0,1) \qquad (t = 1,2,\ldots\ldots,n)$,
where $G(x)$ notates the $\Gamma(p,\lambda)$ distribution function and $\Phi^{-1}(x)$ is the inverse of the standard normal distribution function. In fact, $Z_1(t)$ is the SPI (Standardized Precipitation Index) well known in meteorology for characterization of the drought events.

3.2 Annual mean temperature

$X_2(t) \in N(E_2,D_2) \qquad (t = 1,2,\ldots\ldots,n)$ and
$Z_2(t) = \Phi^{-1}\left(\Phi\left(\frac{X_2(t)-E_2}{D_2}\right)\right) = \frac{X_2(t)-E_2}{D_2} \in N(0,1) \quad (t = 1,2,\ldots\ldots,n)$,
where $\Phi\left(\frac{x-E_2}{D_2}\right)$ is the $N(E_2,D_2)$ distribution function. We defined this index as STI (Standardized Temperature Index).

3.3 Annual precipitation sum and mean temperature together

$\boldsymbol{X}(t) = [X_1(t),X_2(t)]^T \quad (t = 1,2,..,n)$ and the
SPI, STI indexes together are $\boldsymbol{Z}(t) = [Z_1(t),Z_2(t)]^T \qquad (t = 1,2,..,n)$.

Definition 3.3.1

The SPTI (Standardized Precipitation and Temperature Index) can be defined as

$$\|\mathbf{Z}(t)\|_{\mathbf{R}^{-1}} = (\mathbf{Z}(t)^{\mathrm{T}}\mathbf{R}^{-1}\mathbf{Z}(t))^{\frac{1}{2}} \qquad (t = 1,2,..,n) ,$$

where $\mathbf{R}$ is the common correlation matrix of the vector variables $\mathbf{Z}(t)$.

4. Hypothesis testing, statistical test based on norm

4.1 Basic properties of the norms of vector variables

Theorem 4.1.1

Let us assume about the vector variables $\mathbf{Z}(t) = [\mathrm{Z}_1(t),\ldots,\mathrm{Z}_\mathrm{N}(t)]^\mathrm{T}$ $(t = 1,2,\ldots\ldots,n)$, that the vector of expectations is $\mathrm{E}(\mathbf{Z}(t)) = \mathbf{0}$, the vector of standard deviations is $\mathrm{D}(\mathbf{Z}(t)) = \mathbf{1}$, and the correlation matrix is $\mathrm{E}(\mathbf{Z}(t)\mathbf{Z}(t)^\mathrm{T}) = \mathbf{R}$.

Then the following properties are true:

i. Let $\mathbf{R}^{\frac{1}{2}} = \left(\mathbf{R}^{\frac{1}{2}}\right)^{\mathrm{T}}$, $\mathbf{R}^{\frac{1}{2}}\mathbf{R}^{\frac{1}{2}} = \mathbf{R}$. Then the covariance matrix of $\mathbf{R}^{-\frac{1}{2}}\mathbf{Z}(t)$ is the identity matrix **I**.

ii. If matrix **P** satisfies that the covariance matrix of $\mathbf{PZ}(t)$ is **I**, then $\|\mathbf{PZ}(t)\| = \left(\mathbf{Z}(t)^{\mathrm{T}}\mathbf{R}^{-1}\mathbf{Z}(t)\right)^{\frac{1}{2}} = \|\mathbf{Z}(t)\|_{\mathbf{R}^{-1}}$, where $\|\mathbf{PZ}(t)\|$ is the Euclidean norm.

iii. If $\mathbf{Z}(t) \in N(\mathbf{0}, \mathbf{R})$, that means that the joint distribution of the components is normal, then $\|\mathbf{Z}(t)\|_{\mathbf{R}^{-1}} \in \chi_N$, i.e., this $\mathbf{R}^{-1}$-norm is chi distributed with degrees of freedom *N*.

Proof.

i. If $\mathrm{E}\left(\mathbf{Z}(t)\mathbf{Z}(t)^{\mathrm{T}}\right) = \mathbf{R}$, then $\mathrm{E}\left(\left(\mathbf{R}^{-\frac{1}{2}}\mathbf{Z}(t)\right)\left(\mathbf{R}^{-\frac{1}{2}}\mathbf{Z}(t)\right)^{\mathrm{T}}\right) =$

$$= \mathrm{E}\left(\mathbf{R}^{-\frac{1}{2}}\mathbf{Z}(t)\mathbf{Z}(t)^{\mathrm{T}}\mathbf{R}^{-\frac{1}{2}}\right) = \mathbf{R}^{-\frac{1}{2}}\mathrm{E}\left(\mathbf{Z}(t)\mathbf{Z}(t)^{\mathrm{T}}\right)\mathbf{R}^{-\frac{1}{2}} = \mathbf{R}^{-\frac{1}{2}}\mathbf{R}\mathbf{R}^{-\frac{1}{2}} = \mathbf{I}.$$

ii. If $\mathrm{E}\left((\mathbf{PZ}(t))(\mathbf{PZ}(t))^{\mathrm{T}}\right) = \mathbf{I}$, then $\mathbf{PRP}^{\mathrm{T}} = \mathbf{I}$, since $\mathbf{PRP}^{\mathrm{T}} = \mathrm{E}\left((\mathbf{PZ}(t))(\mathbf{PZ}(t))^{\mathrm{T}}\right)$. Therefore, $\mathbf{R} = \mathbf{P}^{-1}(\mathbf{P}^{\mathrm{T}})^{-1}$, and so $\mathbf{R}^{-1} = \mathbf{P}^{\mathrm{T}}\mathbf{P}$. Consequently, $\|\mathbf{PZ}(t)\| = \left(\mathbf{Z}(t)^{\mathrm{T}}\mathbf{P}^{\mathrm{T}}\mathbf{PZ}(t)\right)^{\frac{1}{2}} =$

$$= \left(\mathbf{Z}(t)^{\mathrm{T}}\mathbf{R}^{-1}\mathbf{Z}(t)\right)^{\frac{1}{2}} = \|\mathbf{Z}(t)\|_{\mathbf{R}^{-1}}.$$

iii. If $\mathbf{Z}(t) \in N(\mathbf{0}, \mathbf{R})$ then $\mathbf{R}^{-\frac{1}{2}}\mathbf{Z}(t) \in N(\mathbf{0}, \mathbf{I})$ by item (i) and therefore, $\left\|\mathbf{R}^{-\frac{1}{2}}\mathbf{Z}(t)\right\| \in \chi_N$ according to the definition of chi distribution. Furthermore, $\|\mathbf{Z}(t)\|_{\mathbf{R}^{-1}} = \left\|\mathbf{R}^{-\frac{1}{2}}\mathbf{Z}(t)\right\|$ as a consequence of item (ii).

4.2 Statistical test

Using the concept of multidimensional extreme, the hypothesis test for the identical distribution of vector variables can be implemented as follows.

Let us assume that the vector variables $\mathbf{X}(t)$ $(t = 1,2,\ldots\ldots,n)$ are totally independent. Then the null hypothesis for their identical distribution can be accepted if and only if

$$\|\mathbf{Z}(t_e)\|_{\mathbf{R}^{-1}} = \max_{1 \le t \le n} \|\mathbf{Z}(t)\|_{\mathbf{R}^{-1}} < cr,$$

where cr is a critical value on a given significance level. This critical value can be calculated on the basis of the chi distribution.

Remark 4.2.1

The question may arise as to whether the application of $\mathbf{R}^{-1}$-norm is optimal, as other $\mathbf{A}$-norm $\|\mathbf{Z}(t)\|_{\mathbf{A}} = (\mathbf{Z}(t)^{\mathrm{T}}\mathbf{A}\mathbf{Z}(t))^{\frac{1}{2}}$ could be used, where $\mathbf{A} = \mathbf{A}^{\mathrm{T}}$ is a positive definite square matrix. According to the following theorem, if a different $\mathbf{A}$-norm were used, the efficiency of the test would be expected to decrease.

Theorem 4.2.1 ("minimal" acceptance region)

Let us assume about the vector variable $\mathbf{Z} = [Z_1, \ldots, Z_N]^T$, that the vector of expectations is $\mathrm{E}(\mathbf{Z}) = \mathbf{0}$, the vector of standard deviations is $\mathrm{D}(\mathbf{Z}) = \mathbf{1}$, and the correlation matrix is $\mathrm{E}(\mathbf{Z}\mathbf{Z}^{\mathrm{T}}) = \mathbf{R}$. Let us assume further, that the positive definite matrix $\mathbf{A} = \mathbf{A}^{\mathrm{T}}$satisfies the following criterion for the expected value of the norm square: $\mathrm{E}(\mathbf{Z}^{\mathrm{T}}\mathbf{A}\mathbf{Z}) = \mathrm{E}(\mathbf{Z}^{\mathrm{T}}\mathbf{R}^{-1}\mathbf{Z}) = N$.
Then the inequality $|\mathbf{R}| \leq |\mathbf{A}^{-1}|$ is true for the determinants, consequently

$$\int_{\mathbf{z}^{\mathrm{T}}\mathbf{R}^{-1}\mathbf{z}<\alpha} 1 \ \mathrm{d}\mathbf{z} = |\mathbf{R}|^{\frac{1}{2}} \int_{\mathbf{y}^{\mathrm{T}}\mathbf{y}<\alpha} 1 \ \mathrm{d}\mathbf{y} \leq |\mathbf{A}^{-1}|^{\frac{1}{2}} \int_{\mathbf{y}^{\mathrm{T}}\mathbf{y}<\alpha} 1 \ \mathrm{d}\mathbf{y} = \int_{\mathbf{z}^{\mathrm{T}}\mathbf{A}\mathbf{z}<\alpha} 1 \ \mathrm{d}\mathbf{z}.$$

Proof.

First it needs to be seen that the determinants fulfil the inequality $|\mathbf{R}| \leq |\mathbf{A}^{-1}|$.
According to our assumption:

$$\mathrm{E}(\mathbf{Z}^{\mathrm{T}}\mathbf{A}\mathbf{Z}) = \mathrm{E}\left(\left(\mathbf{A}^{\frac{1}{2}}\mathbf{Z}\right)^{\mathrm{T}}\left(\mathbf{A}^{\frac{1}{2}}\mathbf{Z}\right)\right) = N.$$

Consequently, the sum of the diagonal elements of matrix $\mathbf{A}^{\frac{1}{2}}\mathbf{R}\mathbf{A}^{\frac{1}{2}}$ is also equals to N, since

$$\mathbf{A}^{\frac{1}{2}}\mathbf{R}\mathbf{A}^{\frac{1}{2}} = \mathrm{E}\left(\left(\mathbf{A}^{\frac{1}{2}}\mathbf{Z}\right)\left(\mathbf{A}^{\frac{1}{2}}\mathbf{Z}\right)^{\mathrm{T}}\right) = \mathrm{E}\left(\mathbf{A}^{\frac{1}{2}}\mathbf{Z}\mathbf{Z}^{\mathrm{T}}\mathbf{A}^{\frac{1}{2}}\right).$$

Therefore, the arithmetic mean of the eigenvalues of matrix $\mathbf{A}^{\frac{1}{2}}\mathbf{R}\mathbf{A}^{\frac{1}{2}}$ equals to 1, consequently their geometric mean and their product are less or equal to 1. Using that the product of the eigenvalues equals to the determinant of the matrix we obtain,

$$\left|\mathbf{A}^{\frac{1}{2}}\mathbf{R}\mathbf{A}^{\frac{1}{2}}\right| = |\mathbf{R}||\mathbf{A}| \leq 1, \text{ and so } |\mathbf{R}| \leq |\mathbf{A}^{-1}|.$$

Then applying the substitutions $\mathbf{y} = \mathbf{R}^{-\frac{1}{2}}\mathbf{z}$ and $\mathbf{y} = \mathbf{A}^{\frac{1}{2}}\mathbf{z}$, respectively, we have proved the following relation,

$$\int_{\mathbf{z}^{\mathrm{T}}\mathbf{R}^{-1}\mathbf{z}<\alpha} 1 \ \mathrm{d}\mathbf{z} = |\mathbf{R}|^{\frac{1}{2}} \int_{\mathbf{y}^{\mathrm{T}}\mathbf{y}<\alpha} 1 \ \mathrm{d}\mathbf{y} \leq |\mathbf{A}^{-1}|^{\frac{1}{2}} \int_{\mathbf{y}^{\mathrm{T}}\mathbf{y}<\alpha} 1 \ \mathrm{d}\mathbf{y} = \int_{\mathbf{z}^{\mathrm{T}}\mathbf{A}\mathbf{z}<\alpha} 1 \ \mathrm{d}\mathbf{z}.$$

Remarks 4.2.2

1. According to Theorem 4.2.1, applying a different $\mathbf{A}$-norm for which the probability of the first type error would be similar to that of the $\mathbf{R}^{-1}$-norm would increase the probability of the second type error, therefore, it would decrease the efficiency of the test. In addition, the test is expected to be more effective if the determinant is smaller, that means a stronger linear connection between the components of the vector variable $\mathbf{Z}$.
2. Consequently, in respect of the second type error, the following series of statistics are optimal for testing: $ST(t) = \|\mathbf{Z}(t)\|_{\mathbf{R}^{-1}} = (\mathbf{Z}(t)^{\mathrm{T}}\mathbf{R}^{-1}\mathbf{Z}(t))^{\frac{1}{2}}$ $(t = 1,2,\ldots\ldots,n)$.
3. In order to determine and select the extremes optimally, it is expedient also to examine the subsystems of the components.

5. Analysis of the subsystems of the components

5.1 The subsystems of the components and their properties

According to the former notations, let $\mathbf{Z}(t) = [Z_1(t),\ldots,Z_N(t)]^T$ $(t = 1,2,\ldots\ldots,n)$ be vector variables, assuming that the vector of expectations is $\mathrm{E}(\mathbf{Z}(t)) = \mathbf{0}$, the vector of standard deviations is $\mathrm{D}(\mathbf{Z}(t)) = \mathbf{1}$, and the correlation matrix is $\mathrm{E}(\mathbf{Z}(t)\mathbf{Z}(t)^{\mathrm{T}}) = \mathbf{R}$.
The subsystem of the components can be defined by the subsets of indexes $J = \{j_1,\ldots,j_L\} \subseteq \{1,\ldots,N\}$, and the appropriate subsystem vector variables are, $\mathbf{Z}_J(t) = \left[\mathrm{Z}_{j1}(t),\ldots,\mathrm{Z}_{jL}(t)\right]^{\mathrm{T}} \qquad (t = 1,2,\ldots\ldots,n)$.
The correlation matrix is $\mathrm{E}\left(\mathbf{Z}_J(t)\mathbf{Z}_J(t)^{\mathrm{T}}\right) = \mathbf{R}_J \qquad (t = 1,2,\ldots\ldots,n)$.

The series of the statistics characterizing the extremity of the subsystem vector variables defined by the index subset *J* are as follows:

$$ST(t,J) = \left\|\mathbf{Z}_J(t)\right\|_{\mathbf{R}_J^{-1}} = \left(\mathbf{Z}_J(t)^T\mathbf{R}_J^{-1}\mathbf{Z}_J(t)\right)^{\frac{1}{2}} \qquad (t = 1,2,\ldots\ldots,n)\,.$$

Theorem 5.1.1

If $J_1 = \left\{j_1,\ldots,j_{L_1}\right\} \subseteq J_2 = \left\{j_1,\ldots,j_{L_1+1},\ldots,j_{L_2}\right\} \subseteq \{1,\ldots,N\}$, then with probability 1,
$ST(t,J_1) = \left\|\mathbf{Z}_{J_1}(t)\right\|_{\mathbf{R}_{J_1}^{-1}} \leq \left\|\mathbf{Z}_{J_2}(t)\right\|_{\mathbf{R}_{J_2}^{-1}} = ST(t,J_2) \qquad (t = 1,2,\ldots\ldots,n)$

Proof.
According to our notations, $\mathbf{Z}_{J_1}(t) = \left[\mathrm{Z}_{j1}(t),\ldots,\mathrm{Z}_{jL_1}(t)\right]^T$,

$$\mathbf{Z}_{J_2}(t) = \left[\mathrm{Z}_{j1}(t),..,\mathrm{Z}_{jL_1}(t),..,\mathrm{Z}_{jL_2}(t)\right]^{\mathrm{T}}.$$

Let us see the linear Euclidean space generated by the components $\mathrm{Z}_{j1}(t),..,\mathrm{Z}_{jL_1}(t),..,\mathrm{Z}_{jL_2}(t)$ of the vector variable $\mathbf{Z}_{J_2}(t)$, where the scalar product is the covariance.

In this space, the components of the vector variable $\mathbf{R}_{J_1}^{-\frac{1}{2}}\mathbf{Z}_{J_1}(t)$ form an orthonormal system by item (i) of Theorem 4.1.1. Then according to the orthonormalization procedure, there exists such orthonormal basis in the space, whose first L_1 elements are exactly these components.
Formalized, there is a matrix $\mathbf{P} = \left[\mathbf{P}_1^{\mathrm{T}}, \mathbf{P}_2^{\mathrm{T}}\right]^{\mathrm{T}}$ that the covariance matrix of the vector variable $\mathbf{P}\mathbf{Z}_{J_2}(t) = \left[\left(\mathbf{P}_1\mathbf{Z}_{J_2}(t)\right)^{\mathrm{T}}, \left(\mathbf{P}_2\mathbf{Z}_{J_2}(t)\right)^{\mathrm{T}}\right]^{\mathrm{T}}$ is the identity matrix $\mathbf{I}$, and $\mathbf{P}_1\boldsymbol{Z}_{J_2}(t) = \mathbf{R}_{J_1}^{-\frac{1}{2}}\mathbf{Z}_{J_1}(t)$.

Consequently, according to item (ii) of Theorem 4.1.1.:
$\left\|\mathbf{Z}_{J_2}(t)\right\|_{\mathbf{R}_{J_2}^{-1}} = \left\|\mathbf{P}\mathbf{Z}_{J_2}(t)\right\|$ and $\left\|\mathbf{Z}_{J_1}(t)\right\|_{\mathbf{R}_{J_1}^{-1}} = \left\|\mathbf{R}_{J_1}^{-\frac{1}{2}}\mathbf{Z}_{J_1}(t)\right\|$, therefore

$$\left\|\mathbf{Z}_{J_2}(t)\right\|^2_{\boldsymbol{R}_{J_2}^{-1}} = \left\|\mathbf{P}\mathbf{Z}_{J_2}(t)\right\|^2 =$$

$$= \left[\left(\mathbf{R}_{J_1}^{-\frac{1}{2}}\mathbf{Z}_{J_1}(t)\right)^{\mathrm{T}}, \left(\mathbf{P}_2\mathbf{Z}_{J_2}(t)\right)^{\mathrm{T}}\right]\left[\left(\mathbf{R}_{J_1}^{-\frac{1}{2}}\mathbf{Z}_{J_1}(t)\right)^{\mathrm{T}}, \left(\mathbf{P}_2\mathbf{Z}_{J_2}(t)\right)^{\mathrm{T}}\right]^{\mathrm{T}} =$$

$$= \left(\mathbf{R}_{J_1}^{-\frac{1}{2}}\mathbf{Z}_{J_1}(t)\right)^{\mathrm{T}}\left(\mathbf{R}_{J_1}^{-\frac{1}{2}}\mathbf{Z}_{J_1}(t)\right) + \left(\mathbf{P}_2\mathbf{Z}_{J_2}(t)\right)^{\mathrm{T}}\left(\mathbf{P}_2\mathbf{Z}_{J_2}(t)\right) =$$

$$= \left\|\mathbf{Z}_{J_1}(t)\right\|^2_{\mathbf{R}_{J_1}^{-1}} + \left\|\mathbf{P}_2\mathbf{Z}_{J_2}(t)\right\|^2.$$

Thus, $\left\|\mathbf{Z}_{J_2}(t)\right\|^2_{\mathbf{R}_{J_2}^{-1}} \geq \left\|\mathbf{Z}_{J_1}(t)\right\|^2_{\mathbf{R}_{J_1}^{-1}}$.

5.2 Extreme subsystems

As a consequence of Theorem 5.1.1, if a subsystem of the components is "extreme", then it is presumably visible throughout the system.
A further consequence is that this theorem allows a meaningful, consistent definition of the series of the L-element ($L = 1,2,\ldots..,N$) extreme subsystems.
Let $JL(t) \subseteq \{1,\ldots,N\}$ ($\#JL(t) = L$), where # denotes cardinality be the index set of the L-element extreme subsystem at time t ($L = 1,2,\ldots..,N$; $t = 1,2,\ldots,n$), if

$$ST(t,JL(t)) = STL(t) = \max(ST(t,J)|\ J \subseteq \{1,\ldots,N\},\ \#J = L)\ .$$

According to the notations, the L-element extreme subsystem at time t is $\mathbf{Z}_{JL(t)}(t)$. Furthermore, as a consequence of Theorem 5.1.1, it is true for the series of statistics $STL(t)$ $(t = 1,2,\ldots\ldots,n)$ belonging to the L-element extreme subsystems that

$$\max_{1\le j\le N}\left|Z_j(t)\right| = ST1(t) \le ST2(t) \le \cdots \ldots \le STN(t) = \|\mathbf{Z}(t)\|_{\mathbf{R}^{-1}}$$
$$(t = 1,2,\ldots\ldots,n).$$

5.3 Methodological basis for the analysis procedure

1. Examination of the series of the statistics $STL(t)$ $(t = 1,\ldots,n)$ showing which series $(L = 1,..,N)$ majorize each other, followed by the looking for the extremes and testing them on the basis of the critical values.
2. Calculation of the critical values on the given significance level assuming the chi distribution.
3. Examination of the subsystems $JL(t)$ belonging to the statistics
   $STL(t) = ST(t, JL(t))$ $(t = 1,\ldots,n; \quad L = 1,..,N)$.
4. Comparison of the statistics $STL(t)$ $(t = 1,\ldots,n; \quad L = 1,..,N)$ for different L can be done on the basis of the following probabilities: $p(STL(t)) = 1 - H_L(STL(t))$ $(t = 1,\ldots,n; \quad L = 1,..,N)$, where $H_L(x)$ is the chi distribution function with degrees of freedom L. The less probability $p(STL(t))$ is the more extreme value.
5. Examination of the climate indexes SPI, STI, and SPTI is also recommended.

6. Meteorological applications

6.1 Data

For our study, we used daily data from the last 151 years. For temperature, this means 11 stations from January 1, 1870, 33 from January 1, 1901, 55 from January 1, 1951, and 114 from January 1, 1975 to December 31, 2020. For precipitation, we used data from 11 precipitation stations from January 1, 1870, 131 from January 1, 1901, and 461 from January 1, 1951 to December 31, 2020 (*Figs. 1* and *2*).

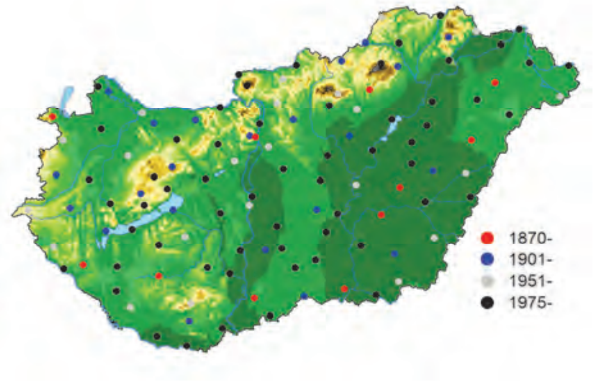

Fig. 1. Location of the stations in case of temperature.

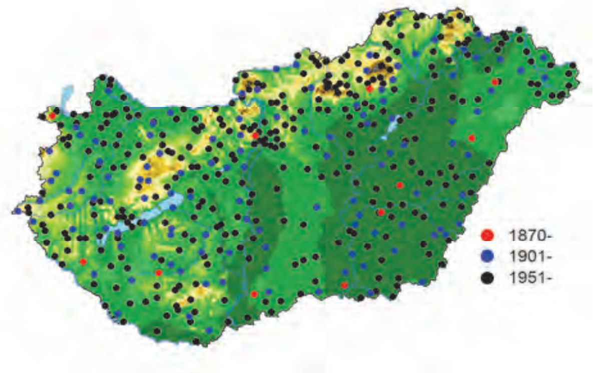

Fig. 2. Location of the stations in the case of precipitation.

As a first step, representative time series had to be produced from the raw measurements. Climate studies, in particular those related to climate change, require long, high-quality, controlled data sets which are both spatially and temporally representative. Changing the context in which the measurements were taken, for example relocating the station, or a change in the frequency of measurements or in the instruments used may result in an unduly fractured time series (*Izsák* and *Szentimrey*, 2020). Data errors and inhomogeneities are eliminated and data gaps are filled in using the MASH (Multiple Analysis of Series for Homogenization; *Szentimrey*, 2017) homogenization procedure. The homogenized station data series were interpolated to a regular grid covering the whole area of Hungary using the MISH (Meteorological Interpolation based on Surface Homogenized Data Basis; *Szentimrey* and *Bihari*, 2014) method, thus obtaining a high quality, representative data set. The method was used for both temperature and precipitation amount series, thus we obtained a grid point time series system with daily data at a resolution of 0.1 × 0.1 degrees. The grid point system is shown in *Fig. 3*. In order to use the longest measurement data from as many stations as possible for our dataset, we harmonized four MASH systems during homogenization and used the grid point data set interpolated using the most stations at each time point during interpolation (*Izsák et al.*, 2022).

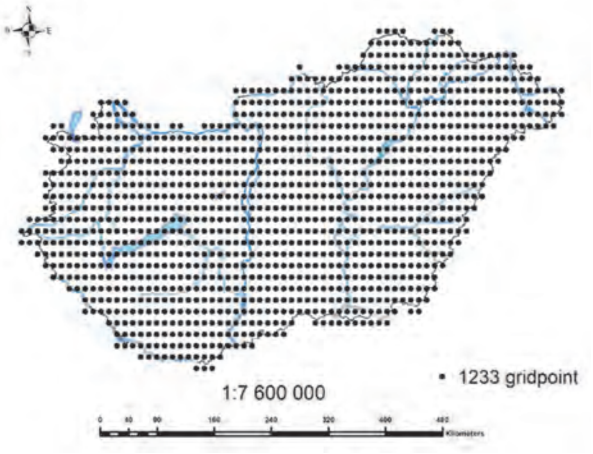

Fig. 3. Spatial location of the gridpoints.

In the next step, the *SPI* (Section 3.1) and *STI* (Section 3.2) variable series are calculated from the grid point data series (*WMO,* 2012; *Szentimrey et al.,* 2014). For annual studies, we will have *SPI12*, i.e., calculated for 12-month precipitation accumulation periods, similarly *STI12* for temperature as our transformed data series. For seasonal studies, we calculate *SPI3* and *STI3* for all 1233 grid points, correspondingly to a resolution of 0.1 degrees. If we perform our analyses in space, we compute the grid point *SPTI* series (Definition 3.3.1) from the corresponding *SPI* and *STI* series. This is shown for two-dimensional studies in Section 6.3. and for eight-dimensional studies in Section 6.4.

If we are studying a regional average, we compute the spatial average of the *STI* and *SPI* series, and then standardize these, since the average of standard normal series will no longer necessarily have a standard normal distribution. Then these standardized spatial average *SPI* and *STI* series will be the components of the multivariate spatial average vector variable series. Consequently, the spatial average norm and *SPTI* series are computed also from the standardized spatial averages of *SPI* and *STI* series. Specifically, for the eight-dimensional studies, the standardized spatial average *SPI3* and *STI3* for the seasons are the eight components of the vector variable. From this we compute the eight-dimensional *ST8* norms (Definition 2.5.1) and the extreme subsystems *ST1*, *ST2*,..., *ST8* (Section 5.2). The corresponding values are presented in Section 6.4. Calibration period for both the two- and eight-dimensional statistics presented in this paper is the period 1871–1900.

6.2 Statistical tests

As indicated in Sections 4.2 and 5.3, to accept the null hypothesis of identical distribution of vector variables, the critical value for a given significance level must be specified. In the present case, certain critical values have been defined at a significance level of 0.1. Three different statistical tests are used to see whether climate change can be detected by analyzing different meteorological elements together. In the following subsections, the procedure for determining the tests and their corresponding critical values is described.

6.2.1 Test 1

In this test, we seek to answer the question: are extreme events more frequent than would be expected for the identical distribution?

The first critical value is defined as follows:

- For any *STN(t)* ($t = 1, 2, ..., n$) statistic, there is a probability of 0.1 that the critical value *Cr1* is reached, i.e., it is expected to occur in 10% of the statistics.

Cr1 values are given in *Table 1* determined assuming joint normality of the transformed components, therefore, the chi distribution was applied for the statistics *STN(t)* according to item (iii) of Theorem 4.1.1.

The test procedure is as follows:

- Calculate the *STN(t)* norms and then to determine the frequency of norms exceeding the *Cr1* value for the total period. This frequency is denoted by v.
- If the null hypothesis is true then $v \in B(n,p)$, where $B(n,p)$ denotes the Binomial distribution with parameters n and p, specifically n=150 and p=0.1.
- Consequently, according to the central limit theorem, the standardized value *TS1* of the frequency ν converges to the standard normal distribution.
- This gives the critical value *Cr3*=1.65 for the standardized value *TS1* at the significance level 0.1. If *TS1*≥ Cr3, the null hypothesis for the identical distribution is not accepted, if *TS1*<Cr3, it is accepted.

6.2.2 Test 2

In the second test, we seek to answer the question whether there are extreme cases in the data set that would have a low probability of occurring if the distribution were identical.

This test is detailed in Section 4.2, and the critical value *Cr2* is defined as follows:

- The maximum of the statistics *STN(t)* ($t = 1, 2, ..., n$) with probability at most 0.1 can reach the critical value *Cr2*.

Table 1 shows these *Cr2* values as a function of the different degrees of freedom. For the present study, the *Cr2* critical values refer to the n=150 years data set. In determining the critical values, the chi distribution was assumed for the statistics *STN(t)* according to item (iii) of Theorem 4.1.1.

Table 1. Critical values

Degrees of freedom	**2**	**3**	**4**	**6**	**8**	**12**	**24**
Cr1	2.15	2.50	2.79	3.26	3.66	4.31	5.76
Cr2	3.81	4.12	4.39	4.83	5.20	5.82	7.24

6.2.3 Test 3

Trend analysis is used to answer the question: is there a one-way change in extremality over time that would occur with low probability given the same distribution?

We fit an exponential trend to *STN(t)* statistics. We test the significance of the resulting trend coefficient. If the one-way change is significant, we reject the null hypothesis at the given significance level. The significance level in the present case is 0.1.

6.3 Two-dimensional application: the SPTI index

In the analysis, we consider the *SPTI* (Definition 3.3.1) series defined above, both for the spatial average and for grid points. In the two-dimensional case, *Cr1*=2.15 and *Cr2*=3.81 for n=150 (*Table 1*). Based on Section 6.2, statistical tests were carried out to see if there is a change in climate when the two elements are considered together.

Fig. 4 shows the spatial average *SPI*, *STI* and *SPTI* values based on annual precipitation sum and mean temperature. It can be clearly seen that there are values above both *Cr1* and *Cr2,* suggesting that there is climate change when looking at spatial average annual mean temperature and precipitation sum series together. The change in the *SPTI* index over 150 years was determined using exponential trend estimation. On spatial average, this index increased by 100% over the whole period. This change is significant at the 0.1 significance level. This is indicated by the green line in *Fig. 4*. Based on Section 6.2.1, the value of *TS1* was determined (*Table 3*). The null hypothesis of an identical distribution for the annual values, a spatial average, cannot be accepted on the basis of this test either, since a *TS1* value well above the critical value was obtained.

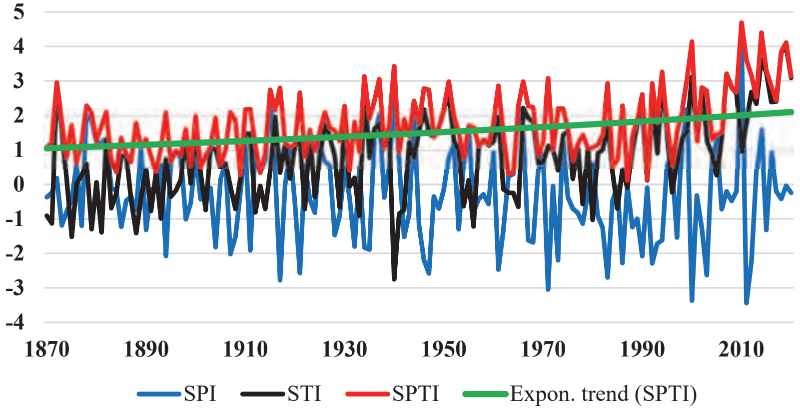

Fig. 4. Spatial average of SPI, STI and SPTI values, based on annual precipitation sum and mean temperature.

If the *SPTI* values are calculated as grid points instead of spatial averages, we can get an idea of which areas of Hungary are experiencing climate change at the 0.1 significance level, when the precipitation and temperature series are taken into account. In *Fig. 5* we show the areas where the maximum of the SPTI values exceeds *Cr2*, these are the red colored areas, while in the green colored areas, these statistics exceed only *Cr1*.

On a spatial average, 2010 was the extreme year with the highest precipitation but average temperature (*Table 2*) If we look at individual areas, *Fig. 6* shows that the year 2014 is still the one with the largest area. This year is markedly extreme in the sense that it is recorded in the yearbooks as a hot and wet year. The extreme drought and heat of the year 2000 makes it appear in even larger areas. Generally speaking, recent years appear as extreme. The largest areas are dominated by warm years with precipitation, but dry hot years also appear on the list. In the case of annual studies, the pairs of dry and cool years are not listed as extreme, but will only appear in seasonal studies.

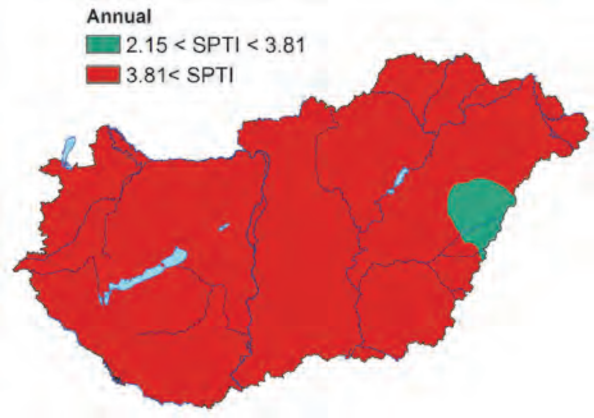

Fig. 5. Maximum of the SPTI values, based on annual precipitation sum and mean temperature, 1870–2020.

Table 2. Extreme years and seasons by SPTI, spatial average, 1871–2020

Annual		**Winter**		**Spring**		**Summer**		**Autumn**	
2010	4.69	**2006/07**	2.7	**1934**	3.8	**1984**	4.13	**1986**	4.08
2014	4.4	**1909/10**	2.62	**1875**	3.25	**2019**	4.07	**1920**	3.95
2000	4.14	**1935/36**	2.56	**2003**	3.02	**2003**	3.81	**1908**	3.69
2019	4.11	**1989/90**	2.49	**1946**	2.9	**1976**	3.57	**2011**	3.62
2018	3.85	**1950/51**	2.47	**1920**	2.85	**1978**	3.5	**2006**	3.31
2011	3.61	**1976/77**	2.44	**2018**	2.79	**2018**	3.49	**1978**	3.01
1940	3.43	**1879/80**	2.41	**1872**	2.78	**1962**	3.46	**1947**	2.93
2015	3.31	**1962/63**	2.4	**1937**	2.7	**2012**	3.46	**1959**	2.84
1994	3.26	**1881/82**	2.35	**2007**	2.66	**1919**	3.45	**1953**	2.76
2007	3.21	**1997/98**	2.25	**2010**	2.65	**1923**	3.43	**1912**	2.75

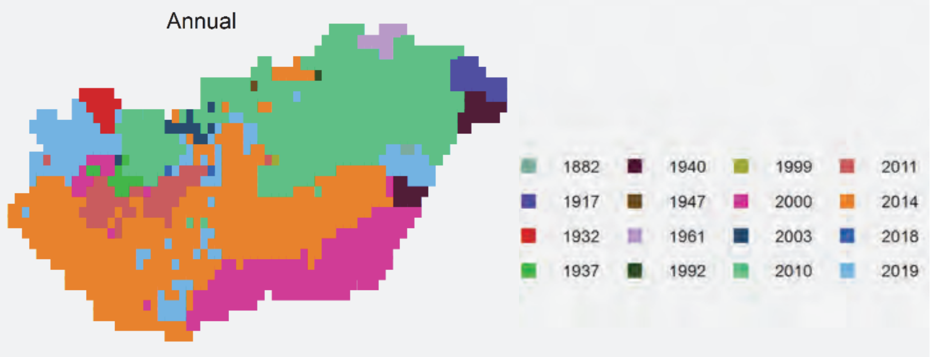

Fig. 6. Year of maximum SPTI values, based on annual precipitation sum and mean temperature, 1870–2020.

Similar to annual studies, seasons and months can be considered together in terms of precipitation sum and mean temperature.

If only the seasonal precipitation sums and mean temperatures are considered, the winter norm values (SPTI) are the lowest and exceed only the mildest *Cr1* critical value (*Fig. 7*). If we want to decide on the basis of the first test (Section 6.2.1), we can see the *TS1* values in *Table 3*. Only the winter value remains below the critical value. The other two tests (Sections 6.2.2 and 6.2.3) were also applied to the seasonal *SPTI* values. None of the spring norm values reaches *Cr2*, but here relatively many values exceed *Cr1*. The summer norm values are the highest and there are values exceeding *Cr2*. The autumn values also include some norms above *Cr2*, but on average they are lower than in the summer study. When an exponential trend is fitted to the *SPTI* values, significant changes are observed only in spring and summer. When the temperature and precipitation time series are considered together, significant increases are observed in both cases. Summer norm values increased by 90% and spring values by 55%.

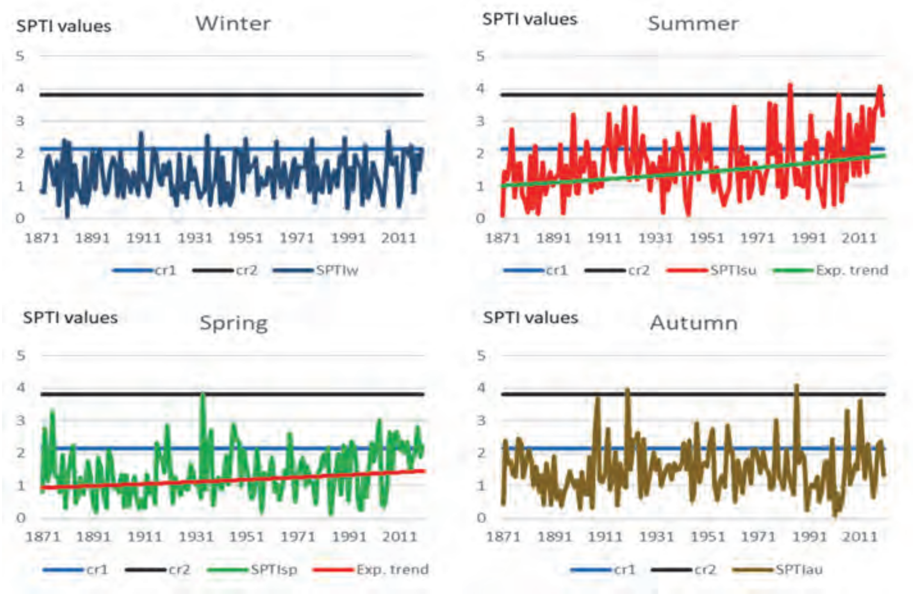

Fig 7. SPTI values by season, standardised spatial average.

Table 3. *TS1* values for Test1, the critical value is Cr3=1.65

1871-2020	Annual	Summer	Autumn	Winter	Spring
TS1	**9.25**	**8.16**	**2.72**	0.27	**2.99**

Of course, the seasonal analyses also examined the areas where the maximum *SPTI* values exceeded each critical value. The areas exceeding *Cr1* and *Cr2* are shown in *Fig. 8*. In all cases, the milder *Cr1* critical value is exceeded everywhere by the maximum of the normal values, these are the areas marked in green. Where the *SPTI* maxima exceed the more severe *Cr2* critical value, the area is red colored.

It can be clearly seen in *Fig. 8A* that the winter values do not reach *Cr2* anywhere, while for the autumn (*Fig. 8D*) and summer (*Fig. 8B*) maxima we get the largest areas with maximum *SPTI* values above the more stringent critical value.

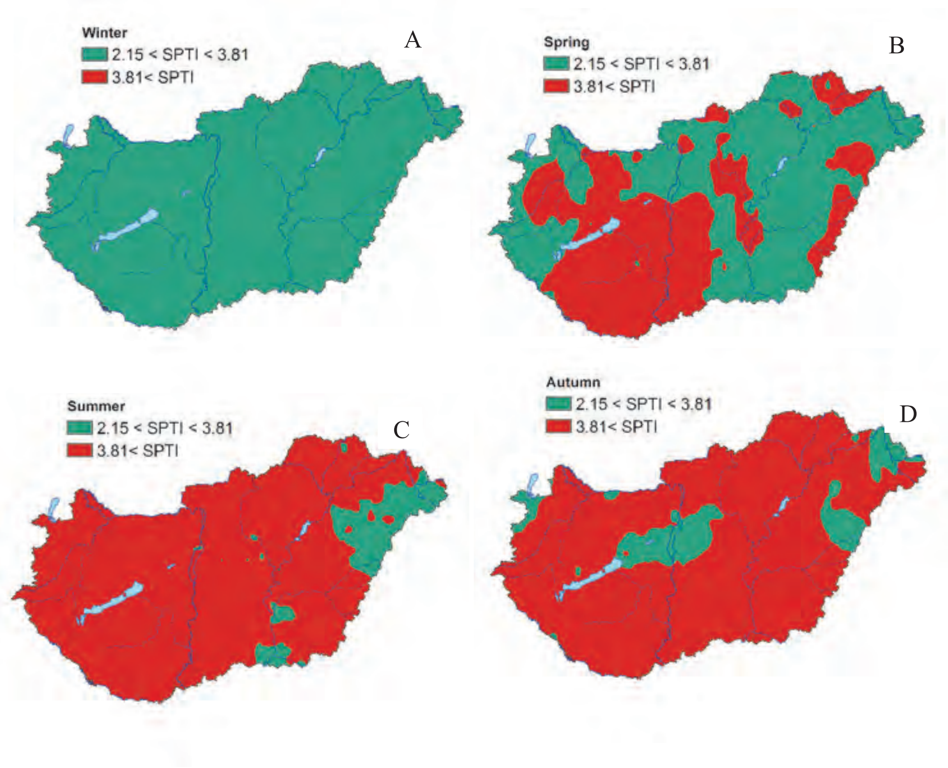

Fig. 8. Maximum SPTI values by season: winter (A), spring (B), summer (C), and autumn (D), based on seasonal precipitation sum and mean temperature, 1871–2020.

Let us look at the spring extremes for grid point data (*Fig. 9*). The hot, dry spring of 1934 is the most unusual spatial average, and the largest area for this year is shown on the map. Dry, hot springs occur over an even larger area in 2003 and 2012. A wet, warm spring is 2010, while the dry, cool feature that was missing in the annual surveys appears here: the springs of 1956 and 1875, for example. There is also an example of a wet, cool spring: 1919 was just such a spring, but it is only shown in one small area on the map (*Fig. 9*).

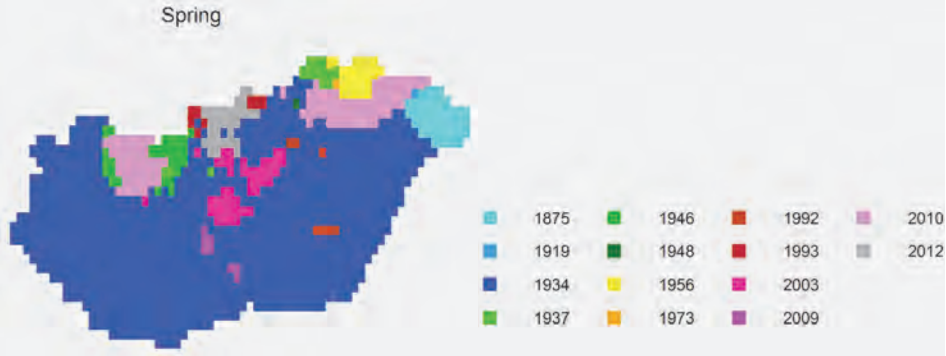

Fig. 9. Spring: year of maximum SPTI values.

The palette of summers is the most colorful (Fig. 10). On spatial average, the dry, cold summer of 1984 is the extreme. Although a large area of *Fig. 10* shows the summer of that year, it is the hot, dry summer of 2003 that is the most extreme over the largest area, precisely in areas where wet, less hot summers are otherwise common, namely the southern and western parts of the Transdanubian region. In general, dry, cool summers dominate the extreme lists, with a large number of dry, hot summers still on the map. Wet, cold summers include 1913 and wet, hot summers include, for example, 1999.

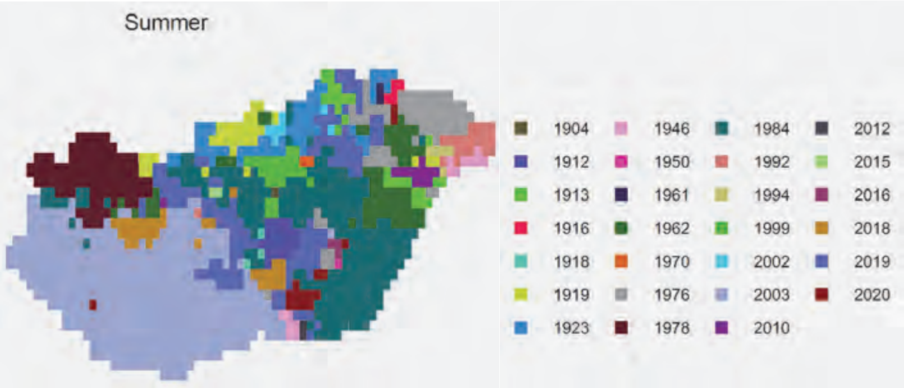

Fig. 10. Summer: year of maximum SPTI values.

The autumn extremes are also shown in *Table 2*. *Fig. 11* shows that the extreme dry and slightly warmer than average autumn of 1986 is the one with the largest area. It can also be said of the years shown in *Fig. 11*, that if we split the country in two parts imaginatively, the western half of the country has the most unusual cold, dry autumns, while the eastern half of the country has the most unusual dry, warm autumns.

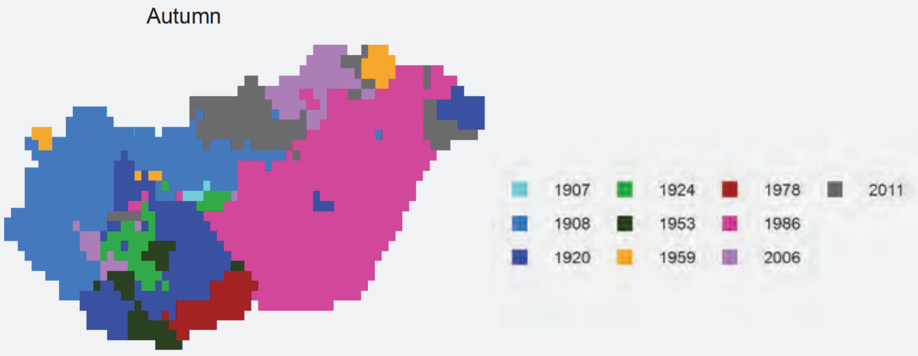

Fig. 11. Autumn: year of maximum SPTI values.

Finally, let us consider the combined extremes of winter (*Fig. 12*). Whether averaged by area or grid point, the *SPTI* indices show that the warmest winter with average precipitation in 2006/2007 is the most unusual of the 150-year-long temperature and precipitation series. Similarly to the summer values, all possible combinations are shown in *Fig. 12*. Warm, wet extremes include the winters of 1909/1910 and 1935/1936, while wet cool extremes include the winter of 1890/1891, but there are also examples of dry, cold winters, such as the winter of 1879/1880.

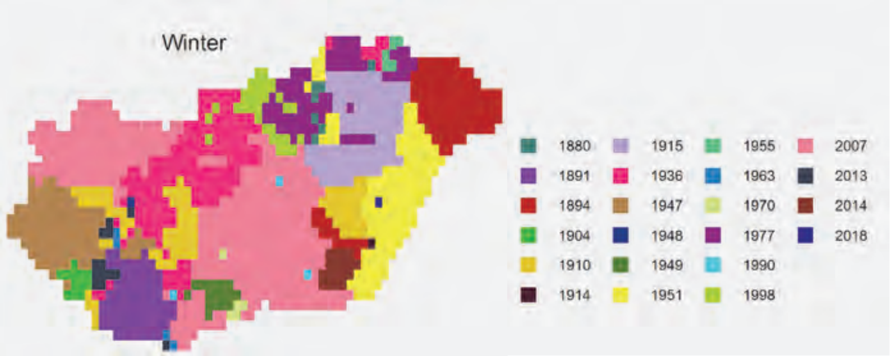

Fig. 12. Winter: year of maximum SPTI values.

6.4 Eight-dimensional application

As indicated in Section 6.1, *SPI3* and *STI3* values were derived from seasonal precipitation sum and mean temperature values for all four seasons. The standardized spatial averages become the components of the eight-dimensional vector variable. To determine the eight-dimensional extreme, the *ST8* statistics were calculated (Sections 2.5, 5.3), and these statistics were applied to the full dataset to decide on the presence of climate change in eight dimensions. Performing the first test (Section 6.2.1), the *TS1* was found to be 6.25, while the critical value is only 1.65, so the null hypothesis of an identical distribution in the eight-dimension cannot be accepted. *Fig. 13* shows that *Cr1*=3.66 is exceeded in a relatively large number of years, but the more stringent *Cr2*=5.20 is only reached in 2018 and 2019. Therefore, we can say that there is climate change with respect to the spatial average, when the mean temperature and precipitation series for the four seasons are considered together. Using an exponential trend estimation for the eight-dimensional norm series, a significant change can be seen, with these values increasing by 37%, shown in green in *Fig. 13*. 2018 was the second warmest and drier than average year, while 2019 was the warmest and slightly wetter than average year. What is striking from *Fig. 13* is that the last decade can be considered an extreme decade. If we plot the probability (Section 5.3) associated with the *ST8* eight-dimensional norm values (*Fig. 14*), this extreme period is more distinct, showing how low probability events have occurred in the past period. In terms of the eight-dimensional norms, 1947 has the third highest norm: it was essentially a dry, hot year. Only winter was wetter and cooler than average, the other three seasons were dry and warm in 1947. The most unusual of the components for 1947 is the autumn precipitation, which is listed as the 5th driest autumn in the 150-year-long time series. The year 1920 and 2020 are not considered extreme on average, but when the eight variables are analyzed together, they can be considered extreme years. In order, they are the fourth and fifth highest *ST8* values. In the year 1920, two seasons were cooler than average and two warmer, while in terms of precipitation, two seasons had above average precipitation and two were extremely dry. In 2020, we also had two very dry seasons and two seasons with above average precipitation, but temperatures were above average in all four seasons.

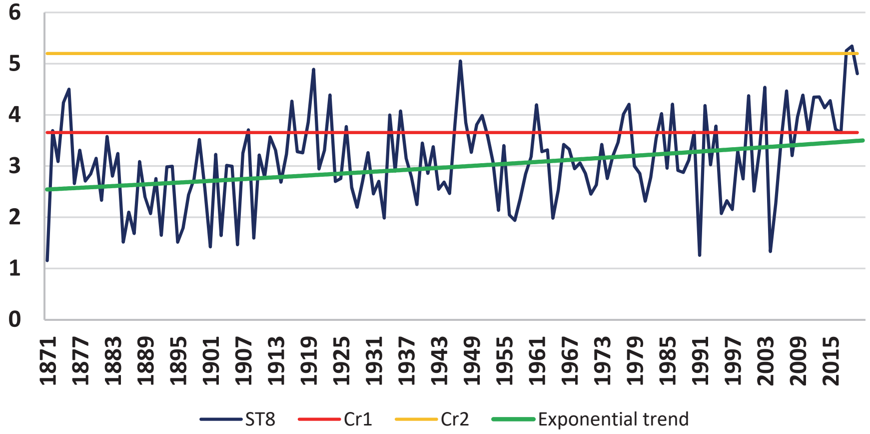

Fig. 13. ST8 values, spatial average.

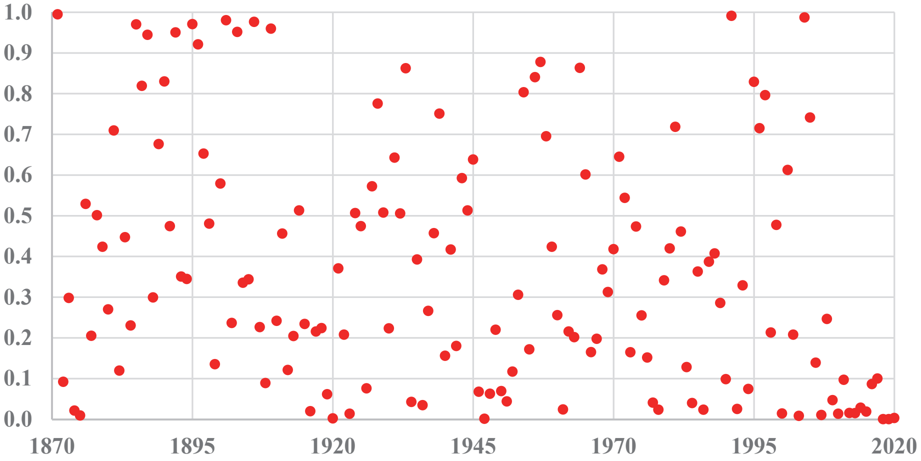

Fig. 14. The probability of ST8 values.

It is also interesting to look at the norm values for the extreme sub-systems (Section 5.2) in *Fig. 15*. For 2019, the two-dimensional extreme sub-system already exceeds the critical value *Cr1* for the eight-dimensional norm values. If we want to know which subsystem is the most unusual, we consider the probabilities in *Fig. 16B*. For the total period and all eight elements, the lowest probability is for the temperature of summer 2003, while the most extreme two-dimensional subsystem, with the addition of the spring drought of the same year, is the most extreme two-dimensional subsystem, with all other extreme subsystems belongs to 2019.

The lowest probability event belongs to the year 2019, of which this value also belongs to the four-element extreme subsystem: warm, dry summer, warm autumn, and wet spring. (*Fig. 16A*)

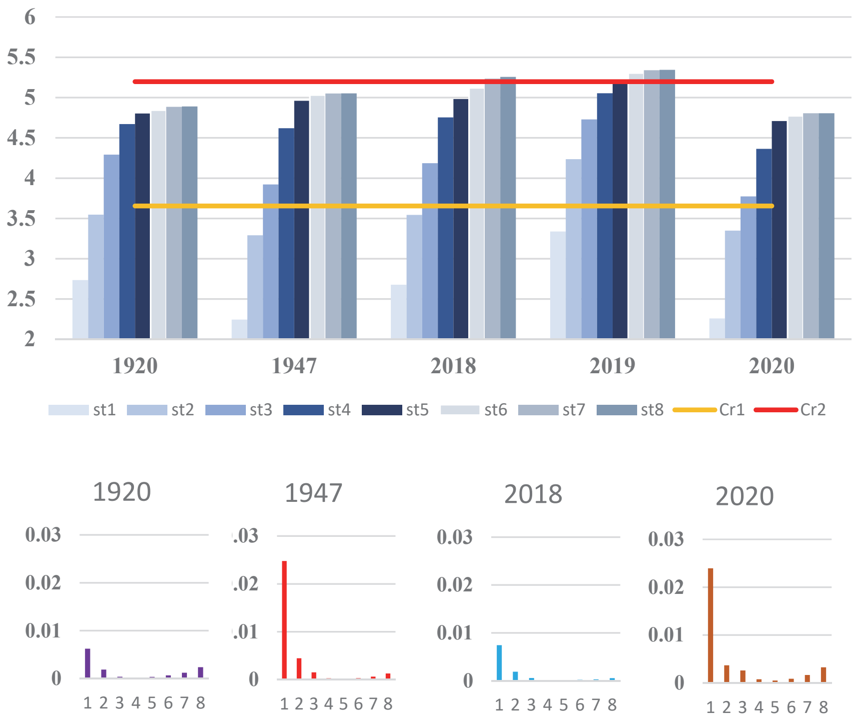

Fig. 15. ST1-8 values for extreme subsystems (top) and their probabilities per year (bottom).

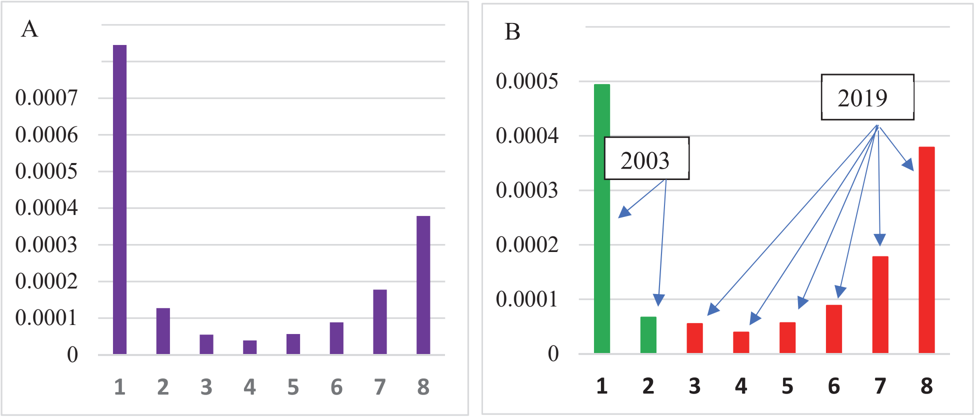

Fig. 16. A: Probability of extreme subsystems in 2019, B: Probability of extreme subsystems of the complete dataset.

If we want to know which seasons and which elements are responsible for the extremes of a given year, we need to analyze the extreme subsystems (Section 5.2), as we did above for the five extreme years (*Figs. 15, 16A*). For most of these, both elements deviated significantly from the average in all four seasons, resulting in high *ST8* norm values. On the other hand, there are years with *ST8* values above the critical value of *Cr1*, but the extremes are caused by only one or two elements. A good example of this is the year 1934 (*Fig 17*), when the probability of the one-dimensional subsystem was the lowest. This is the extreme high mean temperature in spring. Also, *Cr1* is above the norm for the year 1936, but here the two-dimensional extreme subsystem has the lowest probability, and this is the two-dimensional extreme subsystem of a wet winter and a warm spring (*Fig 17*).

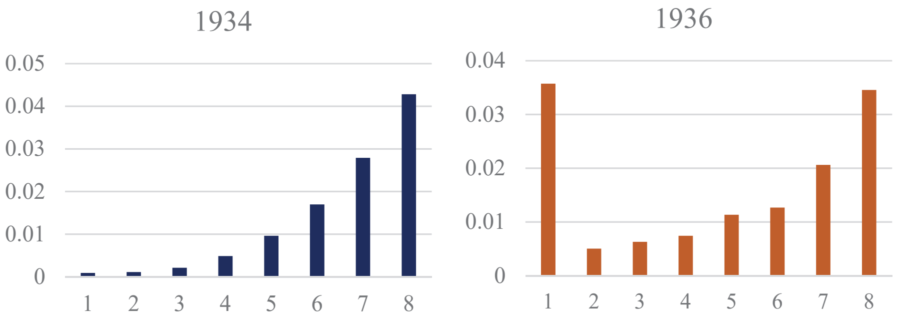

Fig. 17. Probability of ST1-8 norms for the years 1934 and 1936.

7. Summary

The primary objective of this paper was to present a vector norm methodology based on the probability distribution of multidimensional climate time series, which can be used to complement our knowledge of the extremes of climate elements. We have shown why this method was developed in order to study climate elements together and how it works in practice to determine multidimensional extremes.

The results of the statistical tests described in Section 6.2 are summarized in *Table 4*. For the first test (T1 in Section 6.2.1), the change in the distribution of the probability vector variables is not proven only for the winter temperature and precipitation values. For the second test (T2 in Section 6.2.2), the spring values do not exceed the *Cr2* values in addition to the winter values. In the third test (T3 in Section 6.2.3), no unidirectional change is observed for winter and autumn values. In summary, when looking at the two-dimensional annual and summer mean temperature and precipitation values together, all three tests result in rejecting the null hypothesis that there is climate change. The same is true for the four seasonal mean temperature and precipitation values, so that climate change can be detected in eight-dimensions with all three tests. In the case of the spring tests, the T1 and T3 tests were used to detect change, while for the autumn values the T1 and T2 tests were used. Only the winter tests can not demonstrate the change in the probability distribution of the vector variables over time.

Table 4. Summary table of which test and statistics have changes in probability distribution, 1871–2020

	Annual ST2	**Winter ST2**	**Spring ST2**	**Summer ST2**	**Autumn ST2**	**Annual ST8**
Test1	✓	X	✓	✓	✓	✓
Test2	✓	X	X	✓	✓	✓
Test3	✓	X	✓	✓	X	✓

In general, we can say that in Hungary cooler years tend to have more precipitation, while drier years tend to be warmer. This makes it unusual to have a very hot, wet year and a dry, cool year. It is also clear that a very dry, very hot year is also unusual, while a very cold, very wet year can be considered extreme. Looking at the temperature and precipitation time series together, we could see examples of each of these cases. Multidimensional extremes included years that could be considered extreme in one dimension, e.g., 2019, 2010, and 1940, but also included years that were not particularly unusual in one dimension, e.g., 1920, 1947, 2020.

Considering the spatial averages, years with hot, rainy weather are the least likely, followed by a series of dry, very hot years and only one case of a cool, rainy year. The top ten did not include a pair of dry, cool years. In the case of winters, the top ten is dominated by warm, wet winters, with dry, warm and cool, wet winters also found in *Table 2*. Most of the spring extremes are associated with dry, warm springs. There is one case of dry, cool spring and two cases of wet, warm spring in our list. For summers, the extremes are the dry, cool and dry, warm seasons. For autumn, these two combinations are also on the list. The exception is the 10th most extreme autumn, which has a very cold period with a lot of rainfall as an extreme. It is now accepted (*Harangi*, 2017), that the eruption of the Katmai-Novarupta volcano in Alaska (June 6, 1912) is responsible for this extreme autumn.

Of course, other elements and dimensions can be investigated further. Two-dimensional studies can be complemented by six-dimensional studies. For example, summers have the largest statistics, in which case it is worth looking at the mean temperature and precipitation totals for the three summer months together. But it is also possible to look at the precipitation sum and temperature of a single month together, or to determine the SPTI index for the summer and winter semesters. After the mathematical description, we have presented only some meteorological applications, the aim of which was to illustrate, through examples, how the theoretical method works in practice.

References

Harangi, Sz., 2017: Vulkánkitörések klímaváltoztató hatása: a kicsi is számít! *Magyar Tudomány 188*, 664–674. (In Hungarian)

Izsák, B. and *Szentimrey, T.,* 2020: To what extent does the detection of climate change in Hungary depend on the choice of statistical methods? *Int. J. Geomath. 11*, 17 https://doi.org/10.1007/s13137-020-00159-7

Izsák, B., Szentimrey, T., Lakatos, M., Pongrácz, R., and *Szentes, O.*: Creation of a representative climatological database for Hungary from 1870 to 2020. *Időjárás 126*, 1–26. https://doi.org.10.28974/idojaras.2022.1.1

Szentimrey, T., 1999: Többdimenziós éghajlati idősorok "extrémumainak" vizsgálata. Időjárási és éghajlati szélsőségek. Meteorológiai Tudományos Napok 1999. OMSZ, Budapest. 77–88. (in Hungarian)

Szentimrey, T., Lakatos, M., and *Bihari, Z.*, 2014: Joint examination of climate variables, Standardized Precipitation and Temperature Index (SPTI)). European Conference on Applied Climatology (ECAC), Prague, Czech Republic, 5-10 October, 2014.

Szentimrey, T. and *Bihari, Z.*, 2014: Manual of interpolation software MISHv1.03. OMSZ, Budapest.

Szentimrey, T., 2017: Manual of homogenization software MASHv3.03. OMSZ, Budapest.

WMO, 2012: Standardized Precipitation Index User Guide. WMO-No. 1090. https://library.wmo.int/index.php?lvl=notice_display&id=13682#.X4lJJ-28qUk

DOI:10.28974/idojaras.2022.2.2

IDŐJÁRÁS

Quarterly Journal of the Hungarian Meteorological Service
Vol. 126, No. 2, April – June, 2022, pp. 185–201

Assessment of the change of trend in precipitation over Afghanistan in 1979–2019

Qurban Aliyar Assistant [1] and **Morteza Esmailnejad** [2,*]

[1] *Department of Forestry and Natural Resources*
Faculty of Agriculture, Bamyan University
Afghanistan

[2] *Department of Geography*
University of Birjand
Birjand, Iran

**Corresponding author E-mail: esmailnejad.m@birjand.ac.ir*

(Manuscript received in final form March 9, 2021)

Abstract— The civil war, harsh climate, tough topography, and lack of accurate meteorological stations have limited the number of consecutive synoptic data across Afghanistan. The global data (gridded precipitation datasets) pave the way to assess the precipitation indicators of climate, where stations are sparsely located. This study assessed the mean annual precipitation trend in 33 stations over Afghanistan. Non-parametric linear regression technique was employed to find upward and downward trends and magnitudes. The daily of precipitation was obtained from the database of the CPC-NOAA (Climate Prediction Center - National Oceanic Atmospheric Administration) for the period of 1979–2019. The CPC spatial resolution of daily precipitation is 0.5×0.5 degree. Analysis of mean annual precipitation showed a significant decreasing trend at six provinces in the north, while an increasing trend of 9.2 mm per decade has been observed at three provinces. In the south, a notable reduction of the precipitation trend has been experienced in Helmand, Kandahar, and Nimruz provinces, but Ghazni and Uruzgan show a positive trend. Data revealed that mean annual precipitation has remarkably decreased in the western part of Afghanistan. According to the study period, the mean annual rainfall in the central regions indicates a raise of 37.5 mm per decade in Kabul, while in Vardak, the precipitation increases up to 9.21 mm per year. Eastern regions include 8 provinces, and the eastern highland covers the smallest area that is mainly covered by rangeland and the largest existing forests. These regions are directly influenced by the moist air masses of Indian monsoon getting trapped at the high mountain slopes, and it can lead to an increase of rain. Data reveals an upward trend of precipitation in the eastern part of Afghanistan.

Key-words: climate change, Afghanistan, rainfall variation

1. Introduction

Climate change is a change in climatic parameters (such as temperature, precipitation, and their characteristics) and associated patterns (*Pachauri et al*., 2014). In this regard, changes in temperature and precipitation due to their association with phenomena such as drought, floods, and their hydrological and biological consequences are receiving more attention (*Sheila*, 2013). Despite this very alarming situation, almost no scientific literature on climate change and its impacts in the past, nor projected for the future, exists (World Bank, 2014). Therefore, climate change as effective process on social, economic, and environmental phenomena and processes has been considered by scientific circles. (*Groisman et al*., 1999) Afghanistan is frequently ranked among the countries most vulnerable to climate change *(Kreft, et al*., 2015). Afghanistan, as a society often based on the rural economy on natural resources. The livelihood of most Afghans depends on agriculture, and agriculture depends on rainfall. Changes in rainfall could lead to vulnerability for farmers in Afghanistan, which is happening. These resources are very vulnerable to climate change. More than 80% of the country's water resources (a total of 75 billion cubic meters of water, 55 billion cubic meters of which includes surface currents and 20 billion cubic meters of groundwater) come from the Hindu Kush Mountains and its rainfall (World Bank, 2014). Change in climate extremes was assessed that indicate reduction frosts and freeze and raising in hot days in most part of the world (*Karl et al*., 1999). Climate variability is the one of the threats to water resources in tropical regions at large scale. Changes in precipitation have direct effects on water resources, agriculture, forestry, ecosystem, natural resources, plant cover, and drinking water (*Cannarozzo et al*., 2006). Precipitation generally increases in the extra-tropical areas, conversely, rainfall declines in the subtropical region (*Houghton*, 1996). Change in precipitation, evaporation, and snow cover extent have occurred significantly, during the last 50 years over the conterminous United States (*Kunkel et al*., 1999; *Frei et al*., 1999). Precipitation shows a 10% increase since 1910 throughout the contiguous United States (*Karl* and *Knight*, 1998). Precipitation trend is seen as a long-term increase mostly in North America, mid- to high-latitude Eurasia, Argentina, and Australia during the period of 1900–1988 (*Dai et al*., 1997). Frequency of precipitation has been remarkable increased in U.S. since 1920, and less extreme events have occurred in some part of Canada (*Kunkel,* 2003). The average of precipitation has increased by more than 10% in Canada over the 20th century (*Groisman* and *Easterling,* 1994; *Mekis* and *Hogg*, 1999; *Akinremi et al*., 2001*; Cutforth et al.,* 2001). Heavy daily rainfall interrelated with global warming because of atmospheric water vapor and warmer air (*Solomon* and *Srinivasan*, 1995). Increased variance of precipitation has occurred everywhere that wet areas become wetter and arid areas become drier. Overall, precipitation increased at high latitudes (Northern Hemisphere), decreased in China, Australia, and the Small Island States in the Pacific, and its variance increased in equatorial regions. The changes in the major ocean currents also appear to be affecting precipitation patterns. For example, increased intensity and frequency of El Niño and ENSO seem to be associated with the evidence of an observed ‘‘dipole’’ pattern affecting Africa and Asia, although this time series is too short so far (*Dore*, 2005). The number and fequency of extremely intensive rainfalls were reduced in the southwestern and western parts of Australia, conversely, an increase in the extreme events can be observed in the eastern part of Australia (*Allan* and *Haylock*, 1993; *Nicholls* and *Lavery*, 1992: *Suppiah* and *Hennessy*, 1998; *Haylock* and *Nicholls*, 2000; *Hope et al*., 2010). The trend analysis of precipitation showed an upward trend in the annual rainfall over the period of 1955 to 2009 in the San Juan metropolitan area in Puerto Rico (*Méndez-Lázaro et al*., 2014). The study shows, that in the semi-arid Botswana, the rainfall variability decreased with a reduction of rainy days and a rise of drying throughout the area (*Batisani* and *Yarnal*, 2010). In Spain, plant cover change has occurred in the Mediterranean climate, and it is associated with an evolution of temperature and precipitation. The results shows a several decrease in the water supply with high dependence on precipitation (*Ceballos-Barbancho et al*., 2008). The annual precipitation has slightly decreased throughout China over the last five decades (*Zhai et al*., 2011). Conversely, the heaviest precipitations have significantly raised over the Yangtze River and West China during the last decades of the 20th century, while a reduction in the precipitation can be observed over the northern part of China (*Zhai et al.,* 1999b). Also, heavy precipitation and flash flood have occurred in the Caribbean (*Laing*, 2004). The precipitation has remarkably increased over Europe in the decades of the 20th century, while a downward trend shows a decline southward to the Mediterranean (*Schönwiese* and *Rapp*, 2013).

Scientific resuls reveal that the trend of extreme rainfalls has been reduced remarkably over Southeast Asia and the western and central parts of the South Pacific in the period of 1965 to 1998 (*Manton et al*., 2001). Severity of precipitation in South and Central Asia shows little change with positive and negative trends during 1961–2000 (*Klein Tank et al*., 2006). Rainfall trends revealed a significant decrease in the southwest monsoon rainfall and an increase in the post-monsoon season in India (*Krishnakumar et al*., 2009). The precipitation decreased in the winter and post-monsoon seasons and raised in the monsoon and pre-monsoon seasons in the China-Pakistan economic corridor over the period of 1980–2016 (*Ullah et al*., 2019). A downward trend of precipitation can be shown in the West, Northwest, and Southwest, but an upward trend can be indicated in the most stations of Iran during 1960–2001(*Boroujerdy*, 2008). Long-term rainfall prediction is very important to countries thriving on agro-based economy. In Afghanistan, precipitation variation is poorly documented because of the inadequate spatial and temporal data coverage. The annual precipitation has been reduced in the North and West, while it raised at the rest of parts of Afghanistan (*Saboory* and *Tomer,* 2019). The annual precipitation presented reduction trend in the Kunduz River Basin on the northeastern part of Afghanistan during 1961 to 2010 (*Hassanyar et al*., 2018). Based on climate records and data available from the neighboring countries, the average precipitation has declined by 0.5 mm or 2% per decade since 1960 (*Aich et al*., 2017). The aim of this research is to investigate the precipitation series and their trends. Rainfall trend could be an evidence of climate change. In this study, due to the importance of precipitation in terms of agriculture, water resources, and energy production, time changes and the existence of rainfall changes in Afghanistan are discussed.

2. Materials and methods

2.1. Study area

Afghanistan is a vast country with an area of 647,500 km^2 and an estimated population 32.9 million people. Geographically it is located approximately between the 29–38 °N latitudes and 61–74 °E longitudes in the central zone of Asia, and a part of the country is located within the Hindu-Kush Himalayan region *Fig. 1*). Afghanistan has a predominantly dry continental climate, and the quantity and distribution of precipitation is key factor to recharge of water availability. Three-quarter of precipitation is occurring as snow during winter, where altitudes are more than 2500 m. The annual precipitation is less than 400 mm over the 75% of the country and higher values occur above 1000 m on in the mountains of the northwest. The temperature is approximately 33 °C in summer and 10 °C in winter, but in cold areas temperature could fall below -20 °C (*McSweeney et al*., 2013). Afghanistan’s climate is arid to semi-arid with major daytime and nighttime temperature fluctuations. The annual precipitation ranges from less than 50 mm/year in the southwestern part of Afghanistan to 1000 mm/year in the northeastern highland. The monthly precipitation changes between 20 to 80 mm in winter and spring, and it is remarkably below 3 mm in summer, i.e., in the period of June to October (*Tünnermeier et al*., 2005).

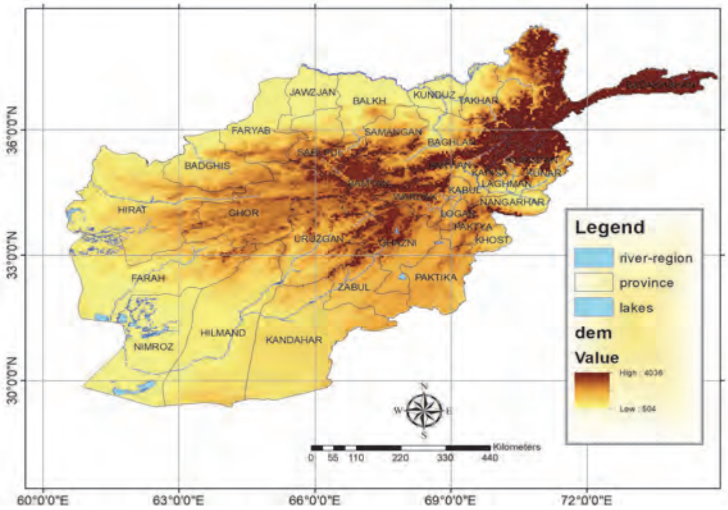

Fig. 1. Location of study area.

Daily precipitation data was obtained from the CPC-NOAA (Climate Prediction Center - National Oceanic Atmospheric Administration) website: https://psl.noaa.gov/data/gridded/data.cpc.global temp.html for the period of 1979–2019. The CPC spatial resolution of daily precipitation is 0.5×0.5 degree. Daily precipitation data were extracted for 33 provinces of Afghanistan covering the whole of the study area, except for the Bamyan province. The capital of every province chosen for the study, with specified latitudes, longitudes, and elevations are shown in *Table 1*.

The study examined the trend in observation time series of precipitation. For qualitative and quantitative analysis of data, the Run Test method was used, all data was normal. The data were validated in order to estimate the robustness of the results. Thus, reanalysis data were compared to observed data of some weather stations of the same time. According to the normal distribution of rainfall, linear regression could be used for the analysis of precipitation trend.

Table 1: Specific locations of the study area in Afghanistan

Provinces	**Study sites**	**Latitude (ºN)**	**Longitude (ºE)**	**Elevation (m.a.s.l.)**
Balkh	Balkh	36.75	66.89	348
Nangarhar	Jalalabad	34.41	70.47	568
Helmand	Lashkar-Gah	31.62	64.36	787
Kandahar	Aino-Mainah	31.63	65.77	1025
Zabul	Hazari	32.11	66.91	1579
Ghazni	Naw Adad	33.58	68.40	2225
Nimroz	Zaranj	30.96	61.87	489
Farah	Arg-Farah	32.37	62.10	660
Herat	Taraqi Park	34.34	62.21	933
Badghis	Qala-e- Naw	34.97	63.13	956
Paktika	Urgun	32.85	69.14	2321
Oruzgan	Khas Oruzgan	32.92	66.69	2211
Faryab	Afghan Kot	35.91	64.78	882
Sar-e-Pole	Sar-e-Pole	36.21	65.93	634
Jowzjan	Sheberghan	36.66	65.75	362
Samangan	Takht-Rostam	36.24	68.02	1027
Baghlan	Pol-e-Khomri	35.94	68.70	649
Kunduz	Kunduz	36.70	68.84	382
Takhar	Taleqan	36.73	69.53	802
Badakhshan	Fyz-Abad	37.10	70.53	1183
Panjshir	Bazark	35.31	69.51	1959
Kapisa	Mahmude-Raqi	35.01	69.34	1436
Parvan	Charikar	35.02	69.16	1604
Kabul,	Bagh-Bala	34.53	69.12	1848
Vardak	Maidan-Shahr	34.38	68.85	2182
Daykundi	Nili	33.73	66.14	2103
Ghowr	Chegcharan	34.52	65.25	2265
Paktia	Gardez	33.59	69.21	2308
Khost	Khost	33.33	69.92	1174
Nuristan	Parun	35.42	70.92	2758
Konar	Asadabad	34.87	71.15	819
Laghman	Mihtar-lam	34.66	70.21	758
Lowgar	Pole-Alam	34.00	69.01	1912

One method of trend analysis of time series is using linear regression models. In this model, the main assumption considers time series that contain a linear regression. Although this assumption is not implemented completely, it provides general overview of the time series. The linear regression is defined as follows:

$$Z_T = a + bT + e_T, \tag{1}$$

where Z_T is the climate variable, T is the time (T=1, 2, 3……n), b is the slope of line (change except of time), e_T is the error (residual or deviation) of the estimation, and a and b is are the regression coefficients (*Asakereh*, 2009). This study is used the method of least squares, the main objective of which is to fit a curve through the time series, so that the sum of the least square errors is minimum. The estimation of regression coefficient the method of least square is:

$$b = \frac{\sum_{i=1}^{n}(T_i - \overline{T})(Z_i - \overline{Z})}{\sum_{i=1}^{n} T_i - \overline{T}}, \tag{2}$$

$$a = \overline{Z} - b\overline{T}$$

where $\overline{T}$ and $\overline{Z}$ are the mean of time and the mean of the climate parameter, respectively.

3. Discussion

3.1. Precipitation trend in the north

The analysis of rainfall data in the northern part of Afghanistan shows mostly reduction in precipitation over the period of 1979 to 2019. Data reveal decreasing precipitation trend in the northeastern provinces: data show a declining trend of -1.14 mm/year and a minimum rainfall of 69 mm in Baghlan, -0.25 mm/year and 88 mm in Kunduz, -2.56 mm/year and 111mm in Takhtar, and -5.85 mm/year in Badakhsan in 2000. Samangan and Faryab provinces shown a decrease in the average of rainfall (-0.38 mm/year and -0.49 mm/year), the minimum rainfall was 64 mm in 2001 and 72 mm in 2014, respectively. Balkh, Sar-e-Pole, and Jowzjan provinces represent a slight increase in precipitation with 0.63 mm/y, 0.75 mm/y, and 0.93 mm/y, the minimum amount of precipitation was 51 mm, 54 mm and 55 mm in 2001, respectively. Overall, the reduction in the precipitation trend was -9.2 mm per decade in the northern part of Afghanistan during study period. Similarly, the result of study *Salma et al.* (2012) shows a decreasing rainfall trend all over the Pakistan. The mean annual rainfall exhibits reduced trend in Russia, some part of Japan, North China, most parts of Northeast India, Indonesia, and Philippines (*Solomon et al.,* 2007). Conversely, the study carried out in the arid

Central Asia reveals an upward trend in precipitation during the past 80 years (*Chen et al*., 2011). The extreme precipitation events observed in summer ranged from 50 mm/day to 100 mm/day in North Xinjiang during 1951–2014 (*Huang et al*., 2017). Comparing the results with those of other researchers in neighboring countries such Iran and Pakistan, an absolute homogeneity assessment of precipitation time series in the arid region of Pakistan found them doubtful for the month of June at two stations (*Kamal et al*., 2018). Rainfall trend analysis of Iran in the last half of the twentieth century was performed. This study shows that the annual rainfall is decreasing at 67% of the stations, while the 24-hour maximum rainfall is increasing at 50% of the stations (*Figs. 2–7*) (*Modarres* and *Sarhadi*, 2009).

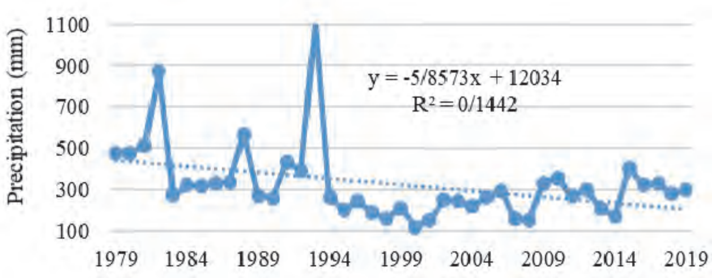

Fig. 2. Mean annual precipitation of Badakhshan province.

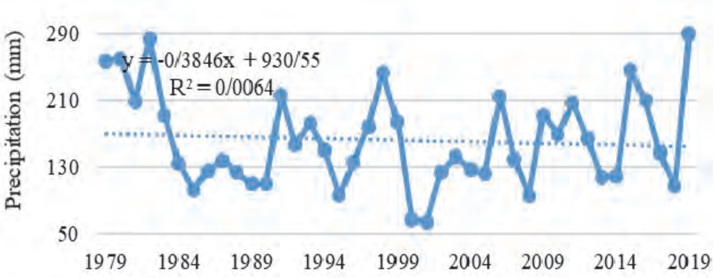

Fig. 3. Mean annual precipitation of Samangan province.

3.2. *Changes in the precipitation in the west and south*

This investigation has shown a decreasing trend in the precipitation in all western and southern provinces of Afghanistan. In the southern provinces, a significant reduction in precipitation has been observed in Helmand, Kandahar, Zabul, and Nimruz provinces with the value of -3.24 mm/y, -3.27 mm/year, -1.09 mm/year, and -0.35 mm/year, and the minimum precipitation was 4 mm, 28 mm, 54 mm, and 6 mm in 2018 and 2001, respectively. Ghazni and Uruzgan provinces show a positive trend of precipitation in the southern part of Afghanistan. The result is consistent with findings of other researchers: *Ahmad et al.* (2015) highlighted negative and positive trends of precipitation during 1961 to 2011 in the Swat River Basin, Pakistan. Rainfall was increasing during summer while decreasing in winter over the period of 1945–2004 in Faisalabad (*Cheema et al.*, 2006). Studies examined the latitudinal precipitation trend in Pakistan, which show raise in high latitudes and no noteworthy trend in lower latitudes (*Hanif et al.,* 2013; *Ahmad et al.*, 2014). The Panjab has experienced a significant increasing precipitation trend during 1961–2014 (*Khattak* and *Ali*, 2015). The finding of *Sheikh et al.* (2015) indicates most extreme precipitation raise in South Asia, consistent with the globally averaged result.

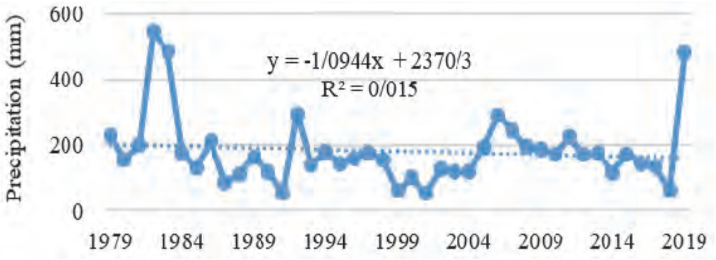

Fig. 4. Mean annual precipitation of Zabul province.

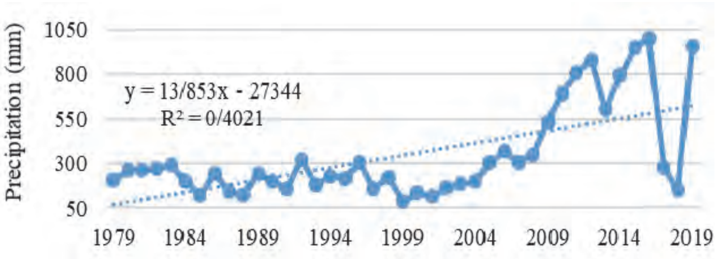

Fig. 5. Mean annual precipitation of Ghazni province.

Data in *Table 2* shows that the mean annul precipitation decreased over the study period in the western part of Afghanistan. Data show a high declining trend of -0.44 mm/year in Farah province in the West, -0.19 mm/year in Herat and 0.17 mm/year in Badghis province. Generally, the average decline of precipitation is -2.44 mm/year per decade. The result of this study is in a good agreement with the report of *Modarres* and *Sarhadi* (2009), which presents negative trend of annual rainfall in the northern and northwestern parts of Iran in the last decades of twentieth century. *Nasri* and *Modarres* (2009) carried out a study in the western and eastern parts of Iran receiving similar results: negative trend of precipitation. The finding of *Raziei et al.* (2005) indicated mostly downward trend of precipitation in the arid and semi-arid regions of Iran (*Modarres* and *da Silva*, 2007; *Tabari et al.,* 2012). A study conducted by *Sadeghi* and *Hazbavi* (2015) has shown a small general reduction trend in the seasonal rainfall in Iran in the period 1970–1992.

Table 2. Changes in precipitation across Afghanistan over the period of 1979 to 2019

Location	**Mean change of precipitation per year (mm)**	**Precipitation variation (mm)**
Balkh	0.63	25
Jalalabad	9.64	395
Lashkar-Gah	-3.24	-133
Aino-Mainah	-3.27	-134
Hazari	-1.09	- 44
Naw Adad	13.85	567
Zaranj	-0.35	- 14
Arg-Farah	-0.44	- 18
Taraqi Park	-0.19	- 8
Qala-e- Naw	-0.17	- 7
Urgun	15.44	663
Khas Oruzgan	2.85	116
Afghan Kot	-0.49	- 20
Sar-e-Pole	0.75	30
Sheberghan	0.93	38
Takht-Rostam	-0.38	- 16
Pol-e-Khomri	-1.14	- 47
Kunduz	-0.25	- 10
Taleqan	-2.56	- 105
Fyz-Abad	-5.85	- 240
Bazark	-1.44	- 59

Table 2. Continued

Location	Mean change of precipitation per year (mm)	Precipitation variation (mm)
Mahmude-Raqi	3.71	152
Charikar	2.40	98
Bagh-Bala	9.21	378
Maidan-Shahr	9.21	378
Nili	2.73	112
Chegcharan	0.44	18
Gardez	15.83	649
Khost	19.66	806
Parun	1.34	55
Asadabad	6.14	252
Mihtar-lam	10.30	423
Pole-Alam	13.53	555

3.3. Precipitation trend in the central regions

The central part of Afghanistan is characterized by low and highly variable precipitation due to the Himalayan mountain ranges. Farther south, monsoon effects moderate the climate near the Pakistan border and increases the rainfall as far inland as central part of Afghanistan. According to the 1979–2019 period, the mean annual rainfall increased in six provinces in the central region except Panjshir province, where it decreased by -1.44 mm/year. *Fig. 2* shows the mean annual precipitation trend of seven provinces in the central region indicating raise of 37.5mm per decade in Kabul, while in Vardak the precipitation increased by 9.21 mm per year. In Growr, the precipitation regions: 0.44 mm/year. Eastern regions include eight provinces, and the eastern highland is covering the smallest area that is mainly covered by rangeland and largest existing forests. This regions are directly influenced by the moist air masses of Indian monsoon getting trapped at the high mountain slopes, which can lead to the increase of rain. *Table 2* reveals upward trend of precipitation in the eastern regions: Khost, Paktia, Paktika, Lowgar, and Laghman show high rainfall rates 19.6 mm, 15.8 mm, 15.4 mm, 13.5 mm, and 10.3 mm per year, respectively.

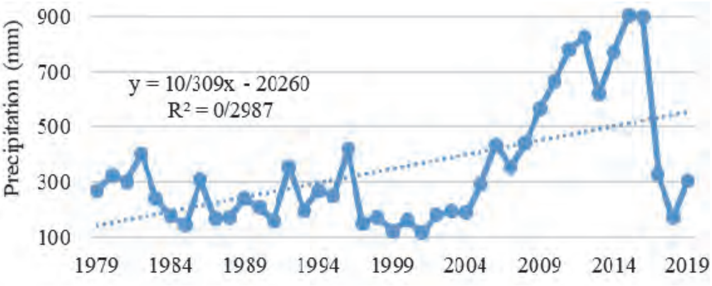

Fig. 6. Mean annual precipitation of Laghman province.

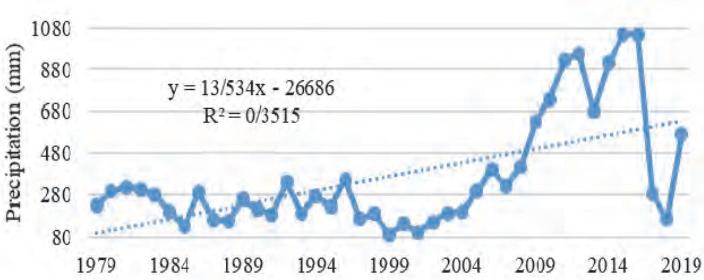

Fig. 7. Mean annual precipitation of Lowgar province.

The rest of provinces in the eastern area show lower rates of rainfall in the study period. Overall, the mean precipitation trend increased by 114.5 mm per decade. The result of this study is similar to the findings of *Alexander et al*. (2006) showing significant increases of precipitation. The findings of *Keggenhoff et al.* (2014) indicated that heavy and extremely heavy precipitation to total precipitation have increased between 1971 to 2010 in Georgia. Studies carried out in Pakistan, that have argued upward annual precipitation trend in the northern highland and sub-Himalayan ranges (*Iqbal et al.,* 2019; *Ahmed et al*., 2017; *Hussain* and *Lee*, 2013). Recent study of *Gajbhiye et al.,* (2016) further outlined a significant increasing of precipitation in both seasonal and annual rainfall amounts during 1901 to 2002 in the Sindh River Basin, India. A research was conducted by *Sen Roy* (2009), which investigated raising trends in extreme heavy precipitation in the high elevation parts of India. Ont he contrary to this study, significant decreasing trends of precipitation, *Martinez et al.* (2012) revealing the precipitation has negative trend in October and May in Florida. Other studies mostly observed negative trend on monthly rainy days in Iran (*Soltani et al*., 2012; *Rahimzadeh et al*., 2009). Also, the findings of studies mostly noticed decreasing trends in precipitation over Iran (*Some'e et al*., 2012; *Tabar*i and *Talaee*, 2011). A study assessed by *Zhai et al.* (2005) revealed that the annual precipitation decreased over the southern northeast parts of China, while a significant increase was detected in western region.

4. Conclusion

This study identified the mean annual trend in precipitation of 33 provinces from the 34 provinces of Afghanistan from 1979 to 2019. The center of each province was selected as study site with specific latitudes, longitudes, and elevations. The method used was the non-parametric linear regression trend in time series for rainfall parameters. The trend of precipitation may be attributed to the regional climate changes, local land use, and high emission of greenhouse gases from various sources, i.e., population density, industry, infrastructure, building, transport, agriculture, deforestation, and rearing livestock. The daily precipitation data were extracted from the database of CPC-NOAA (Climate Prediction Center - National Oceanic Atmospheric Administration), and they were analyzed by the linear regression trend. The analysis of rainfall data shows a declining trend in the northeastern provinces such as Baghlan, Kunduz, Takhar, and Badakhshan. Samangan and Faryab indicated a negative trend of precipitation, while Balkh, Sar-e-Pole, and Samangan were revealed with slight increase on precipitation trend in the northern part of Afghanistan showing -9.2mm per decade generally. In the south, a significant reduction was observed in the precipitation trend in Helmand, Kandahar, and Nimruz provinces, but Ghazni and Uruzgan showed positive trend. *Table 2* revealed that the mean annual precipitation significantly decreased in the western part of Afghanistan. Central parts of Afghanistan are characterized by low and highly variable precipitation due to Himalayan mountain ranges. Farther south, the monsoon effects moderate the climate near the Pakistan border and increases rainfall as far inland as the central parts of Afghanistan. According to the 1979–2019 period, the mean annual rainfall increase in six provinces in central region except Panjshir province decrease -1.44 mm per year. *Fig. 2* shows the mean annual precipitation trend of seven provinces in the central region indicating raise of 37.5 mm per decade in Kabul, while in Vardak, while in the highest precipitation increase was 9.21 mm per year. Eastern regions include eight provinces, and the eastern highland is covering the smallest area, which is mainly covered by rangeland and the largest existing forests. This regions are directly influenced by the moist air masses of Indian monsoon getting trapped at the high mountain slopes, and it can lead to the increase of rain. Data reveals upward trend of precipitation in the eastern regions, that Khost, Paktia, Paktika, Lowgar, and Laghman showed high rainfall rate, and the rest of provinces in the eastern area showed lower rate of rainfall in the study period.

References

Ahmad, I., Tang, D., Wang, T., Wang, M., and *Wagan, B*., 2015: Precipitation trends over time using Mann-Kendall and spearman's rho tests in swat river basin, Pakistan. *Adv. Meteorol. 2015,* 431860. https://doi.org/10.1155/2015/431860

Ahmad, W., Fatima, A., Awan, U.K., and *Anwar, A*., 2014: Analysis of long term meteorological trends in the middle and lower Indus Basin of Pakistan—A non-parametric statistical approach. *Glob. Planet. Change 122*, 282–291. https://doi.org/10.1016/j.gloplacha.2014.09.007

Ahmed, K., Shamsuddin, S., Eun-Sung, C., Tarmizi, I., and *Xiao-Jun, W*., 2017: Spatial distribution of secular trends in annual and seasonal precipitation over Pakistan. *Climate Res. 74*, 95–107. https://doi.org/10.3354/cr01489

Aich, V., Akhundzadah, N.A., Knuerr, A., Khoshbeen, A.J., Hattermann, F., Paeth, H., and *Paton, E.N*., 2017: Climate Change in Afghanistan Deduced from Reanalysis and Coordinated Regional Climate Downscaling Experiment (CORDEX)—South Asia Simulations. *Climate*, 5(2), 38. https://doi.org/10.3390/cli5020038

Akinremi, O.O., McGinn, S.M., and *Cutforth, H.W*., 2001: Seasonal and spatial patterns of rainfall trends on the Canadian prairies. *J. Climate 14*, 2177–2182. https://doi.org/10.1175/1520-0442(2001)014<2177:SASPOR>2.0.CO;2

Alexander, L.V., Zhang, X., Peterson, T.C., Caesar, J., Gleason, B., Klein Tank, A.M.G., ... and *Tagipour, A.,* 2006: Global observed changes in daily climate extremes of temperature and precipitation. *J. Geophys. Res.*: *Atmos.*, 111(D5). https://doi.org/10.1029/2005JD006290

Allan, R.J. and *Haylock, M.R.,* 1993: Circulation features associated with the winter rainfall decrease in southwestern Australia. *J. Climate* 6, 1356–1367. https://doi.org/10.1175/1520-0442(1993)006<1356:CFAWTW>2.0.CO;2

Asakereh, H. 2009: Power spectrum analysis of the time series of Tabriz annual temperature.

Batisani, N. and *Yarnal, B.,* 2010: Rainfall variability and trends in semi-arid Botswana: implications for climate change adaptation policy. *Appl. Geograp.*, 30, 483–489. https://doi.org/10.1016/j.apgeog.2009.10.007

Boroujerdy, P. K., 2008: the analysis of precipitation variation and quantiles in Iran. In Proceedings of the 3rd WSEAS International Conference on Energy and Environment, University of Cambridge, UK, 248–253.

Cannarozzo, M., Noto, L.V., and *Viola, F*. 2006: Spatial distribution of rainfall trends in Sicily (1921–2000). *Phys. Chem. Earth*, *31*, 1201–1211. https://doi.org/10.1016/j.pce.2006.03.022

Ceballos-Barbancho, A., Morán-Tejeda, E., Luengo-Ugidos, M.Á., and *Llorente-Pinto, J.M.,* 2008: Water resources and environmental change in a Mediterranean environment: the south-west sector of the Duero river basin (Spain). *J. Hydrol. 351*, 126–138. https://doi.org/10.1016/j.jhydrol.2007.12.004

Cheema, M.A., Farooq, M., Ahmad, R., and *Munir, H.,* 2006: Climatic trends in Faisalabad (Pakistan) over the last 60 years (1945-2004). *J. Agric. Social Sci. 2*, 42–45.

Chen, F., Huang, W., Jin, L., Chen, J., and *Wang, J.,* 2011: Spatiotemporal precipitation variations in the arid Central Asia in the context of global warming. *Sci. China Earth Sci. 54*, 1812–1821. https://doi.org/10.1007/s11430-011-4333-8

Cutforth, H.W., Akinremi, O.O., and *McGinn, S.M.,* 2001: Seasonal and spatial patterns of rainfall trends on the Canadian prairie. In Soils and Crops Workshop. *J. Climate 14*, 2177–2182. https://doi.org/10.1175/1520-0442(2001)014<2177:SASPOR>2.0.CO;2

Dai, A., Fung, I.Y., and *Del Genio, A.D.,* 1997: Surface observed global land precipitation variations during 1900–88. *J. Climate 10*, 2943–2962. https://doi.org/10.1175/1520-0442(1997)010<2943:SOGLPV>2.0.CO;2

Dore, M.H., 2005: Climate change and changes in global precipitation patterns: what do we know? *Environ. Int. 31*, 1167–1181. https://doi.org/10.1016/j.envint.2005.03.004

Frei, A., Robinson, D.A., and *Hughes, M.G.,* 1999: North American snow extent: 1900–1994. *Int. J. Climatol. 19*, 1517–1534. https://doi.org/10.1002/(SICI)1097-0088(19991130)19:14<1517::AID-JOC437>3.0.CO;2-I

Gajbhiye, S., Meshram, C., Singh, S.K., Srivastava, P.K., and *Islam, T.,* 2016: Precipitation trend analysis of Sindh River basin, India, from 102-year record (1901–2002). *Atmos. Sci. Lett. 17*, 71–77. https://doi.org/10.1002/asl.602

Groisman, P., Karl, T., Easterling, D., Knight, R., Jamason, P., Hennessy, K., Suppiah, R., Page, C., Wibig, J., Fortuniak, K., Razuvaev, V., Douglas, A., Førland, E., and *Zhai, P*., 1999: Changes in the probability of extreme precipitation: important indicators of climate change. *Climat. Change 42*, 243–283. https://doi.org/10.1023/A:1005432803188

Groisman, P. Y., and Easterling, D. R. 1994: Variability and trends of total precipitation and snowfall over the United States and Canada. *Journal of Climate*, 7(1), 184-205. https://doi.org/10.1175/1520-0442(1994)007<0184:VATOTP>2.0.CO;2

Hanif, M., Khan, A.H., and *Adnan, S*., 2013: Latitudinal precipitation characteristics and trends in Pakistan. *J. Hydrol. 492*, 266–272. https://doi.org/10.1016/j.jhydrol.2013.03.040

Hassanyar, M.H., Tsutsumi, J.I.G., Nakamatsu, R., and *Omid, S.M.,* 2018: The Analysis Of Temporal Variability, Trend Of Precipitation And River Discharge Of Kunduz River Basin, *Afghanistan. Manage. Res.* 5(4), 69–78. https://doi.org/10.29121/ijetmr.v5.i4.2018.210

Haylock, M. and *Nicholls, N.,* 2000: Trends in extreme rainfall indices for an updated high quality data set for Australia, 1910–1998. *Int. J. Climatol. 20*, 1533–1541. https://doi.org/10.1002/1097-0088(20001115)20:13<1533::AID-JOC586>3.0.CO;2-J

Hope, P., Timbal, B., and *Fawcett, R.,* 2010: Associations between rainfall variability in the southwest and southeast of Australia and their evolution through time. *Int. J. Climatol. 30*, 1360-1371. https://doi.org/10.1002/joc.1964

Houghton, E., 1996: Climate change 1995: The science of climate change: contribution of working group I to the second assessment report of the Intergovernmental Panel on Climate Change (Vol. 2). Cambridge University Press.

Huang, W., Chang, S.Q., Xie, C.L., and *Zhang, Z.P.,* 2017: Moisture sources of extreme summer precipitation events in North Xinjiang and their relationship with atmospheric circulation. Advances in Climate, *Change Res. 8*, 12–17. https://doi.org/10.1016/j.accre.2017.02.001

Hussain, M.S. and *Lee, S.,* 2013: The regional and the seasonal variability of extreme precipitation trends in Pakistan. *Asia-Pacific J. Atmos. Sci. 49*, 421–441. https://doi.org/10.1007/s13143-013-0039-5

Iqbal, Z., Shahid, S., Ahmed, K., Ismail, T., and *Nawaz, N.,* 2019: Spatial distribution of the trends in precipitation and precipitation extremes in the sub-Himalayan region of Pakistan. *Theor. Appl. Climatol. 137,* 2755–2769. https://doi.org/10.1007/s00704-019-02773-4

Kamal, A., Shamsodin, S., Tarmmizi, I., Nadeem, N., and Xio, W., 2018: Absolute homogeneity assessment of precipitation time series in an arid region of Pakistan. *Atmosfera 31*, 301–316. https://doi.org/10.20937/ATM.2018.31.03.06

Karl, T.R., Nicholls, N., and *Ghazi, A.,* 1999: In: Weather Climate Extremes Clivar/GCOS/WMO workshop on indices and indicators for climate extremes workshop summary. 3–7. https://doi.org/10.1007/978-94-015-9265-9_2

Karl, R. and *Knight, R.,*1998:Secular Trends of Precipitation Amount, Frequency, and Intensity in the United States, *Bull. Amer. Meteorol. Soc. 79*, 231–242. https://doi.org/10.1175/1520-0477

Keggenhoff, I., Elizbarashvili, M., Amiri-Farahani, A., and *King, L.* 2014: Trends in daily temperature and precipitation extremes over Georgia, 1971–2010. *Weather Climate Extrem. 4*, 75–85. https://doi.org/10.1016/j.wace.2014.05.001

Khattak, M.S. and *Ali, S.,* 2015: Assessment of temperature and rainfall trends in Punjab province of Pakistan for the period 1961-2014. *J.f Himalayan Earth Sci. 48(2).*

Klein Tank, A.M.G., Peterson, T.C., Quadir, D.A., Dorji, S., Zou, X., Tang, H., ... and Sikder, A. B. 2006: Changes in daily temperature and precipitation extremes in central and south Asia. *J. Geophys. Res.: Atmos.*, 111(D16). https://doi.org/10.1029/2005JD006316

Kreft, S.; Eckstein, D.; Dorsch, L., and *Fischer, L.,* 2015: Global Climate Risk Index 2016: Who Suffers Most from Extreme. Think Tank and Research. Germanwatch. https://germanwatch.org/sites/default/files/publication/13503.pdf

Krishnakumar, K.N., G.S.L.H.V. Prasada Rao, and *C S. Gopakumar*, 2009: Rainfall trends in twentieth century overKerala, India. *Atmos. Environ. 43*, 1940–1944. https://doi.org/10.1016/j.atmosenv.2008.12.053

Kunkel, K.E., 2003: North American trends in extreme precipitation. *Natural Hazards 29*, 291–305. https://doi.org/10.1023/A:1023694115864

Kunkel, K.E., Andsager, K., and *Easterling, D.R.,* 1999: Long-term trends in extreme precipitation events over the conterminous United States and Canada. *J. Climate 12*, 2515–2527. https://doi.org/10.1175/1520-0442(1999)012<2515:LTTIEP>2.0.CO;2

Laing, A.G., 2004: Cases of heavy precipitation and flash floods in the Caribbean during El Nino winters. *J Hydrometeorol. 5*, 577–594. https://doi.org/10.1175/1525-7541(2004)005<0577:COHPAF>2.0.CO;2

Manton, M.J., Della-Marta, P.M., Haylock, M.R., Hennessy, K.J., Nicholls, N., Chambers, L.E., and *Inape, K.,* 2001: Trends in extreme daily rainfall and temperature in Southeast Asia and the South Pacific: 1961–1998. *Int. J. Climatol.* 21, 269–284. https://doi.org/10.1002/joc.610

Martinez, C.J., Maleski, J.J., and *Miller, M.F.,* 2012: Trends in precipitation and temperature in Florida, USA. *J. Hydrol 452*, 259–281. https://doi.org/10.1016/j.jhydrol.2012.05.066

McSweeney, C., New, M., and *Lizcano, G.* 2013: UNDP climate change country profiles: Afghanistan.

Mekis, E. and *Hogg, W.D.,* 1999: Rehabilitation and analysis of Canadian daily precipitation time series. *Atmos.-ocean 37*, 53–85. https://doi.org/10.1080/07055900.1999.9649621

Méndez-Lázaro, P.A., Nieves-Santiango, A., and *Miranda-Bermúdez, J.,* 2014: Trends in total rainfall, heavy rain events, and number of dry days in San Juan, Puerto Rico, 1955-2009. *Ecol. Soc.* 19(2), 50. https://doi.org/10.5751/ES-06464-190250

Modarres, R. and *da Silva, V.* 2007: Rainfall trends in arid and semi-arid regions of Iran. *J. Arid Environ. 70*, 344–355. https://doi.org/10.1016/j.jaridenv.2006.12.024

Modarres, R. and *Sarhadi, A.,* 2009: Rainfall trends analysis of Iran in the last half of the twentieth century, *J. Geophys. Res. Atmos. 114(3),* 1–9. https://doi.org/10.1029/2008JD010707

Nasri, M. and *Modarres, R.,* 2009: Dry spell trend analysis of Isfahan Province, Iran. *Int. J. Climatol. 29*, 1430–1438. https://doi.org/10.1002/joc.1805

Nicholls, N. and *Lavery, B.,* 1992: Australian rainfall trends during the twentieth century. *Int. J. Climatol. 12*, 153–163. https://doi.org/10.1002/joc.3370120204

Pachauri, R. K., Allen, M. R., Barros, V. R., Broome, J., Cramer, W., Christ, R., ... and *van Ypserle, J.P., 2014.* Climate change 2014: synthesis report. Contribution of Working Groups I, II and III to the fifth assessment report of the Intergovernmental Panel on Climate Change, 151.

Rahimzadeh, F., Asgari, A., and *Fattahi, E.* 2009: Variability of extreme temperature and precipitation in Iran during recent decades. *Int. J. Climatol. 29*, 329–343. https://doi.org/10.1002/joc.1739

Raziei, T., Arasteh, P.D., and *Saghafian, B.,* 2005: Annual rainfall trend in arid and semi-arid regions of Iran. In ICID 21st European Regional Conference. 15–19.

Saboory, S.K., and *Tomer, S.K.,* 2019: Regional scale spatiotemporal trends of precipitation and temperatures over Afghanistan.

Sadeghi, S.H.R., and *Hazbavi, Z.* 2015: Trend analysis of the rainfall erosivity index at different time scales in Iran. *Nat.Hazard. 77*, 383–404. https://doi.org/10.1007/s11069-015-1607-z

Salma, S., Rehman, S., and Shah, M. A. 2012: Rainfall trends in different climate zones of Pakistan. *Pakistan J. Meteorol. 9(17)* 37–47.

Schönwiese, C.D. and *Rapp, J.* 2013: Climate trend atlas of Europe based on observations 1891–1990. Springer Science and Business Media.

Sen Roy, S. 2009: A spatial analysis of extreme hourly precipitation patterns in India. *Int. J. Climatol. 29*, 345–355. https://doi.org/10.1002/joc.1763

Sheikh, M.M., Manzoor, N., Ashraf, J., Adnan, M., Collins, D., Hameed, S. ... and *Islam, N.* 2015: Trends in extreme daily rainfall and temperature indices over South Asia. *Int. J. Climatol. 35*, 1625–1637. https://doi.org/10.1002/joc.4081

Sheila M. 2013: Climate change adaptation and water resource management: A review of the literature, Energy Economics, Available online 19 September 2013, ISSN 0140-9883.

Solomon, S.D et al., 2007*:* Climate Change 2007: The Physical Science Basis; IPPC. 2007; Contribution of Working Group I to the Fourth Assessment Report of the Intergovernmental Panel on Climate Change.

Solomon, S., and *Srinivasan, J.,* 1995: Radiative forcing of climate change. Climate change, 108-118, Cambridge University Press, New York.

Soltani, S., Saboohi, R., and *Yaghmaei, L.* 2012: Rainfall and rainy days trend in Iran. *Climatic Change 110*, 187–213. https://doi.org/10.1007/s10584-011-0146-1

Some'e, B.S., Ezani, A., and *Tabari, H.,* 2012: Spatiotemporal trends and change point of precipitation in Iran. *Atmos. Res. 113*, 1–12. https://doi.org/10.1016/j.atmosres.2012.04.016

Suppiah, R. and *Hennessy, K. J.* 1998: Trends in total rainfall, heavy rain events and number of dry days in Australia, 1910–1990. *Int. J. Climatol. 18*, 1141–1164. https://doi.org/10.1002/(SICI)1097-0088(199808)18:10<1141::AID-JOC286>3.0.CO;2-P

Tabari, H. and *Talaee, P.H.,* 2011: Temporal variability of precipitation over Iran: 1966–2005. *J. Hydrol. 396*, 313–320. https://doi.org/10.1016/j.jhydrol.2010.11.034

Tabari, H., Abghari, H., and *Hosseinzadeh Talaee, P.* 2012: Temporal trends and spatial characteristics of drought and rainfall in arid and semiarid regions of Iran. *Hydrol. Proc. 26*, 3351–3361. https://doi.org/10.1002/hyp.8460

Tünnermeier, T., Houben, G., and *Himmelsbach, T.* 2005: Hydrogeology of the Kabul Basin, part I: geology, aquifer characteristics, climate and hydrography. Foreign Office of the Federal Republic of Germany, *AA-Gz'GF07*, 885(3), 16.

Ullah, S., You, Q., Ullah, W., and *Ali, A.* 2018: Observed changes in precipitation in China-Pakistan economic corridor during 1980–2016. *Atmos. Res. 210*, 1–14. https://doi.org/10.1016/j.atmosres.2018.04.007

World Bank. 2014: Scoping Strategic Options for Development of the Kabul River Basin a multi- sector decision support system approach, document of World Bank.

Zhai, P., Sun, A., Ren, F., Liu, X., GAO, B., and *Zhang, Q.* 1999a. Changes of climate extremes in China. In Weather and Climate extremes (pp. 203-218). *Springer*, Dordrecht. https://doi.org/10.1007/978-94-015-9265-9_13

Zhai, P. M., Ren, F. M., and *Zhang, Q.* 1999b: Detection of trends in China's precipitation extremes. *Acta Meteorologica Sinica*, 57(2), 208–216.

Zhai, P., Zhang, X., Wan, H., and *Pan, X.* 2005: Trends in total precipitation and frequency of daily precipitation extremes over China. *J. Climate 18*, 1096–1108. https://doi.org/10.1175/JCLI-3318.1

DOI:10.28974/idojaras.2022.2.3

IDŐJÁRÁS

Quarterly Journal of the Hungarian Meteorological Service
Vol. 126, No. 2, April – June, 2022, pp. 203–232

Spatial effect of anti-COVID measures on land surface temperature (LST) in urban areas: A case study of a medium-sized city

Kamill Dániel Kovács* and **Ionel Haidu**

Université de Lorraine
Laboratoire LOTERR-EA7304
Île du Saulcy, 57045 Metz, France

**Corresponding author E-mail: kamill-daniel.kovacs@univ-lorraine.fr*

(Manuscript received in final form March 1, 2021)

Abstract— This case study investigates the magnitude and nature of the spatial effect generated by the anti-COVID measures on land surface temperature (LST) in the city of Târgu Mureș (Marosvásárhely), Romania. The measures were taken by the Romanian government during the state of emergency (March 16 – May 14, 2020) due to the SARS-CoV-2 coronavirus pandemic. The study shows that – contrary to previous studies carried out on cities in China and India – in most of the urban areas of Marosvásárhely LST has increased in the period of health emergency in 2020 concerning the large average of the years 2000–2019. Remote sensing data from the MODIS and the Landsat satellites show, that MODIS data, having a moderate spatial (approximately 1 km) but good temporal resolution (daily measurements), show a temperature increase of +0.78 °C, while Landsat data, having better spatial (30 m) but lower temporal resolution, show an even greater increase, +2.36 °C in the built-up areas. The difference in temperature increase is mainly due to the spatial resolution difference between the two TIR band sensors. The LST anomaly analysis performed with MODIS data also shows a positive anomaly increase of 1 °C. However, despite this increase, with the help of the hotspot-coldspot analysis of the Getis-Ord Gi* statistic we were able to identify 46 significant coldspots that showed a 1–2 °C decrease of LST in April 2020 compared to the average of the previous years in April. Most of these coldspots correspond to factory areas, public transport epicenters, shopping centers, industrial polygons, and non-residential areas. This shows that anti-COVID measures in the medium-sized city of Marosvásárhely had many effects on LST in particular areas that have links to the local economy, trade, and transport. Paired sample t-test for areas identified with LST decrease shows that there is a statistically significant difference in the average LST observed before and after anti-COVID measures were applied. MODIS-based LST is satisfactory for recognizing patterns and trends at large or moderate geographical scales. However, for a hotspot-coldspot analysis of the urban heat islands, it is more suitable to use Landsat data.

Key-words: LST, TIR band, thermal sensor, anti-COVID measures, spatial effect, urban heat islands, medium-sized city, hotspot-coldspot analysis, Getis-Ord Gi*, QGIS

1. Introduction

Space remote sensing is a technology that has undergone constant progress in recent years. Nowadays it is one of the methods for change analysis by studying the events that occur in the Earth's spheres. It allows the obtaining of several geophysical magnitudes and variables that are within the geographic space. Thermal remote sensing is a branch of spatial remote sensing that studies the Earth's temperature. This is done by measurements obtained by a sensor onboard a satellite platform or an aircraft containing a TIR (thermal infrared) band. This sensor measures the electromagnetic radiation emitted by the Earth's surface in the thermal infrared region of the electromagnetic spectrum (between 8 and 14 µm) emitted by the Earth's surface and atmosphere (*Sobrino et al.,* 2000). Therefore, land surface temperature (LST) allows us to indirectly study the qualitative and quantitative processes that occur on the Earth's surface, and thus, to analyze and model changes over time (*Quattrochi* and *Luvall*, 2004; *Kovács*, 2019; *Ursu*, 2019; *Kis et al.,* 2020).

Previous studies have shown that LST has experienced significant declines during the emergency of COVID-19 in cities of China and India, where strict quarantine policy measures were adopted. *Maithani et al.* (2020) has pointed out that areas with high building density had minimal LST decline, while large proportions of open spaces with medium or low building density had maxima LST declines. *Hadibasyir et al.* (2020), in their study on Wuhan city, China, have shown that during the COVID-19 emergency with applied policies of breaking the virus spread, LST was lower than the average of the last three years on the same dates. However, in these two cases large cities were studied that have greater impact on their environment than the medium-sized cities or small towns.

Other studies also addressed the effects of COVID-19 concerning changes detected in the environment (*Liu et al.,* 2020; *Tobías et al.,* 2020; *Xie* and *Zhu*, 2020; *Lin et al.,* 2020; *Ma et al.,* 2020; *Awasthi et al.*, 2021; *Agrawal et al.,* 2020; *Singh et al.,* 2020; *Patel et al.,* 2020). LST has a principal part in climate change topics, because directly or indirectly, land surface temperature influences other factors related to hydrology, agriculture, or the urban environment (*Avdan* and *Jovanovska Kaplan*, 2016). Researchers also describe that anthropogenic factors, in general, can have a significant effect on LST (*Buyantuyev* and *Wu*, 2010; *Li et al.,* 2016; *Meng* and *Dou,* 2016). Factors such as urbanization, general transport, large centers of public transport, industrial and residential activities are related to LST (*Yoo et al.,* 2017; *Wang et al.,* 2017).

The alterations in LST that occur in urban areas are mainly depending on the characteristics of the materials that form the buildings, orientation, density of buildings, and also there is the main factor of anthropogenic heat sources generated near the surface (*Maithani et al.,* 2020; *Zsebeházi* and *Szépszó,* 2020). With all this, the result is that the LST in urban areas is altered, modified artificially in contrast to the non-built-up areas. This is how the phenomenon of urban heat islands (UHI) appears *(Mathew et al.,* 2016; 2017; *Mukherjee et al.,* 2017; *Kikon et al.,* 2016; *Mallick et al.,* 2013; *Xu et al.,* 2012; *Imhoff et al.,* 2010; *Yuan* and *Bauer*, 2007; *Gallo et al.,* 1993; *Oke,* 1982).

With the help of remote sensing technology, by calculating LST, we can identify these heat islands and their changes in the urban environment. Therefore, these changes indirectly explain the effects of human activities within the urban environment.

This study analyzes the changes in land surface temperature that have occurred within the urban area of the city of Marosvásárhely in the reference period of March 16 –May14, 2020. The study compares and detects the changes that occurred in 2020 compared to a large average of the previous years between 2000–2019. The state of emergency in Romania due to the pandemic of SARS-CoV-2, a new respiratory disease, was declared on March 14, 2020, implemented on March16, and extended on April 15 by 30 days until May 14, by a government decree. The main measures adopted were the cancellation of classes at the pre-university and university levels, limitation of public transport, compulsory wearing of masks in enclosed spaces, partial limitation of mobility of persons (permitted only with a personal statement and indicating the purpose of the posting).

2. Study area and data

Târgu Mureș (Marosvásárhely) is the main town in the district of Mureș (Maros) in the historical region of Transylvania, Romania (46°32’44’’N 24°33’45’’E) (*Fig. 1*). According to the latest Romanian census (*Institutul Național de Statistică,* 2011), it has a population of 134,290 inhabitants, an area of 49.3 km^2, making it the 16th largest city in the country. It extends along the two banks of river terraces of the River Mureș (Maros). At the country level, it is an important center of the chemical industry (Azomureș), and also of pharmaceutical, textile, wood, and food industries.

The data used for calculating the surface temperature are remote sensing data from the MODIS and Landsat satellite sensors. Remote sensing technology makes LST measurements possible by satellites in different orbits, on a multi-temporal scale. However, these satellites provide data in different spatial and temporal resolutions (*Maithani et al.,* 2020; *Jensen,* 2015; *Ndossi* and *Avdan,* 2016).

LST data from two different sensors (MODIS and Landsat) have used in this study. The reason for choosing this method is to find the balance between the spatial and temporal resolution of the available data. MODIS/MOD11A1 provides daily LST data with a spatial resolution of approximately 1 km. MODIS/MOD11A2, in turn, provides data of an average of 8 days with the same spatial resolution. Instead, Landsat sensors provide data with a much better spatial resolution (30 m). The Landsat 4–5 TIR band (band 6,10.40 – 12.50 μm) obtains data at 120 m resolution, but it is resampled to 30 m. Landsat 7 band 6 (10.40 – 12.50 μm) acquires data at 60 m resolution, then it is resampled to 30 m. Landsat 7 acquires thermal data in two different bands (band 6H - high gain, band 6L - low gain). The gain difference is present, because it is essential for studies of different types and purposes.

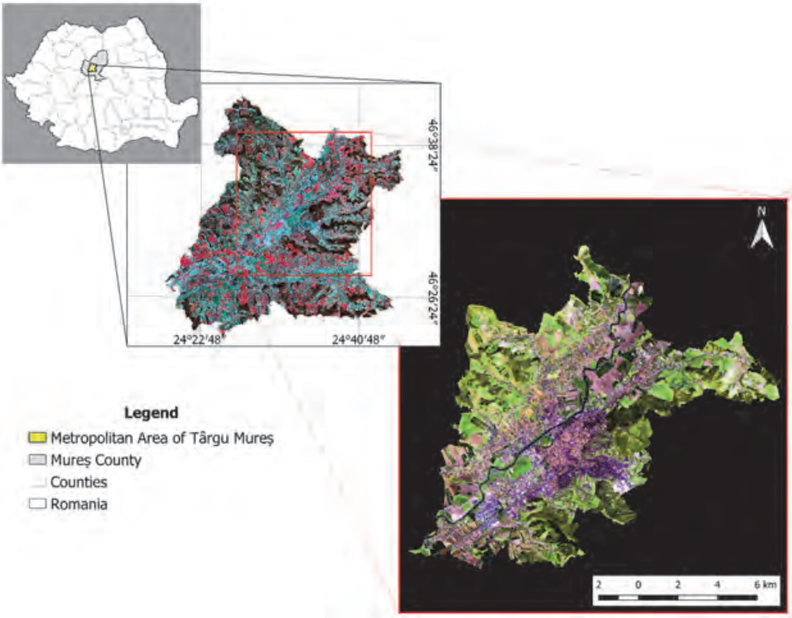

Fig. 1. Location of the functional urban area of Târgu Mureș (Marosvásárhely).

In this study, we have used band 6H (BAND_6_VCID_2), which has a higher radiometric resolution (sensitivity), a more restricted dynamic range, and is more likely to become saturated on hot objects. The reason for this choice is that the high gain setting is better for scenes that are in temperate zones, areas that have a lower surface luminosity, because the high gain has a temperature range between 240–320 K (*Karnieli et al.,* 2004; *Barsi et al.,* 2006; *Slater et al.,* 1987; *Donegan* and *Flynn,* 2004). Landsat 8 has two thermal infrared bands (TIRS): band 10 (10.60–11.19 μm) and band 11 (11.50–12.51 μm). In this study, we have used band 10, which is better in the calculation of current evapotranspiration, since it measures with high gain, while band 11 provides low gain (*Xu,* 2015; *Du et al.,* 2015; *Yu et al.,* 2014; *Xiao et al.,* 2007; *Rozenstein et al.,* 2014; *Sahana et al.,* 2016).

As we saw above, MODIS LST data has a lower spatial resolution (1 km) than Landsat (30 m). However, MODIS obtains daily data. Despite this, the

MODIS LST calculation continues to improve the cloud pollution removal, the update of the look-up table coefficient (LUT) for the split-window algorithm, and the classification to obtain emissivity. Also, studies have tested with ground validation methods that MODIS LST data show dependable accuracy (*Eleftheriou et al.,* 2018; *Hulley et al.,* 2012). On the other hand, the difficulty with using Landsat data is that they have a fairly long return period. Besides, from March to May (spring), in the temperate zones, such as where Marosvásárhely is located, clouds are more frequent in the scenes. Therefore, the effective temporal resolution (i.e., satellite images that can be used in the study period) can be greatly reduced. For this reason, we chose to use both MODIS LST and Landsat LST data to compare land surface temperature results. We have seen that the overall comparison results between 2020 and the long average of the years 2000–2019 of MODIS are corroborated with the results of Landsat and, knowing this, we have used the data of Landsat for the most in-depth analyses (hotspot-coldspot change detection analysis).

The Landsat data used are presented in *Table 1*. In the case of Landsat data, the reference date is a scene from the emergency period, which is April 8, 2020. Other satellite scenes have been searched in the previous years in the month of April with a maximum difference of 6 days to reduce the effect of the natural cycle of LST.

Landsat's NIR and RED bands have been downloaded from the Collection 2 Level 2 database, where the atmospheric effects on products are corrected. This step is crucial, because if the surface emissivity is calculated from the normalized vegetation index, on NIR and RED bands must be corrected atmospheric effects (*Dissanayake et al.,* 2019a, 2019b; *Ranagalage et al.,* 2018; *Sekertekin* and *Bonafoni,* 2020).

Table 1. Landsat data used

Landsat	Date	Difference from reference
L8	April 8, 2020	*reference*
L7	April 11, 2018	3 days
L7	April 5, 2016	3 days
L8	April 11, 2015	3 days
L8	April 8, 2014	0 days
L7	April 10, 2012	2 days
L5	April 13, 2010	5 days
L7	April 13, 2007	5 days
L7	April 7, 2005	1 day
L7	April 4, 2004	4 days
L7	April 2, 2003	6 days

TIR bands have been downloaded from Level 1 products, because in this study, LST was calculated with the radiative transfer equation (RTE), and this equation requires that the TIR band must be in digital numbers (DN) (0-255). Vector data referring to the boundaries of different urban area categories and administrative boundaries are derived from the Urban Atlas data of the Copernicus Programme. Data processing and obtaining the results were carried out with open source softwares Google Earth Engine and QGIS.

3. Techniques and methodology

There are different methods and algorithms for extracting LST from the TIR band (*Jiménez-Muñoz et al.,* 2014; *Sattari* and *Hashim,* 2014; *Mohamadi et al.,* 2019; *Hulley et al.,* 2019; *Dousset et al.,* 2019; *Weng,* 2019; *Vlassova et al.,* 2014; *Soleimani Vosta Kolaei* and *Akhoondzadeh,* 2018). This procedure is based on the inversion of the Planck's law and the brightness temperature obtained from the atmospheric radiance from the TIR band sensor (*Mathew et al.,* 2016).

The surface emissivity is also calculated, then these parameters along with the calibration coefficients are entered into an equation that calculates the LST estimation values. Other atmospheric corrections are also generally applied. The radiative transfer equation (RTE) has been used in this study to obtain the LST values (*Mallick et al.,* 2012; *Yu et al.,* 2014; *Wang* and *Upreti,* 2019; *Sobrino et al.,* 2004; *Sobrino* and *Romaguera*, 2004). The reference period of the study is March 16 – May 14. This period is analyzed in 2020 and in the previous years too (2000–2019). The reference period of 2020 has been chosen for all previous years to 2020 according to the health emergency period in 2020. This type of research should compare not only the LST variation before and after anti-COVID measures have been applied but also the LST in previous years in the same period of the year, thus avoiding the influence of regular changes of seasons of the year. The techniques and methodology of the study are detailed below.

3.1. LST extraction from MODIS data

MODIS11A2 and MODIS11A1 LST data were created based on a generalized split-window algorithm under cloud-free conditions (*Wan,* 2013; *Duan et al.,* 2019). The digital number (DN) values of MOD11A2 and MOD11A1 were calibrated to LST values in Kelvin scale by multiplying the DN with 0.02. From the obtained results, 273.15 were subtracted, thus the LST values in degrees Celsius were finally obtained. This whole process was done in Google Earth Engine using lines of JavaScript code.

The monthly temperature anomaly was calculated with MOD11A2 data with the following equation (*Ceccato et al.,* 2017):

$$r'_{ij} = r_{ij} - \frac{1}{N_i}\sum_{j=1}^{N} r_{ij}, \tag{1}$$

where *r'ij* is the monthly anomaly, *rij* is the original monthly value, and the rest of the equation is the calculation of the monthly climatology, which is subtracted from the original monthly values.

According to *Ceccato et al.* (2017), in climatology, anomaly means the difference between the value of a quantity and its mean climatological value. A monthly anomaly is a difference between the original monthly value of an amount in a given month and the monthly climatological value for that month of the year.

3.2. LST extraction from Landsat data

The authors have developed an automated processing model in QGIS Graphical Modeller for calculating the LST with Landsat satellite images. For Landsat 8, 7, and 5 products, three different models have been built, respectively. The difference between these models is that for Landsat 7 satellite images, a correction process of the gaps produced by the sensor's technique issue has been implemented in the model process, while for the other Landsat scene products, this step is not required (nor for Landsat 7 products before June 2003). In all models, cloud pixels have been excluded by identifying clouds with the BQA band of Level 1 by applying threshold values.

3.2.1. Vegetation indices and emissivity

The problem with estimating the Earth’s surface temperature with satellite data are the effects appear due to atmospheric absorption and surface emissivity. For the emissivity calculation, we have used the model presented by *Valor* and *Caselles* (1996). NIR and RED bands have been used which are atmospherically corrected (Level 2). NDVI has been calculated as follows (*Sellers,* 1985):

$$NDVI = \frac{(NIR-RED)}{(NIR+RED)}\ . \tag{2}$$

Based on the NDVI index, the vegetation proportion index (Pv) has been calculated. This calculation is necessary to isolate the thermal emissivity of the vegetation. These values (max and min NDVI) are taken as reference values (*Valor* and *Caselles*, 1996):

$$Pv = \left(\frac{(NDVI-NDVI_{min})}{(NDVI_{max}-NDVI_{min})}\right)^2\ . \tag{3}$$

This result is the basis for the calculation of emissivity. A typical value for vegetation in thermal infrared is 0.99. However, choosing a typical emissivity value for another type of soil is more complicated. We have taken the proposed value from 49 samples as reference from the Aster spectral library. In this case, the mean value is 0.986 with a standard deviation of 0.004:

$$\varepsilon = 0.004 * Pv + 0.986\,. \tag{4}$$

3.2.2. DN conversion to radiance

Landsat 7 and 5 data were converted to radiance using the spectral radiance scale method:

$$L_\lambda = \left(\frac{LMAX_\lambda - LMIN_\lambda}{Qcalmax - Qcalmin}\right) * (Qcal - Qcalmin) + LMIN_\lambda\,, \tag{5}$$

while Landsat 8 data were converted to radiance using the gain and bias method:

$$L_\lambda = ML * Qcal + AL\,, \tag{6}$$

where

$$ML = \left(\frac{LMAX_\lambda - LMIN_\lambda}{Qcalmax - Qcalmin}\right), \tag{7}$$

$$AL = LMIN_\lambda - \left(\frac{LMAX_\lambda - LMIN_\lambda}{Qcalmax - Qcalmin}\right) * Qcalmin\,. \tag{8}$$

In Eqs. (5–8), L_λ is the spectral radiance in the sensor (satellite radiance), *ML* is the band-specific reset multiplicative factor from the metadata (RADIANCE_MULT_BAND_x, where x is the band number), *AL* is the band-specific reset additive factor from the metadata (RADIANCE_MULT_BAND_x, where x is the band number), *Qcal* is the discretized and calibrated pixel values of the standard product (DN digital values), $LMAX_\lambda$ is the maximum spectral radiance corresponding to the band *Qcalx*, $LMIN_\lambda$ is the minimum spectral radiance corresponding to the band *Qcalx*, *Qcalmax* is the maximum pixel value depending on the radiometric resolution, *Qcalmin* is the minimum pixel value.

The problem with the transformation of radiance to land surface temperature is that dispersion and atmospheric transmission (effects produced by albedo and water vapor) alter values and give temperature values that do not correspond to the ground. For correcting these effects, a corrected radiative transfer equation has been used by applying it to the radiance obtained with the above equations (*Coll et al.,* 2010):

$$B(T) = \frac{L_{sen} - L^{\uparrow}}{\varepsilon\tau} - \frac{1-\varepsilon}{\varepsilon} L^{\downarrow}\,, \tag{9}$$

where L_{sen} is the radiance measured by the sensor (W/m^{-2}/sr^{-1}/µm^{-1}), ε is the emissivity of the surface, B is the parameter derived from the Planck's law calculated from the surface temperature calculation equation (°K), $L\downarrow$ is the descending atmospheric radiance (W/m^{-2}/sr^{-1}/µm^{-1}), τ is the atmospheric transmissivity, and $L\uparrow$ is the ascending atmospheric radiance (W/m^{-2}/sr^{-1}/µm^{-1}).

Parameters atmospheric transmissivity and ascending and descending radiance are not present in the metadata of satellite products. These parameters were obtained with the Atmospheric Correction Parameter Calculator tool available online (*Barsi et al.,* 2003). In the calculator data on temperature, altitude, atmospheric pressure, and relative humidity can be introduced. These data were acquired from the National Climatic Data Center of NOAA, specifically from the Vidrasău (Vidrátszeg) weather station (15 km from Marosvásárhely). With this equation, the corrected soil radiance has been obtained, a radiance in which atmospheric effects have been limited.

3.2.3. Obtaining LST from radiance

Thermal infrared bands are transformed into brightness temperature values by the Planck's law inversion equation (*Riaño et al.,* 2000; *Chander et al.,* 2009):

$$B_T = \frac{K_2}{\ln\left(\frac{K_1}{L}+1\right)}, \tag{10}$$

where K_1 (in W/m^{-2}/sr^{-1}/µm^{-1}) and K_2 (in degrees K) are the calibration constants according to the Landsat thermal band configuration, and L is the spectral radiance (W/m^{-2}/sr^{-1}/µm^{-1}) calculated previously.

Therefore, the surface temperature (LST) is obtained with the following equation (*Avdan* and *Jovanovska Kaplan,* 2016):

$$S_T = LST = \frac{B_T}{1+\left(\lambda * \frac{B_T}{\rho}\right)\ln(\varepsilon)}, \tag{11}$$

where B_T is the brightness temperature, λ is the wavelength of the radiance emitted in each band. $\rho = h*c/\sigma$ = 14380 mK, σ is the Boltzmann constant (1.38*10^{-23} J/K), h is the Planck constant (6.26*10^{-34} Js), and c is the speed of light (2.998*10^{8} m/s). ε is the emissivity of the surface.

From this result 273.15 is subtracted to obtain the LST values in degrees Celsius.

3.3. Comparison of results

An average of the previous years to 2020 was calculated with the LST results of MODIS and Landsat. This result is a mean raster that was compared with the LST raster of 2020.

3.3.1. Dependent t-test for samples

To determine if the LST difference between the mean of 2000–2019 and 2020 whether or not is statistically significant, a t-test of two dependent samples has been performed. The t-test of dependent samples has been chosen because we are measuring the same territory before and after an intervention, that is, the application of anti-COVID measures. Therefore, the factors that make the difference are the time and anti-COVID measures. The t-test was carried out in 7 steps. (1) Definition of the null hypothesis and alternative hypothesis: H_0; μbefore = μafter, H_1; μbefore ≠ μafter. (2) Alpha statement: $\alpha = 0.05$. (3) Calculation of the degree of freedom: df = N-1. (4) Statement of the order of decision, based on the Student's t distribution t-test table. (5) Calculation of the statistical value of t. (6) Declaration of results. (7) Statement of conclusion. The t-statistic equation is as follows (*Brown* and *Melamed,* 2012):

$$t = \frac{\bar{X}_D}{s_D/\sqrt{n}}, \tag{12}$$

where

$$\bar{X}_D = \frac{(x_i + \cdots + x_n)}{n}, \tag{13}$$

$$s_D = \sqrt{\frac{\sum x^2 - \frac{(\Sigma x)^2}{n}}{n-1}}, \tag{14}$$

where *t* is the dependent test statistic, $\bar{x}_D$ is the mean difference, s_D is the standard deviation of the difference and *n* is the sample size.

The two samples were obtained with the help of Raster Pixels to Points QGIS tool. Then the attribute tables were moved to Excel.

Another paired samples t-test was performed using SPSS for the areas where LST decrease was identified. A mean comparison was made to find out if statistically there is a difference between the mean LST of the areas identified with LST decrease in the lockdown period of 2020 and the mean LST before 2020 (individual available LST data between 2003–2018) in the same period (March 16 -May 14).

3.4. Hotspot-coldspot analysis with Getis-Ord Gi statistic*

The hotspot-coldspot analysis with Getis-Ord Gi* statistic was performed to identify and describe the phenomenon of clustering in the study area of the high (hotspot) and low (coldspot) LST values (*Tran et al.,* 2017; *Ord* and *Getis,* 1995). A single high or low LST value cannot be considered as a cluster. To be considered as a hotspot or coldspot, a high or low value has to be surrounded by other high or low values. The result of the Getis-Ord Gi* statistic is a z-score. The z-score shows the intensity of clustering; a positive high z-score shows that high values are forming clusters (a hotspot), while a negative high z-score shows that low values are forming clusters (a coldspot). Thus, with the Getis-Ord Gi* statistic, we can better understand the dimensional and spatial changes of LST within the study area. This study has focused especially on the significant change in coldspots. The difference between the average LST of the previous years and 2020 LST shows specific areas in which the temperature has decreased in 2020 concerning to the past. Coldspots with more than 95% confidence level were taken into account. The Getis-Ord Gi* statistic is presented in detail on the ESRI website (*ESRI,* 2016). In this study, the calculation of Getis-Ord Gi* was done with the QGIS Hotspot Analysis plugin. The hotspot-coldspot analysis was carried out in 4 steps: (1) extracting pixel values to points, (2) creating a vector grid layer, (3) counting pixels in polygons with the weight field of the LST value, (4) execution of the hotspot-coldspot local Getis-Ord Gi* analysis.

Other authors have studied LST in urban areas using different urban impact indices such as UTFI (Urban Thermal Field Variance Index) or EEI (Ecological Evaluation Indices) (*Guha et al.,* 2017, 2018; *Grover* and *Singh,* 2015; *Jiménez-Muñoz et al.,* 2010).

The average LST values in urban areas were calculated using the QGIS Raster Layer Zonal Statistics tool.

4. Results and discussion

Owing to anthropogenic practices such as land-use change, urban expansion, urban population growth, LST is likely to increase in urban areas (*Singh et al.,* 2017; *Walawender et al.,* 2014; *Zhan et al.,* 2015). However, recent studies have shown that LST can be changed abruptly in urban areas despite urban expansion and population growth; it can decrease with the implementation of measures of suppression of the urban anthropogenic heat, for example the measures of anti-COVID lockdown. This indicates that there is a significant influence of anthropogenic activities on LST regulation (*Li et al.,* 2014; *Lau et al.,* 2020).

Land cover categories can also be distinguished based on their behavior to temperature changes. As they can hold water for the evaporative cooling process, forests and water bodies appear to have comparatively lower LST than urban areas. These land covers (forests and water bodies) increase the flow of latent heat and prevent the transfer of sensitive heat. Dry urban areas, by comparison, magnify responsive heat transfer and impede latent heat flow (*Shahmohamadi et al.,* 2011). Due to their ability to control heat, water bodies tend to have steady temperatures by using the convection mechanism in all segments of the water body (*Jensen,* 2014). *Shahmohamadi et al.* (2011) explain that built-up areas tend to have higher temperatures than their natural environment around them; this is attributable to land use characteristics and anthropogenic activities.

Built-up areas are consisting of impermeable surfaces and objects, which may lead to an increase in LST due to the lower amount of moisture available to evaporate, according to *Gartland* (2012) (see more: *Matthews,* 2012). Moreover, dark materials restrict incoming short-wave radiation from the Sun within the urban area, and at the same time, buildings can almost completely reduce wind speed. As a consequence, a low wind speed appears to decrease evaporative cooling (*Lee,* 1984). In addition, some authors add that during winter and by the presence of atmospheric pollutants, the impact of anthropogenic activities emitting heat may become more relevant (*Nagy et al.,* 2020; *Offerle et al.,* 2006).

We can conclude from previous studies that relatively higher temperatures in urban areas are influenced not only by the land cover but also by human activities.

4.1. Paired sample t-test result

The Dependent t-test with two dependent samples (Landsat LST 2020 and Landsat LST 2003 – 2018) showed that our H1 hypothesis is true (μbefore $\neq$ μafter), that is, the time and/or anti-COVID measures taken in 2020 have a statistically significant effect on the change in LST, $t = -432.7$, critical value = 1.96, $p < 0.05$.

4.2. Comparison of the average LST in the lockdown period (March 16 –May 14) of 2020 with the average for the years 2000–2019 in the same period

The average LST for the period March 16–May 14, 2020, which corresponds to the confinement period, has been compared with the average for the years 2000–2019 for the same period. In *Fig. 2*, which presents the MODIS data, we can see that during 2000 and 2019, high values of LST are found in urban areas. The situation in 2020 seems to follow the same trend. The difference map highlights the areas that show the positive and negative change. The urban environment, which stands out in the descent of the LST is the Tudor (Sásvári) district, a neighborhood characterized by the density of tall buildings and few vegetation. This neighborhood is the most crowded in the city with a significant impact on traffic and population density. For this reason, it has the greatest descent change (negative change) of LST.

Because Landsat has a higher spatial resolution, we can see in more detail the areas with high and low temperatures and the areas that have changed (*Fig. 3*).

Landsat results corroborate the MODIS results: the distribution of high and low values is different in 2020 than the long average of data existing between 2003–2018.

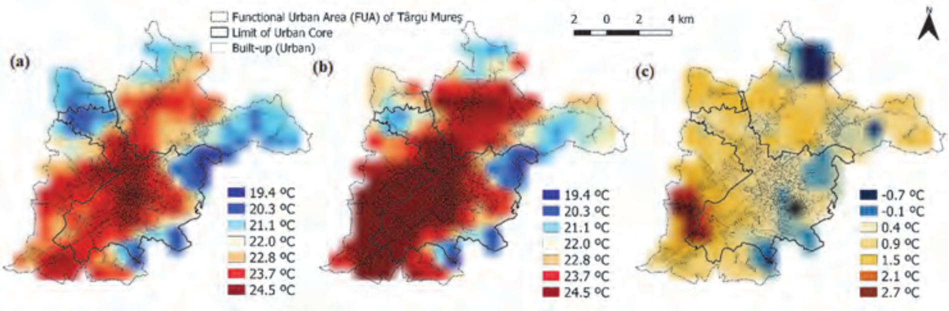

Fig. 2. MODIS LST (a) between 2000–2019, (b) in 2020, and (c) the difference between them.

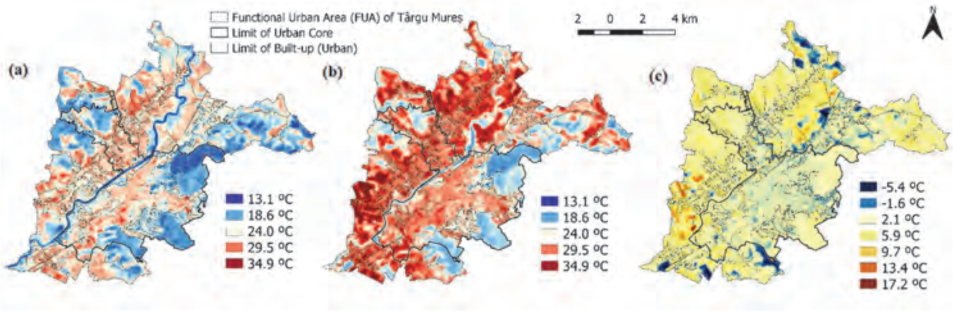

Fig. 3. Landsat LST (a) between 2003–2018, (b) in 2020, and (c) the difference between them.

Although we have higher values in 2020 in urban areas, their concentration has been reduced in some areas. However, in 2020 we can still observe existing heat islands (e.g., areas of the Azomureș industrial estate). The Tudor district also stands out in the difference raster.

Both MODIS and Landsat data show an increase in LST, in general in built-up areas. The trends in LST described below are also including the study period in 2020. The average value observed in 2000–2019 for MODIS and in 2003–2018 for Landsat images, respectively, has been subtracted from the value observed in 2020. MODIS shows an increase of +0.78 °C (average for the years 2000–2019: 23.3 °C and average of 2020: 24.1 °C), while Landsat shows an increase of +2.36 °C (average for the years 2003-2018: 24.7 °C and average of 2020: 27.0 °C).

The range of the maximum and minimum values is also different between MODIS and Landsat (MODIS: 0.79 °C, Landsat: -2.97 °C). We have a negative difference range in the case of Landsat (2003-2019 average range and 2020 range), because the range between the minimum and maximum values in the year 2020 was almost 3 °C lower (17.1 °C) than during the years 2003–2018 (20.0 °C). In the case of MODIS, this average range difference between 2000–2019 and

2020 range is not even 1 ° Celsius (the average range 2000–2019 is 4.0 °C and the 2020 range is 4.8 °C) and, on the contrary, here we have a larger range in 2020 (4.8 °C) than during 2000-2019 (4.0 °C), which gives a positive range difference. Thus, Landsat shows a much higher range than MODIS; that is, the minimum and maximum values are quite different between 2003–2018 and 2020. This is reflected in the standard deviations as well (MODIS LST 2020: σ = 1.04, MODIS LST 2000– 2019: σ = 0.92, Landsat 2020: σ = 1.71, Landsat 2003–2018: σ = 1.62). The difference in standard deviations between MODIS and Landsat shows that MODIS σ = 0.12, Landsat σ = 0.08. These differences between MODIS and Landsat are relevant to the LST trend, because they show how spatial resolution and acquisition methods of satellite images can influence the LST values obtained. Due to its higher spatial resolution, Landsat can better detect objects with higher or lower LST emissions.

Differences between MODIS and Landsat are due to the different spatial resolution of the two sensors (Landsat LST offers more details about the territory and the objects) and the different modes of capturing the TIR and obtaining the LST.

Fig. 4 shows the trend of LST between the years 2000–2020 with MODIS data in the built-up area. A downward trend can be observed between 2000–2005, however, after 2005, this becomes an upward trend of LST.

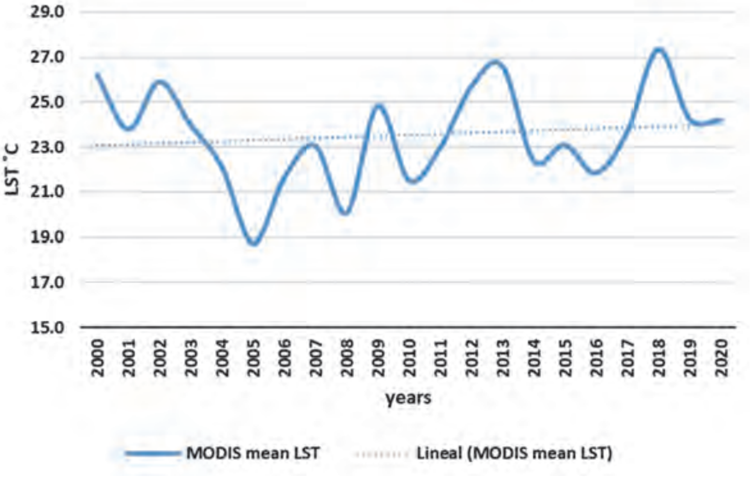

Fig. 4. MODIS mean LST evolution in the general built-up land cover (time period: March 16–May 14).

The timeseries analysis also indicates an increase of +0.72 °C in the case of MODIS data. However, if we take only the last three years (2019, 2018, 2017), we are talking about a decrease of -1 °C in urban areas. This points out that to have a broad and detailed view of how much and how LST has changed with the implementation of anti-COVID measures, it is not enough to take into consideration only the last few pairs of years, as some studies have done so far (*Maithani et al.*, 2020). At the global level, climate change also affects large and medium-sized cities, so more years should be taken when comparing with the 2020 situation. Time-series analysis shows that LST in urban areas tends to increase since 2000, although in the case of Marosvásárhely, there has been no significant urban expansion since 2000.

The increase in temperature in the urban area is due to climate change that causes even warmer cities. If we analyze the LST data of Landsat (only the data that we have), we see that we have an increase of +2.5 °C in the built areas in general. The evolution of the average LST in the built-up area with Landsat data shows two peaks throughout the images available between 2003–2020 in the month of April: in 2007 (27.3 °C) and 2018 (32.6 °C) (*Fig. 5*). An upward LST trend is also observed.

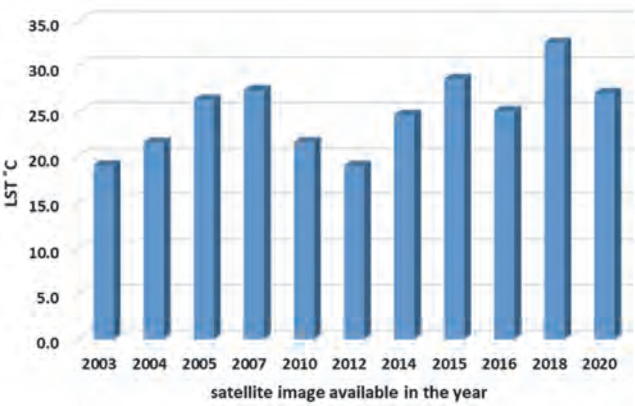

Fig. 5. Landsat mean LST evolution in the general built-up (urban) land cover over available Landsat images.

The difference between the trend detailed above first and the trend of timeseries analysis is that the former was calculated by adding the LST raster layers of the years prior to 2020 and dividing by the total number of years (20); thus comparing the resulting average raster layer of the years 2000–2019 with the raster layer of 2020 using the zonal statistics method for the urban area. The second trend analysis was also calculated with the zonal statistics method. However, this time we calculated the average value of LST for each year separately in the urban area. These observations were placed in a table, thus achieving the graphical representation of the trend (*Figs. 4* and *5*).

4.3. LST anomaly analysis

Similarly to the LST temperature calculation, the LST anomaly with MODIS data was calculated for the study period between March 16 and May 14 for the years 2000–2020. These LST anomaly results for the different years are raster layers representing the LST anomaly within March 16 – May 14 in 2000–2020. For the years 2000–2019, an average resulting in a single LST anomaly average raster has been calculated. The 2020 anomaly is not included in this average, because the mean raster of 2000–2019 is subtracted from the 2020 raster, thus obtaining the LST anomaly difference.

We calculated the monthly anomaly as the difference between the monthly climatology minus the average of months within the study period, i.e., March-May. Then the rasters between 2000–2019 are added, and a long average comparing with the 2020 raster is calculated.

Fig. 7 represents the average monthly LST anomaly in the period March 16 - May 19, 2000–2019 and in 2020. It can be observed that in 2020, the concentration of high values of positive thermal anomaly is still present in urban areas. This also shows that the spatial distribution of high and low values is different in 2020 than in previous years.

The LST anomaly trend in the built-up area reached the minimum point in 2005, when the average anomaly in the built-up was the most lower (+0.2 °C). After 2005 the variation persists, however, an upward trend is observed over time, touching the maximum value observed during 2000–2020 in 2018 (+6.4 °C) (*Fig. 6*).

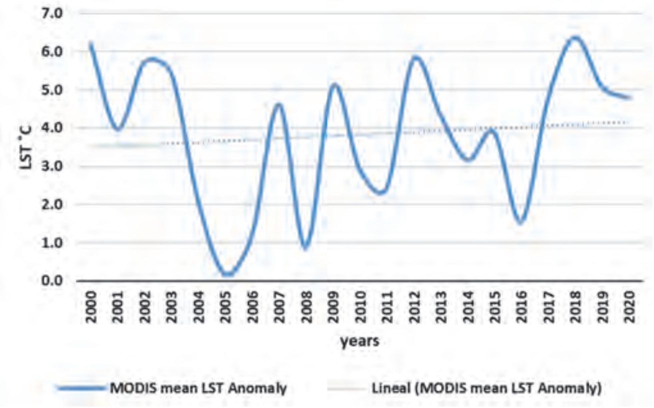

Fig. 6. MODIS mean LST anomaly in the general built-up (urban) land cover (time period: March 16–May 14).

The timeseries analysis of the anomaly shows an increase of positive LST anomaly of +1 °C by 2020 for the long average of the years 2000–2019. The anomaly trend analysis does not include the year 2020, because the average of 2000–2019 has compared with the average anomaly observed in 2020. Again, if we look only at the last three years, it shows an anomaly decrease of -0.6 °C (*Fig. 6*).

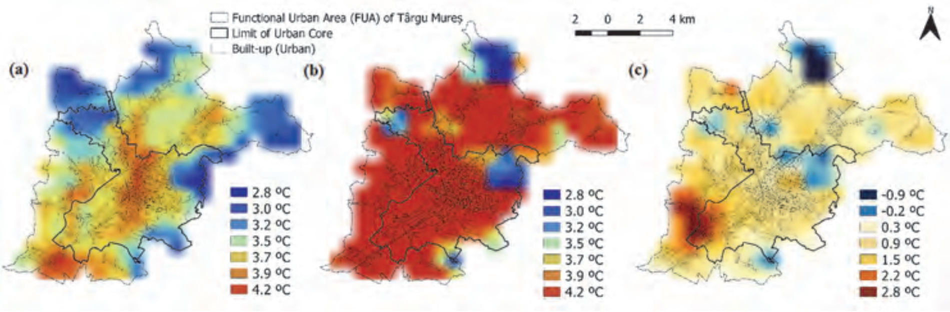

Fig. 7. LST anomaly (a) between 2000–2019, (b) in 2020, and (c) the difference between them.

4.4. . Change in the categories of built-up areas

Urban categories correspond to the land cover classification of the Urban Atlas (Copernicus Programme, Copernicus Land Monitoring Service) (*Fig. 8*). This methodology classifies urban areas into different categories according to characteristics and land use.

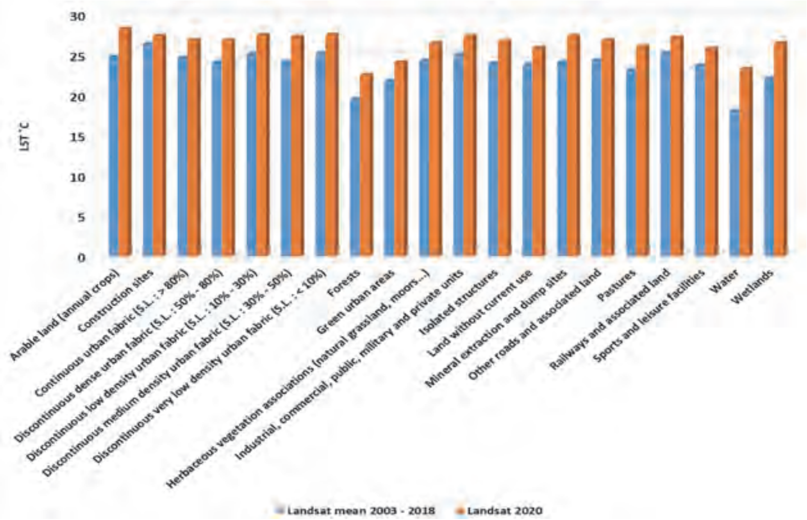

Fig. 8. Landsat LST in different land cover categories. Comparison between the mean LST of available images and 2020 (time period: March 16–May 14).

The LST analysis of urban area categories also shows an increase of LST in 2020 for all urban categories compared to the average of previous years.

The urban type that experienced the greatest increase is the "Discontinuous medium density urban fabric (S.L.: 30–50%)" (+3.1 °C). Other categories are similar in terms of the increase in temperature (about +2.4 °C).

Based on the land use data from the Urban Atlas, it is also purposeful to see what differences exist between the different land categories present in the functional urban area (FUA) of Târgu Mureș concerning the average before 2020 and the situation in 2020 (*Fig. 8*). The largest increase in LST occurs in the categories "Water" (+5.2 °C) and "Wetlands" (+4.3 °C). This change also refers to the fact that thermal anomaly persists more in water bodies. The reclassification of all these land-use types into four representative categories of the territory ("Built-up (Urban)", "Vegetation", "Water", "Bare soil") also shows that water bodies are more likely to register a positive change, an LST increase (+5.1 °C) (*Fig. 9*). On the contrary, the smallest increment in LST is recorded in the category "Bare soil" (+2.1 °C) which land type is more likely to catch and lose temperature more quickly due to the lack of vegetation. The "Built-up (Urban)" category also behaves similarly (+2.4 °C) because of the nature of the building and street materials (*Fig. 9*).

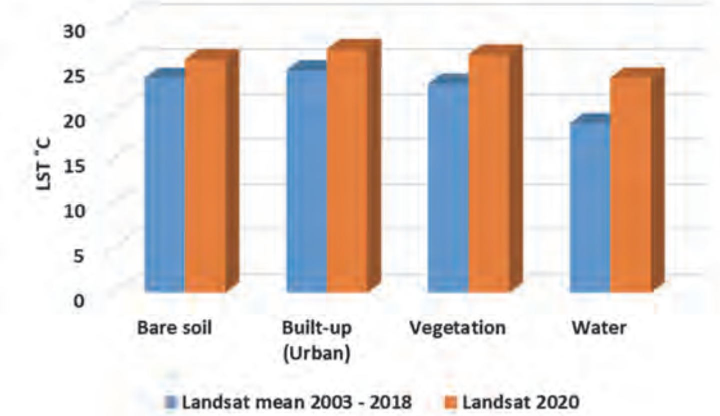

Fig. 9. Landsat LST in reclassified land cover categories. Comparison between the mean LST of available images and 2020 (time period: March 16 - May 14).

4.5. *Coldspot analysis and areas with LST drop*

Despite the general increase of LST in the built-up areas, with the hotspot-coldspot analysis of Getis-Ord Gi* is possible to identify areas with a decrease in LST in 2020 concerning the average of the previous years (*Fig. 11(a)*).

Looking at these coldspots on a Google Satellite Hybrid map, it was observed that they largely correspond to factory areas, public transport centers, shopping malls, and industrial polygons (*Fig. 11*). The Mureșeni (Meggyesfalvi)–Orașul de Jos (Bega) and Tudor (Sásvári) dictricts stand out in the number of cases. These districts are located on a west-east axis, which is the direction of the western winds. The Azomureș industrial area of national interest is located in the western part of the city. It can have an impact on the fact that these districts have significant temperature drops. On the other hand, open fields and the river Mureș show significant hotspots in terms of the difference between 2020 and the long average of the previous years.

In the case of the River Mureș, this is due to climate change. It has to be connected to the sensitivity of rivers to climate change (*Nijssen et al.*, 2001) because if a positive temperature anomaly persists in a river basin, waterbodies can store heat for longer. Other parts can also experience climate change. However, the temporal variability of the LST due to weather conditions increases, because bodies on the Earth's surface get warmer and cooler faster, and most of them are not able to store heat any longer like waterbodies.

If we focus on the map presented in *Fig. 10(b)* showing hot and cold spots in 2020, we can see that there are few clusters (hole phenomenon) within the city compared to 2013-2018 (*Fig. 10(a)*). The Azomureș chemical industrial area and other areas related to the industry also operated between March 16 –May 14, 2020, and these hotspots remained unchanged in 2020. *Fig. 11(a)* shows the difference between the LST raster of 2020 and the LST raster of 2003–2018.

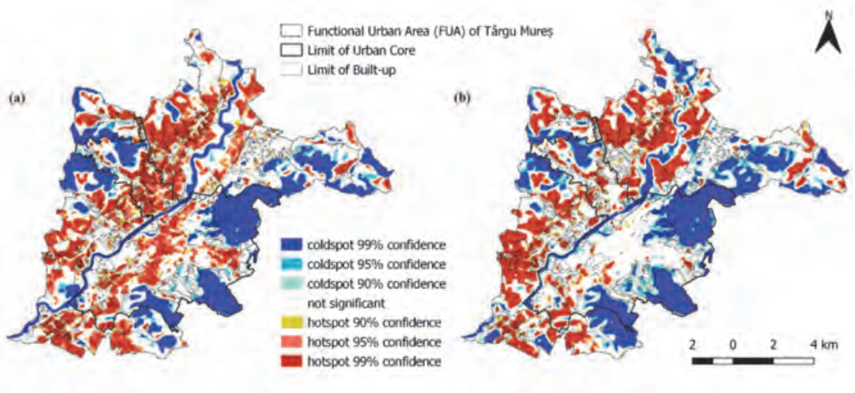

Fig. 10. Significant LST hotspots and coldspots (a) between 2003–2018 and (b) in 2020.

The total area of the built-up (urban) area is 33.84 km^2. The size of the area that has experienced a decrease in surface temperature is 0.24 km^2, which is equivalent to only 1% of the total built-up area; these are mostly areas of factories, industrial polygons, shopping centers, and public transport centers (*Table 2*). However, if we take the entire area of the significant coldspot change (confidence level of 99%) within the built-up area (*Fig. 11(b)*), this percentage is 11% (3.71 km^2) of the total built-up area. The fifth column of *Table 2* indicates the minimum LST temperature of the area of that coldspot. The average of the minimum values of these 46 cases is -0.61 °C. However, there are cases with LST loss below -1 °C. In the first column (N), the number marked with the upper index ** represents cases with LST decrease below -2 °C. The number marked with the upper index *, on the other hand, indicates cases with an LST drop below -1 °C.

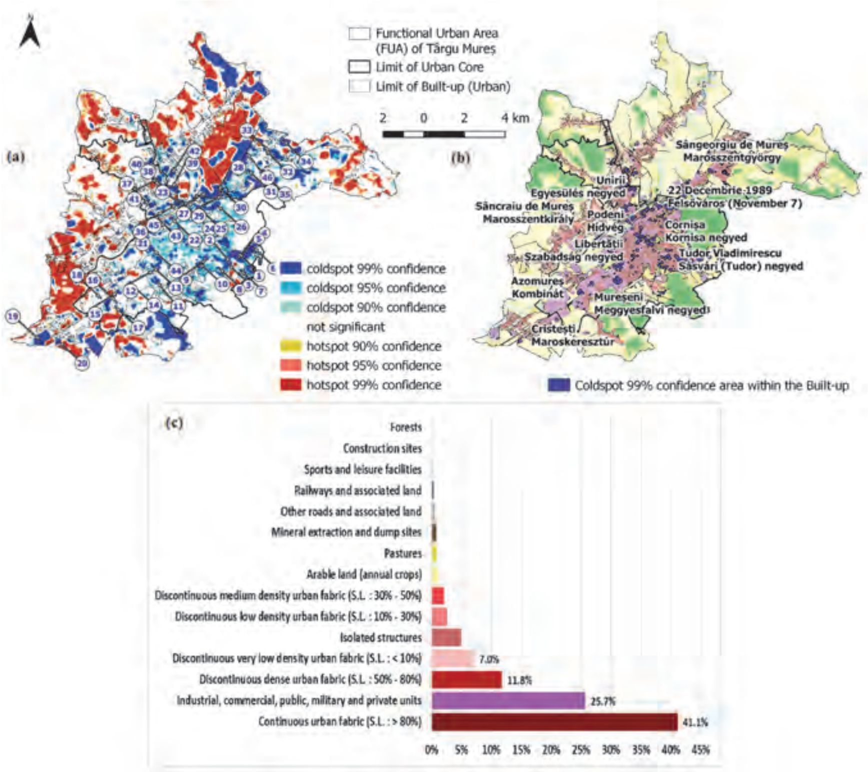

Fig. 11. (a) LST change hotspots and coldspots, (b) significant coldspots within the built-up areas (see *Table 2*), and (c) relative frequency of land cover types within the changing coldspots (confidence level of 99%) in the urban area.

The relative frequency of land cover types within significant coldspots (confidence level 99%) in the built area shows that 41.1% of the total area of cold spots corresponds to the category "Continuous urban fabric (S.L. > 80%)" (*Fig. 11(c)*). Another 25.7% of the coldspot areas corresponds to the category "Industrial, commercial, public, military and private units" and, also, 11.8% belong to the "Discontinuous dense urban fabric (S.L. 50%–80%)" category.

Table 2. Decreased areas in LST; category type, name of location, and the minimum LST value of decrease. The number marked in the first column (N) with the upper index * indicates cases with LST decrease below -1 °C, while ** indicates the cases with an LST drop below -2 °C (Fig. 11)

N	Type	District	Constituent building name	Min LST decrease (°C)
1**	Industrial, Commercial	Tudor (Sásvári)	SC Sumel Maşini de Calcul SA; ROTECOM S.R.L.; Meesenburg România - sediul central; Coralia Com Srl Depozit Tg. Mures; SELDOR S.R.L; Sameday Curier Târgu Mureș	**-2.58**
2	Commercial, Industrial, Service	Tudor (Sásvári)	U-Rent - Închirieri Remorci; X-Tend MOB; ITP Nova Service; SC PARTNER ALU PLAST SRL; Gold Gym Fitness & Aerobics	-0.69
3	Services	Tudor (Sásvári)	ELIT; Merkúr	-0.00021
4	Residential	Tudor (Sásvári)	Houses	-0.22
5	Commercial	Tudor (Sásvári)	Ropharma	-0.26
6	Residential	Tudor (Sásvári)	Mansions	-0.37
7	Services, Commercial	Tudor (Sásvári)	Auchan	-0.44
8	Industrial, Services	Tudor (Sásvári)	Euro Gas Systems: Vessels & CNC; CarXpert Mures | Service Auto & Tractări	-0.34
9	Services, Commercial	Tudor (Sásvári)	Area of Profi Moldovei	-0.03
10	Transportation Services	Tudor (Sásvári)	MOL gas station; Crossroad Bulevardul Pandurilor - Strada Secerei	-0.10
11*	Industrial, Transportation	Orașul de Jos (Bega)	Industrial area of Orașul de Jos quarter: TMF Manufacturing Solutions SRL; Roseco SRL; Novoparts SRL; PLASTERM S.A.; Siletina SC Transport Local SA; Autogara Voiajor Marosvásárhely; Surtec; Bioeel; FrieslandCampina	**-1.33**
12	Residential	Orașul de Jos (Bega)	Strada Făgărașului	-0.0001
13	Commercial, Transportation	Orașul de Jos (Bega)	Near the CFR locomotive depot	-0.10
14	Commercial	Mureșeni (Meggyesfalvi)	Commercial Area: Natürlich - mobilier und decoratiuni, Tg.Mures; Melinda Instal; SC Vargas Seminee SRL; Total Sport Distribution SRL; Kober SRL - Mureș	-0.82
15	Industrial, Commercial	Mureșeni (Meggyesfalvi)	Industrial Area: Mobex polygon area; Panservice; Urgent Cargus	-0.90
16	Services	Mureșeni (Meggyesfalvi)	Recreation Area: Hotel Imperial Inn; Imperial Spa. Service Area: Turbo Logic; TEKAROM SRL; Professional Recycle	-0.98
17	Commercial, Services	Mureșeni (Meggyesfalvi)	Metro	-0.25
18	Industrial	Mureșeni (Meggyesfalvi) - Azomureș	Azomureș	-0.45
19*	Services: Water treatment plant	Cristești (Maroskeresztúr)	Aquaserv	**-1.84**
20	Services, Commercial	Cristești (Maroskeresztúr)	Leco AGRO; SC VERAL COM SRL	-0.16
21	Services	Centru (Főtér)	Multipurpose Hall (Sala Polivalentă)	-0.05
22*	Industrial	Centru (Főtér)	Electromureş S.A.	**-1.75**

Table 2. Continued

N	Type	District	Constituent building name	Min LST decrease (°C)
23	Services	Aleea Carpați (Kárpátok-sétány)	Area near Pensiunea Mureșul	-0.32
24	Residential	Aleea Carpați (Kárpátok-sétány)	"Area of the apartment"	-0.02
25	Industrial	22 Decembrie (Felsőváros)	Furniture Mobex factory area	-0.72
26	Services	22 Decembrie (Felsőváros)	Area of Emergency County Hospital Marosvásárhely	-0.55
27*	Residential	Sângeorgiu de Mureș	New houses - Strada Petőfi Sándor utca	**-1.17**
28	Residential	Sângeorgiu de Mureș	Houses - Strada Mihai Eminescu utca	-0.14
29	Commercial	22 Decembrie (Felsőváros)	Nakita Prod Comimpex S.R.L.; Accesorii Ancorare Marfă	-0.08
30	Industrial	Sângeorgiu de Mureș (Marosszentgyörgy)	Manufacture complex - Strada Sudului	-0.80
31	Industrial, Commercial	Sângeorgiu de Mureș (Marosszentgyörgy)	Buildings	-0.15
32*	Industrial, Services	Sângeorgiu de Mureș (Marosszentgyörgy)	SC Gastrometal SRL; AD GARAGE GOLDFIT SERVICE; A.C.R Sângeorgiu de Mureș	**-1.27**
33	Services	Sângeorgiu de Mureș (Marosszentgyörgy)	TinyHome - Închirieri autorulote	-0.30
34	Residential	Sângeorgiu de Mureș (Marosszentgyörgy)	Houses	-0.17
35	Residential	Sângeorgiu de Mureș (Marosszentgyörgy)	Houses	-0.63
36	Transportation, Industrial	Podeni (Hídvég)	Hídvég Crossroad; Romcab S.A.	-0.20
37	Residential	Podeni (Hídvég)	Houses	-0.31
38*	Industrial	Unirii (Egyesülés)	Strada Apaductului	**-1.05**
39**	Industrial	Unirii (Egyesülés)	Foto	**-2.80**
40	Residential	Unirii (Egyesülés)	Houses	-0.09
41	Residential	Unirii (Egyesülés)	Unirii Park Residence	-0.17
42*	Industrial	Unirii (Egyesülés)	AUNDE C&S AUTOMOTIVE S.R.L.	**-1.16**
43	Transportation	Sâncraiu de Mureș (Marosszentkirály)	Road	-0.10
44	Commercial	Libertății (Szabadság)	S.C. ADIMAG COMIMPEX S.R.L.	-0.08
45	Commercial	Unirii (Egyesülés)	Palas com	-0.25
46*	Residential	Sângeorgiu de Mureș (Marosszentgyörgy)	Houses	**-1.78**

4.6. Paired sample t-test for areas identified with LST decrease

To be able to affirm that the decrease of the LST in these 46 cases can be explained with the application of the anti-COVID measures, it is examined statistically whether there is a difference between the mean LST of the areas identified with LST decrease in the lockdown period of 2020 and the mean LST before 2020 (i.e., 2003–2018) in the same period (March 16 –May 14) (*Table 3*). For this purpose, we use the available Landsat data.

The null hypothesis (H_0) is that the mean of the *before LST* is equal to the mean of the *after LST* measurement (μbefore = μafter). In other words, there is no difference between LST measured before 2020 with no anti-COVID measures applied, and LST measured in 2020 with anti-COVID measures applied.

The alternative hypothesis (H_1) is that the mean of the *before LST* is not equal to the mean of the *after LST* measurement (μbefore ≠ μafter). In other words, there is a difference between LST before 2020 with no anti-COVID measures applied, and LST in 2020 with anti-COVID measures applied.

We test this with an alpha value equal to 0.05, which is equal to 95% confidence level.

In the 46 cases, the mean LST of 2020 was compared with the mean LST of previous years. The comparative results of the averages show that in all pairs, the t statistical value is less or greater than the critical value (2.000), which corresponds to the degree of freedom (45). Likewise, the p-value in all pairs is less than 0.05 (*Table 3*). Therefore, we can conclude that there is a statistically significant difference in the average LST before and after anti-COVID measures in the areas identified with LST decrease.

Table 3. Paired samples t-test comparing the average difference of Landsat 2020 mean LST and previous years mean LST in the areas identified with LST decrease. Column t shows the t-test values, df is the degree of freedom, and Sig. (2-tailed) shows the significance of p value for each pair (this test is done with an $\alpha = 0.05$)

Paired samples t-test									
		Paired differences							
					95% confidence interval of the difference				
Landsat mean LST		Mean	Std. deviation	Std. error mean	Lower	Upper	t	df	Sig. (2-tailed)
Pair 1	2020 - 2018	-8.38965	2.35986	0.34794	-9.09045	-7.68886	-24.112	45	0.000
Pair 2	2020 - 2016	-1.13292	2.37514	0.35019	-1.83824	-0.42759	-3.235	45	0.002
Pair 3	2020 - 2015	-3.24816	1.99564	0.29424	-3.84079	-2.65553	-11.039	45	0.000
Pair 4	2020 - 2014	1.30848	1.21359	0.17893	0.94809	1.66887	7.313	45	0.000
Pair 5	2020 - 2012	4.56721	1.64654	0.24277	4.07825	5.05617	18.813	45	0.000
Pair 6	2020 - 2010	3.53593	1.29481	0.19091	3.15142	3.92045	18.521	45	0.000
Pair 7	2020 - 2007	-3.93599	1.28956	0.19013	-4.31894	-3.55304	-20.701	45	0.000
Pair 8	2020 - 2005	-2.46037	1.94611	0.28694	-3.03830	-1.88245	-8.575	45	0.000
Pair 9	2020 - 2004	1.81966	1.83836	0.27105	1.27374	2.36559	6.713	45	0.000
Pair 10	2020 - 2003	4.68105	1.87976	0.27716	4.12283	5.23927	16.890	45	0.000
Pair 11	2020 - Mean years 2003-2018	-0.32548	0.30425	0.04486	-0.41583	-0.23512	-7.255	45	0.000

5. Conclusions

In Marosvásárhely city, the land surface temperature (LST), despite the anti-COVID measures applied between March 16 -May 14 corresponding to the lockdown period, was increased by 1–2 °C in general in urban areas compared to the previous years of 2000-2019. It can be explained by the insufficiency and weakness of the anti-COVID measures adopted. Anti-COVID measures could not reverse the process of increasing LST and positive LST anomaly throughout urban areas.

However, anti-COVID measures have not been completely ineffective. 46 cases of coldspots within urban areas show a decline in LST due to the 2020 health emergency. The vast majority of these coldspots are areas that perform economic and transport activity, so, logically, the anti-COVID measures have mainly affected these areas.

Coldspots are interpreted as a negative LST change and not as a downward trend. The 46 cases of coldspots are resulted from the difference between the 2020 raster and the average raster of 2003–2018. (These Landsat data do not include every year between 2000–2019, because no useful satellite image had found in these years just after applying the anti-COVID measures in the study period). This difference raster shows areas where compared to previous years, LST has decreased or increased in 2020. This raster layerwas used to identify statistically significant coldspots.

Consequently, according to the difference between the 2003–2018 average and 2020, the 46 identified cases within the urban land class are specific areas that have transformed into coldspots.

The percentage of the total size of the area that has shown a negative change, that is, it has become colder in the lockdown period of 2020 than during the same period of the previous years, is about 1% (0.25 km^2) of the total built-up area (33.8 km^2). However, if we take the significant coldspots of change (confidence level of 99%) within the built-up area as a measure, this percentage goes up to 11% (3.71 km^2). The most frequent built-up area type within the significant coldspots (confidence level of 99%) is the "Continuous urban fabric (S.L. > 80%)" (41.1%), followed by the categories "Industrial, commercial, public, military and private units" (25.7%), and "Discontinuous dense urban fabric (S.L. 50%–80%)" (11.8%), which are typically urban categories.

Paired samples t-test performed for the areas identified with LST decrease shows that there is a statistically significant difference ($p < 0.05$) of the average LST between the years before 2020 and 2020, which may indicate evidence of the implication of anti-COVID measures to the decline of LST in these areas carrying out economic and transport activities. This shows that in a medium-sized city such as Marosvásárhely, anti-COVID measures have caused a decrease in land surface temperature in specific areas (*Fig. 11, Tables 2* and *3*).

The MODIS LST data are satisfactory for identifying general trends and patterns at global or moderate geographical scale. However, for a hotspot-coldspot analysis of the urban heat islands, it is more appropriate to use Landsat satellite data.

Limitations of the study: To show irrefutably that the anti-COVID measures had a significant effect on the decline of LST, more or all medium-sized cities would have to be analyzed at a country level or the European continental level. The nature and effectiveness of the measures should be taken also into account in each country or region. Therefore, other studies should compare more cities in the same administration region or the same country.

Acknowledgment: The authors wish to express appreciation to the free software developers of QGIS and Google Earth Engine.

References

Agrawal, S., Bhandari, S., Bhattacharjee, A., Deo, A., Dixit, N. M., Harsha, P., . . ., and *Yasodharan, S.*, 2020: City-Scale Agent-Based Simulators for the Study of Non-pharmaceutical Interventions in the Context of the COVID-19 Epidemic: IISc-TIFR COVID-19 City-Scale Simulation Team. *J. Indian Inst. Sci. 100*(4), 809–847. https://doi.org/10.1007/s41745-020-00211-3

Avdan, U. and *Jovanovska Kaplan, G.*, 2016: Algorithm for Automated Mapping of Land Surface Temperature Using LANDSAT 8 Satellite Data. *J. Sensors, 2016*(2), 1–8. https://doi.org/10.1155/2016/1480307

Awasthi, A., Sharma, A., Kaur, P., Gugamsetty, B., and *Kumar, A.,* 2021: Statistical interpretation of environmental influencing parameters on COVID-19 during the lockdown in Delhi, India. *Environment, Development and Sustainability 23,* 8147–8160. https://doi.org/10.1007/s10668-020-01000-9

Barsi, J. A., Barker, J. L., and *Schott, J. R.*, 2003: An Atmospheric Correction Parameter Calculator for a single thermal band earth-sensing instrument. *IEEE International Geoscience and Remote Sensing Symposium 2003*, *5*, 3014–3016. Toulouse. https://doi.org/10.1109/IGARSS.2003.1294665

Barsi, J. A., Hook, S. J., Palluconi, F. D., Schott, J. R., and *Raqueno, N. G.*, 2006: Landsat TM and ETM+ thermal band calibration. En J. J. Butler (Ed.), *Earth Observ. Syst.XI*, *6296.* San Diego. doi:10.1117/12.683212. https://doi.org/10.1117/12.683212

Brown, S. and *Melamed, L.*, 2012: T Test, In: Experimental Design and Analysis. SAGE Publications, Inc., 10–12. https://doi.org/10.4135/9781412984218.n3

Buyantuyev, A. and *Wu, J.*, 2010: Urban heat islands and landscape heterogeneity: linking spatiotemporal variations in surface temperatures to land-cover and socioeconomic patterns. *Landscape Ecol 25*, 17–33. https://doi.org/10.1007/s10980-009-9402-4

Ceccato, P., Pietsch, V., Chen, Y.-J., Marconi, B., Balk, C., and *Stevenson, A.*, 2017: JavaScript: Using Google Earth Engine to Analyze Land Surface Temperature by benjamin.j.marconi - issuu. International Research Institute for Climate Society, Earth Institute, Columbia University,. URL https://issuu.com/benjamin.j.marconi/docs/iri_analysis_of_temperature_data.docx (accessed 12.29.20).

Chander, G., Markham, B. L., and *Helder, D. L.*, 2009: Summary of current radiometric calibration coefficients for Landsat MSS, TM, ETM+, and EO-1 ALI sensors. *Remote Sens. Environ. 113*, 893–903. https://doi.org/10.1016/j.rse.2009.01.007

Coll, C., Galve, J. M., Sanchez, J. M., and *Caselles, V.*, 2010: Validation of Landsat-7/ETM+ Thermal-Band Calibration and Atmospheric Correction With Ground-Based Measurements. *IEEE Trans. Geosci. Remote Sens., 48*, 547–555. https://doi.org/10.1109/TGRS.2009.2024934

Dissanayake, D., Morimoto, T., Murayama, Y., and *Ranagalage, M.*, 2019a: Impact of Landscape Structure on the Variation of Land Surface Temperature in Sub-Saharan Region: A Case Study of Addis Ababa using Landsat Data (1986–2016). *Sustainability 11*, 2257. https://doi.org/10.3390/su11082257

Dissanayake, D., Morimoto, T., Murayama, Y., Ranagalage, M., and *Handayani, H. H.*, 2019b: Impact of Urban Surface Characteristics and Socio-Economic Variables on the Spatial Variation of Land Surface Temperature in Lagos City, Nigeria. *Sustainability, 11*(1), 25. https://doi.org/10.3390/su11010025

Donegan, S. J., and *Flynn, L. P.*, 2004: Comparison of the response of the Landsat 7 Enhanced Thematic Mapper Plus and the Earth Observing-1 Advanced Land Imager over active lava flows. *J. Volcanol. Geothermal Res. 135*(1-2), 105–126. https://doi.org/10.1016/j.jvolgeores.2003.12.010

Dousset, B., Luvall, J.C., and *Hulley, G.C.*, 2019: Surface Temperatures in the Urban Environment, In: Taking the Temperature of the Earth (eds. *Hulley, G. C.* and *Ghent, D.*). Elsevier, 203–226. https://doi.org/10.1016/B978-0-12-814458-9.00007-1

Du, C., Ren, H., Qin, Q., Meng, J., and *Zhao, S.*, 2015: A Practical Split-Window Algorithm for Estimating Land Surface Temperature from Landsat 8 Data. *Remote Sens. 7*(1), 647–665. https://doi.org/10.3390/rs70100647

Duan, S.-B., Li, Z.-L., Li, H., Göttsche, F.-M., Wu, H., Zhao, W., . . ., and *Coll, C.*, 2019: Validation of Collection 6 MODIS land surface temperature product using in situ measurements. *Remote Sens. Environ. 225*, 16–29. https://doi.org/10.1016/j.rse.2019.02.020

Eleftheriou, D., Kiachidis, K., Kalmintzis, G., Kalea, A., Bantasis, C., Koumadoraki, P., . . ., and *Gemitzi, A.*, 2018: Determination of annual and seasonal daytime and nighttime trends of MODIS LST over Greece - climate change implications. *Sci. Total Environ. 616–617*, 937–947. https://doi.org/10.1016/j.scitotenv.2017.10.226

ESRI, 2016: How Hot Spot Analysis (Getis-Ord Gi*) works. Retrieved 12 16, 2020, from https://desktop.arcgis.com/en/arcmap/10.3/tools/spatial-statistics-toolbox/h-how-hot-spot-analysis-getis-ord-gi-spatial-stati.htm

Gallo, K. P., McNab, A. L., Karl, T. R., Brown, J. F., Hood, J. J., and *Tarpley, J. D.*, 1993: The Use of NOAA AVHRR Data for Assessment of the Urban Heat Island Effect. *J. Appl. Meteorol. Climatol. 32*(5), 899–908. https://doi.org/10.1175/1520-0450(1993)032<0899:TUONAD>2.0.CO;2

Gartland, L., 2012: Heat Islands: Understanding and mitigating heat in urban areas (1 ed.). London, UK: Routledge. https://doi.org/10.4324/9781849771559

Grover, A. and *Singh, R.B.*, 2015: Analysis of Urban Heat Island (UHI) in Relation to Normalized Difference Vegetation Index (NDVI): A Comparative Study of Delhi and Mumbai. *Environments 2*, 125–138. https://doi.org/10.3390/environments2020125

Guha, S., Govil, H., and *Mukherjee, S.*, 2017: Dynamic analysis and ecological evaluation of urban heat islands in Raipur city, India. *J. Appl. Remote Sens. 11*(3), 036020. https://doi.org/10.1117/1.JRS.11.036020

Guha, S., Govil, H., Dey, A., and *Gill, N.*, 2018: Analytical study of land surface temperature with NDVI and NDBI using Landsat 8 OLI and TIRS data in Florence and Naples city, Italy. *Eur. J. Remote Sens. 51*(1), 667–678. https://doi.org/10.1080/22797254.2018.1474494

Hadibasyir, H. Z., Rijal, S. S., and *Sari, D. R.*, 2020: Comparison of Land Surface Temperature During and Before the Emergence of Covid-19 using Modis Imagery in Wuhan City, China. *Forum Geografi 34*(1), 1–15. https://doi.org/10.23917/forgeo.v34i1.10862

Hulley, G. C., Ghent, D., Göttsche, F. M., Guillevic, P. C., Mildrexler, D. J., and *Coll, C.*, 2019: Land Surface Temperature, In: Taking the Temperature of the Earth (eds. *Hulley, G.C., and Ghent, D.*). Elsevier, 57–127. https://doi.org/10.1016/B978-0-12-814458-9.00003-4

Hulley, G. C., Hughes, C. G., and *Hook, S. J.*, 2012: Quantifying uncertainties in land surface temperature and emissivity retrievals from ASTER and MODIS thermal infrared data. *J. Geophys. Res.: Atmospheres, 117*(D23), 1–18. https://doi.org/10.1029/2012JD018506

Imhoff, M. L., Zhang, P., Wolfe, R. E., and *Bounoua, L.*, 2010: Remote sensing of the urban heat island effect across biomes in the continental USA. *Remote Sens. Environ. 114*(3), 504–513. https://doi.org/10.1016/j.rse.2009.10.008

Institutul Național de Statistică, 2011: Rezultate | Recensamant 2011. *Recensământul populației și al locuințelor*,. URL http://www.recensamantromania.ro/rezultate-2/ (accessed 12.30.20). (In Romaian)

Jensen, J. R., 2014: Remote Sensing of the Environment: An Earth Resource Perspective (2 ed.). Harlow, Essex, England: Pearson.

Jensen, J., 2015: Introductory Digital Image Processing: A Remote Sensing Perspective (4 ed.). Upper Saddle River, NJ, US: Prentice Hall Press.

Jiménez-Muñoz, J. C., Sobrino, J. A., Cristóbal, J., Sòria, G., Ninyerola, M., Pons, X., . . ., and *Mattar, C.*, 2010: Land surface temperature retrieval from historical LANDSAT data. *Revista de Teledetección, 33*, 53–63.

Jiménez-Muñoz, J., Sobrino, J., Skokovic, D., Mattar, C., and *Cristóbal, J.*, 2014: Land Surface Temperature Retrieval Methods From Landsat-8 Thermal Infrared Sensor Data. *IEEE Geosci. and Remote Sens. Lett. 11*(10), 1840–1843. https://doi.org/10.1109/LGRS.2014.2312032

Karnieli, A., Ben-Dor, E., Bayarjargal, Y., and *Lugasi, R.*, 2004: Radiometric saturation of Landsat-7 ETM+ data over the Negev Desert (Israel): problems and solutions. *Int. J. Appl. Earth Observ. Geoinform. 5*(3), 219–237. https://doi.org/10.1016/j.jag.2004.04.001

Kikon, N., Singh, P., Singh, S. K., and *Vyas, A.*, 2016: Assessment of urban heat islands (UHI) of Noida City, India using multi-temporal satellite data. *Sustain. Cities Society 22*, 19–28. https://doi.org/10.1016/j.scs.2016.01.005

Kis, A., Pongrácz, R., Bartholy, J., Gocic, M., Milanovic, M., and *Trajkovic, S.*, 2020: Multi-scenario and multi-model ensemble of regional climate change projections for the plain areas of the pannonian basin. *Időjárás 124*, 157–190. https://doi.org/10.28974/idojaras.2020.2.2

Kovács, K.D., 2019: Evaluation of burned areas with SENTINEL-2 using SNAP. The case of Kineta and Mati, Greece, July 2018. *Geographia Technica, 14*(2), 20–38. https://doi.org/10.21163/GT_2019.142.03

Lau, H., Khosrawipour, V., Kocbach, P., Mikolajczyk, A., Schubert, J., Bania, J., and *Khosrawipour, T.*, 2020: The positive impact of lockdown in Wuhan on containing the COVID-19 outbreak in China. *J. Travel Medicine, 27*(3), 1–7. https://doi.org/10.1093/jtm/taaa037

Lee, D.O., 1984: Urban climates. *Progr. Phys. Geography: Earth Environ 8*(1), 1–31. https://doi.org/10.1177/030913338400800101

Li, L., Tan, Y., Ying, S., Yu, Z., Li, Z., and *Lan, H.*, 2014: Impact of land cover and population density on land surface temperature: case study in Wuhan, China. *J. Appl. Remote Sens. 8*(1), 084993. https://doi.org/10.1117/1.JRS.8.084993

Li, X., Li, W., Middel, A., Harlan, S., Brazel, A. J., and *Turner, B.*, 2016: Remote sensing of the surface urban heat island and land architecture in Phoenix, Arizona: Combined effects of land composition and configuration and cadastral-demographic-economic factors. *Remote Sens. Environ. 174*, 233–243. https://doi.org/10.1016/j.rse.2015.12.022

Lin, C., Lau, A.K., Fung, J.C., Guo, C., Chan, J.W., Yeung, D.W., . . ., and *Lao, X.Q.*, 2020: A mechanism-based parameterisation scheme to investigate the association between transmission rate of COVID-19 and meteorological factors on plains in China. *Sci. Total Environ. 737*(140348). https://doi.org/10.1016/j.scitotenv.2020.140348

Liu, J., Zhou, J., Yao, J., Zhan, X., Li, L., Xu, X., . . ., and *Zhang, K.*, 2020: Impact of meteorological factors on the COVID-19 transmission: A multi-city study in China. *Sci. Total Environ. 726*(138513). https://doi.org/10.1016/j.scitotenv.2020.138513

Ma, Y., Zhao, Y., Liu, J., He, X., Wang, B., Fu, S., . . ., and *Luo, B.*, 2020: Effects of temperature variation and humidity on the death of COVID-19 in Wuhan, China. *Sci. Total Environ. 724*(138226). https://doi.org/10.1016/j.scitotenv.2020.138226

Maithani, S., Nautiyal, G., and *Sharma, A.*, 2020: Investigating the Effect of Lockdown During COVID-19 on Land Surface Temperature: Study of Dehradun City, India. *J. Indian Soc. Remote Sens. 48*(9), 1297–1311. https://doi.org/10.1007/s12524-020-01157-w

Mallick, J., Rahman, A., and *Singh, C. K.*, 2013: Modeling urban heat islands in heterogeneous land surface and its correlation with impervious surface area by using night-time ASTER satellite data in highly urbanizing city, Delhi-India. *Adv. Space Res. 52*(4), 639–655. https://doi.org/10.1016/j.asr.2013.04.025

Mallick, J., Singh, C. K., Shashtri, S., Rahman, A., and *Mukherjee, S.*, 2012: Land surface emissivity retrieval based on moisture index from LANDSAT TM satellite data over heterogeneous surfaces of Delhi city. *Int. J. Appli. Earth Observ. Geoinform. 19*, 348–358. https://doi.org/10.1016/j.jag.2012.06.002

Mathew, A., Khandelwal, S., and *Kaul, N.*, 2016: Spatial and temporal variations of urban heat island effect and the effect of percentage impervious surface area and elevation on land surface temperature: Study of Chandigarh city, India. *Sustain. Cities Soc. 26*, 264–277. https://doi.org/10.1016/j.scs.2016.06.018

Mathew, A., Khandelwal, S., and *Kaul, N.*, 2017: Investigating spatial and seasonal variations of urban heat island effect over Jaipur city and its relationship with vegetation, urbanization and elevation parameters. *Sustain. Cities Soc. 35*, 157–177. https://doi.org/10.1016/j.scs.2017.07.013

Matthews, T., 2012: Heat islands: understanding and mitigating heat in urban areas. *Australian Planner 49*(4), 363–364. https://doi.org/10.1080/07293682.2011.591742

Meng, C., and *Dou, Y.*, 2016: Quantifying the Anthropogenic Footprint in Eastern China. *Sci. Reports 6*(24337), 1–7. https://doi.org/10.1038/srep24337

Mohamadi, B., Chen, S., Balz, T., Gulshad, K., and *McClure, S. C.*, 2019: Normalized Method for Land Surface Temperature Monitoring on Coastal Reclaimed Areas. *Sensors 19*(22), 4836. https://doi.org/10.3390/s19224836

Mukherjee, S., Joshi, P. K., and *Garg, R. D.*, 2017: Analysis of urban built-up areas and surface urban heat island using downscaled MODIS derived land surface temperature data. *Geocarto Int. 32*(8), 900-918. https://doi.org/10.1080/10106049.2016.1222634

Nagy, G., Kovács, R., Szőke, S., Bökfi, K.A., Gurgenidze, T., and Sahbeni, G., 2020: Characteristics of pollutants and their correlation to meteorological conditions in Hungary applying regression analysis. *Időjárás 124*, 113–127. https://doi.org/10.28974/idojaras.2020.1.6

Ndossi, M.I., and *Avdan, U.*, 2016: Application of Open Source Coding Technologies in the Production of Land Surface Temperature (LST) Maps from Landsat: A PyQGIS Plugin. *Remote Sens. 8*(5), 1–31. https://doi.org/10.3390/rs8050413

Nijssen, B., O'donnell, G.M., Hamlet, A.F., and Lettenmaier, D.P., 2001: Hydrologic sensitivity of global rivers to climate change. *Climatic Change 50*, 143–175. https://doi.org/10.1023/A:1010616428763

Offerle, B., Grimmond, C. S., Fortuniak, K., Kłysik, K., and *Oke, T. R.*, 2006: Temporal variations in heat fluxes over a central European city centre. *Theor. Appl. Climatol. 84*(1), 103–115. https://doi.org/10.1007/s00704-005-0148-x

Oke, T. R., 1982: The energetic basis of the urban heat island. *Quart. J. Roy. Meteorol. Soc. 108*(455), 1–24. https://doi.org/10.1002/qj.49710845502

Ord, J. K., and *Getis, A.*, 1995: Local Spatial Autocorrelation Statistics: Distributional Issues and an Application. *Geograph. Anal. 27*(4), 286–306. https://doi.org/10.1111/j.1538-4632.1995.tb00912.x

Patel, H., Talbot, N., Salmond, J., Dirks, K., Xie, S., and *Davy, P.*, 2020: Implications for air quality management of changes in air quality during lockdown in Auckland (New Zealand) in response to the 2020 SARS-CoV-2 epidemic. *Sci. Total Environ. 746*(141129). https://doi.org/10.1016/j.scitotenv.2020.141129

Quattrochi, D. A., and *Luvall, J. C.*, 2004: Thermal Remote Sensing in Land Surface Processes. Boca Raton, Florida, US: CRC Press. https://doi.org/10.1201/9780203502174

Ranagalage, M., Dissanayake, D., Murayama, Y., Zhang, X., Estoque, R., Perera, E., and *Morimoto, T.*, 2018: Quantifying Surface Urban Heat Island Formation in the World Heritage Tropical Mountain City of Sri Lanka. *ISPRS Int. J. Geo-Inf.*, *7*(9), 341. https://doi.org/10.3390/ijgi7090341

Riaño, D., Salas, J., and *Chuvieco, E.*, 2000: Corrección Atmosférica y Topográfica, Información Multi-temporal y Auxiliar Aplicadas a la Cartografía de Modelos de Combustibles con Imágenes Landsat-TM, In: Tecnologías geográficas para el desarrollo sostenible (eds. Aguado, I., and Gómez, M.). Madrid, Comunidad de Madrid, España: Universidad de Alcalá: Asociación Española de Geografía, 222–239. (In Spain)

Rozenstein, O., Qin, Z., Derimian, Y., and *Karnieli, A.*, 2014: Derivation of Land Surface Temperature for Landsat-8 TIRS Using a Split Window Algorithm. *Sensors 14*(4), 5768–5780. https://doi.org/10.3390/s140405768

Sahana, M., Ahmed, R., and *Sajjad, H.*, 2016: Analyzing land surface temperature distribution in response to land use/land cover change using split window algorithm and spectral radiance model in Sundarban Biosphere Reserve, India. *Modeli. Earth Syst. Environ. 2*(81), 1–11. https://doi.org/10.1007/s40808-016-0135-5

Sattari, F., and *Hashim, M.*, 2014: A Breife Review of Land Surface Temperature Retrieval Methods from Thermal Satellite Sensors. *Middle East J. Sci. Res. 22*(5), 757–768. https://doi.org/10.5829/idosi.mejsr.2014.22.05.21934

Sekertekin, A., and *Bonafoni, S.*, 2020: Land Surface Temperature Retrieval from Landsat 5, 7, and 8 over Rural Areas: Assessment of Different Retrieval Algorithms and Emissivity Models and Toolbox Implementation. *Remote Sensing 12*(2), 294. https://doi.org/10.3390/rs12020294

Sellers, P. J., 1985: Canopy reflectance, photosynthesis and transpiration. *Int. J.Remote Sens. 6*(8), 1335–1372. https://doi.org/10.1080/01431168508948283

Shahmohamadi, P., Che-Ani, A. I., Maulud, K. N., Tawil, N. M., and *Abdullah, N. A.*, 2011: The Impact of Anthropogenic Heat on Formation of Urban Heat Island and Energy Consumption Balance. *Urban Studies Res. 2011*(497524), 1–9. https://doi.org/10.1155/2011/497524

Singh, P., Kikon, N., and *Verma, P.*, 2017: Impact of land use change and urbanization on urban heat island in Lucknow city, Central India. A remote sensing based estimate. *Sustainable Cities and Society, 32*, 100-114. https://doi.org/10.1016/j.scs.2017.02.018

Singh, V., Singh, S., Biswal, A., Kesarkar, A. P., Mor, S., and *Ravindra, K.*, 2020: Diurnal and temporal changes in air pollution during COVID-19 strict lockdown over different regions of India. *Environ. Pollut. 266*(115368). https://doi.org/10.1016/j.envpol.2020.115368

Slater, P. N., Biggar, S. F., Holm, R. G., Jackson, R. D., Mao, Y., Moran, M. S., . . ., and *Yuan, B.*, 1987: Reflectance- and radiance-based methods for the in-flight absolute calibration of multispectral sensors. *Remote Sens. Environ. 22*(1), 11–37. https://doi.org/10.1016/0034-4257(87)90026-5

Sobrino, J. A., and *Romaguera, M.*, 2004: Land surface temperature retrieval from MSG1-SEVIRI data. *Remote Sens. Environ. 92*(2), 247–254. https://doi.org/10.1016/j.rse.2004.06.009

Sobrino, J. A., Jiménez-Muñoz, J. C., and *Paolini, L.*, 2004: Land surface temperature retrieval from LANDSAT TM 5. *Remote Sens. Environ. 90*(4), 434-440. https://doi.org/10.1016/j.rse.2004.02.003

Sobrino, J., Raissouni, N., Kerr, Y., Olioso, López García, M., Belaid, . . ., and *Dempere-Marco, L.*, 2000: *Teledetección* (1 ed.). Valencia, Comunidad Valenciana, Spain: Universidad de Valencia.

Soleimani Vosta Kolaei, F., and *Akhoondzadeh, M.*, 2018: A comparison of four methods for extracting Land Surface Emissivity and Temperature in the Thermal Infrared Hyperspectral Data. *Earth Observ. Geomatics Engin. 2*(1), 56–63. doi:10.22059/eoge.2018.239666.1011

Tobías, A., Carnerero, C., Reche, C., Massagué, J., Via, M., Minguillón, M. C., . . ., and Querol, X., 2020: Changes in air quality during the lockdown in Barcelona (Spain) one month into the SARS-CoV-2 epidemic. *Sci. Total Environ. 726*(138540). https://doi.org/10.1016/j.scitotenv.2020.138540

Tran, D. X., Pla, F., Latorre-Carmona, P., Myint, S. W., Caetano, M., and *Kieu, H. V.*, 2017: Characterizing the relationship between land use land cover change and land surface temperature. *ISPRS J. Photogram. Remote Sens. 124*, 119–132. https://doi.org/10.1016/j.isprsjprs.2017.01.001

Ursu, C-D., 2019: The land surface temperature evolution (LST) using LANDSAT scenes. Case study: The industrial platform Săvinești. *Geographia Technica 14*(2), 131–142. https://doi.org/10.21163/GT_2019.142.12

Valor, E., and *Caselles, V.*, 1996: Mapping land surface emissivity from NDVI: Application to European, African, and South American areas. *Remote Sens. Environ. 57*(3), 167–184. https://doi.org/10.1016/0034-4257(96)00039-9

Vlassova, L., Perez-Cabello, F., Nieto, H., Martín, P., Riaño, D., and *Riva, J. d.*, 2014: Assessment of Methods for Land Surface Temperature Retrieval from Landsat-5 TM Images Applicable to MultiscaleTree-Grass Ecosystem Modeling. *Remote Sens. 6*(5), 4345–4368. https://doi.org/10.3390/rs6054345

Walawender, J. P., Szymanowski, M., Hajto, M. J., and *Bokwa, A.*, 2014: Land Surface Temperature Patterns in the Urban Agglomeration of Krakow (Poland) Derived from Landsat-7/ETM+ Data. *Pure Appl. Geophys. 171*(6), 913–940. https://doi.org/10.1007/s00024-013-0685-7

Wan, Z., 2013: Collection-6 MODIS Land Surface Temperature Products Users' Guide. Retrieved 12 16, 2020, from Land Processes Distributed Active Archive Center (LP DAAC): https://lpdaac.usgs.gov/documents/118/MOD11_User_Guide_V6.pdf

Wang, Y., Zhan, Q., and *Ouyang, W.*, 2017: Impact of Urban Climate Landscape Patterns on Land Surface Temperature in Wuhan, China. *Sustainability 9*(10), 1700. https://doi.org/10.3390/su9101700

Wang, Z.-H., and *Upreti, R.*, 2019: A scenario analysis of thermal environmental changes induced by urban growth in Colorado River Basin, USA. *Landscape Urban Plan. 181*, 125–138. doi:10.1016/j.landurbplan.2018.10.002

Weng, Q., 2019: Land Surface Temperature Data Generation. In (Ed. *Q. Weng*) Techniques and Methods in Urban Remote Sensing (1 ed.) The Institute of Electrical and Electronics Engineers Press. 91–127. https://doi.org/10.1002/9781119307303.ch5

Xiao, R. B., Ouyang, Z. Y., Zheng, H., Li, W. F., Schienke, E. W., and *Wang, X. K.*, 2007: Spatial pattern of impervious surfaces and their impacts on land surface temperature in Beijing, China. *J. Environ. Sci. 19*(2), 250–256. https://doi.org/10.1016/S1001-0742(07)60041-2

Xie, J., and Zhu, Y., 2020: Association between ambient temperature and COVID-19 infection in 122 cities from China. *Sci. Total Environ. 724*(138201). https://doi.org/10.1016/j.scitotenv.2020.138201

Xu, H., 2015: Retrieval of the reflectance and land surface temperature of the newly-launched Landsat 8 satellite. *Chinese J. Geophys. 58*(3), 741–747. doi:10.6038/cjg20150304

Xu, H., Lin, D., and *Tang, F.*, 2012: The impact of impervious surface development on land surface temperature in a subtropical city: Xiamen, China. *Int. J. Climatol. 33*(8), 1873–1883. https://doi.org/10.1002/joc.3554

Yoo, C., Im, J., Park, S., and *Cho, D.*, 2017: Thermal Characteristics of Daegu using Land Cover Data and Satellite-derived Surface Temperature Downscaled Based on Machine Learning. *Korean J. Remote Sens. 33*, 1101–1118.

Yu, X., Guo, X., and *Wu, Z.*, 2014: Land Surface Temperature Retrieval from Landsat 8 TIRS—Comparison between Radiative Transfer Equation-Based Method, Split Window Algorithm and Single Channel Method. *Remote Sens. 6*(10), 9829–9852. https://doi.org/10.3390/rs6109829

Yuan, F. and *Bauer, M. E.*, 2007: Comparison of impervious surface area and normalized difference vegetation index as indicators of surface urban heat island effects in Landsat imagery. *Remote Sens. Environ. 106*(3), 375–386. https://doi.org/10.1016/j.rse.2006.09.003

Zhan, Q., Meng, F., and *Xiao, Y.*, 2015: Exploring the relationships of between land surface temperature, ground coverage ratio and building volume density in an urbanized environment. *Int. Arch. Photogramm. Remote Sens. Spatial Inf. Sci., XL-7/W3*, 255–260. https://doi.org/10.5194/isprsarchives-XL-7-W3-255-2015

Zsebeházi, G. and *Szépszó, G.*, 2020: Modeling the urban climate of Budapest using the SURFEX land surface model driven by the ALADIN-climate regional climate model results. *Időjárás 124*, 191–207. https://doi.org/10.28974/idojaras.2020.2.3

DOI:10.28974/idojaras.2022.2.4

IDŐJÁRÁS

Quarterly Journal of the Hungarian Meteorological Service
Vol. 126, No. 2, April – June, 2022, pp. 233–246

How human catabolism processes relate to the combustion of liquid fuels regarding oxygen consumption and carbon dioxide emissions in Hungary

György Szabados[1,*], **Iván Nagyszokolyai**[2], **Jozefin Hézer**[1], and **Tamás Koller**[3]

[1] *Department of Internal Combustion Engines and Propulsion Systems*
Audi Hungaria Faculty of Vehicle Engineering
Széchenyi István University, H-9026 Győr, Egyetem tér 1., Hungary

[2] *Department of Road and Rail Vehicles*
Faculty of Mechanical Engineering, Informatics and Electrical Engineering
Széchenyi István University, H-9026 Győr, Egyetem tér 1., Hungary

[3] *Multidisciplinary Doctoral School of Engineering Science*
Széchenyi István University, H-9026 Győr, Egyetem tér 1., Hungary

* *Corresponding Author e-mail: szabados.gyorgy.gergo@ga.sze.hu*

(Manuscript received in final form February 22, 2021)

Abstract— In connection with road vehicles and their internal combustion engines, their effects on our environment are being dealt with more and more. Plenty of parameters could be listed, but human catabolism and combustion of liquid fuels probably have not been examined together. Carbon dioxide has the most priority as a greenhouse gas in environmental change and metrology, thus it is a constant topic. Oxygen consumption has been examined rarely or never in such a context. In this article, calculations have been carried out from different points of view regarding these two parameters. The results of total-quantity calculations show, that the oxygen demand for the combustion of fuels used for road transport in 2019 in Hungary is the same as the 6-year oxygen demand of the Hungarian population, and the amount of the carbon dioxide emitted by the combustion of fuel used in road transport in Hungary is the same as the amount emitted by the Hungarian population during 5.2 years. The results might be worth examining on a larger scale.

Key-words: oxygen consumption, carbon dioxide emission, human population, transport emission, catabolism, environmental change

1. Introduction

Metabolism is a medical, biochemical term refers to the flow of matter, energy, and information in living organisms. One of the basic processes of metabolism is called catabolism. During catabolism, more complex materials, i.e., food which can be treated as hydrocarbon fuels for humans are broken down into simpler materials, releasing energy. This catabolic energy is converted into work in cells and reserve energy, and some of it is released as thermal energy. The main function of catabolism is to convert high-energy compounds into low-energy oxidized compounds. O_2 (oxygen) is needed to perform this process and CO_2 (carbon dioxide) is generated meanwhile (*Hawkins* and *Mans*, 1983). Oxygen enters the bloodstream through the lungs, and carbon dioxide escapes from the human body through the lungs as well (*Askanazi et al.,* 1980).

In internal combustion engines and fuel cells, metabolic processes are analogous to that of respiratory metabolism in a human body. Hydrocarbons are introduced into the engine in liquid or gaseous form. The oxygen required for oxidation comes from the ambient air. Oxidation of hydrocarbons releases heat that is utilized by the engine. In the case of theoretical and perfect combustion, CO_2 and H_2O (water) are formed. In reality, combustion is never perfect, but the volume ratio of pollutants generated is very small compared to CO_2 (*Heywood,* 1988).

There are rankings for what the number one problem is in the world today that will affect us in the next years, but scientists do not have the answer. It is also certain that everything is connected to everything. Climate change, ozone hole, pollution of waters, grounds, and pathogenic mutations that we are currently suffering from. Many attribute the reason for these to human intervention, among other the overpopulation and the human activity upsetting the environmental balance (*Businessinseider*, 2011; *Gallup International*, 2020; *Ipsos*, 2020).

Anthropogenic is an adjective that refers to an effect that depends on a person or human activity, or an effect caused by a person or human activity (*Fuge*, 2013). Nowadays, first and foremost, impact is nothing more than pollution. Let us go along this line, because the motor vehicle, as such, in its full reality, is a human creation from the conception of a man-made source of pollution, through its life, to the complete cessation of being a car. We can already see that financially the most expensive consequence for mitigating climate change can be found in automotive technology, and therefore, this sector is forced to work hard.

The anthropogenic ratio in emissions of combustion exhaust is 14–15%, from which 7–8% is due to the combined effect of water vapor + gases (e.g., CO_2, CH_4 (methane)). How can it affect the atmospheric warming / cooling to such an extent to guide the fight against carbon dioxide as a primary / most important aspect of energy supply, energy strategy? Global population growth of nearly fifty percent over the next thirsty years, which means, humanity of nine billion people is expected in 2050, to cause an order of magnitude greater change in the hydrological cycle and in water management as climate change is expected over the same thirsty years (*Kovács* and *Tompa*, 2012).

"It could easily be that we have reached a stage where facts, reason and truth are already helpless against propaganda." The greenhouse effect, rioting with the danger of global warming, the purpose of the forcible spread of so-called renewable energies is no different from the aspiration of the (research, business) lobbies interested in the issue to tap the central (state) budget (*Jacobsen*, 2011).

If the combustion of hydrocarbon-fuelled internal combustion engines were perfect and N_2 (nitrogen) was not oxidized, or hydrocarbons did not form particles, there would not be pollutants in the exhaust gas. However, there are some reasons in connection with combustion of any kinds of hydrocarbons, but especially with internal combustion engine why we may be in trouble (not to mention other pollutants such as NO_x and particulate matter):

- it removes a lot of oxygen from the air from the living being, and
- it emits carbon dioxide and water (water vapor) causing climate change (although this has not yet been fully proven).

The aim of this study is dual. Our first aim is to perform a triple comparative analysis by calculation, regarding vehicles with Otto-engine powered by gasoline, Diesel-engine with diesel, and fuel cell vehicles with fuel of hydrogen, where the investigated parameters are the oxygen consumption and the emission of CO_2. On the other hand, total-quantities have been calculated and compared as far as the fuels' combustion and human function regarding oxygen and carbon dioxide are concerned. This second aim is regarding only Hungary and its transport sector. Hopefully, it can make the readership curious to see how some of the rarely discussed metabolic processes evolve in the processes in terms of exact figures.

2. Calculation methodology and chosen propulsions

2.1. Theoretical combustion processes

Theoretical combustion calculations are being carried out to quantify how many O_2 needed for and CO_2 produced during the processes. For different fuel compositions, these parameters vary. The three investigated kind of fuels are gasoline, diesel, and hydrogen.

2.2. Development of parameters during a type approval test cycle of passenger cars

For a triple comparison, three different propulsions have been chosen. The first subject is a Toyota-branded Yaris vehicle powered by an Otto-engine with a rated power output of 51 kW (*Kraftfahrt Bundesamt*, 2020). The second is a hydrogen-fueled fuel cell of Toyota Mirai. The drive has a rated power of 55 kW (*Kraftfahrt*

Bundesamt, 2020). A diesel-powered Hyundai i20 in the same performance category would be the third one. It has a rated power of 55 kW (*Kraftfahrt Bundesamt*, 2020). Each of these cars has a fuel consumption value which is determined with the help of the standardized WLTC (worldwide harmonized light duty test cycle) cycle in every case. The make of the selected vehicles has no role in this study. An important consideration in the selection of vehicles was that the rated propulsion power should be similar to each other as much as it can be. The other important aspect was that the values of fuel consumption should be the result of testing vehicles for the same purpose. This was fulfilled, because the results come from the same cycle, which is WLTC, that is a part of the emission type approval process prescribed in the regulations used mainly in Europe or in the countries of the United Nations (*Official Journal of the European Union*, 2018; *UNECE*, 2021). The results available with each powertrain will be compared regarding the two investigated gaseous parameters.

2.3. Calculation method of total quantities

To compare the amounts of oxygen needed to burn fuels with humans' oxygen demand, the following calculation method has been used. Calculations have been conducted for the year 2019. As for the oxygen:

- To quantify the total oxygen demand for combusting the fuels used in the road transportation sector, theoretically two parameters are needed. The first one is the quantity of consumed fuels in Hungary in 2019 (*MÁSZ*, 2020), and the second one is the later calculated O_2 factors separately for each fuel (Eqs.(8),(15),(21)). Simple multiplication of these parameters would be the calculation method to get the result.
- For the calculation of humans' O_2 consumption, more parameters are needed. Firstly, the amount of oxygen consumed by a person in room conditions in one day is needed (*ELTE*, 2020). The standard density of the oxygen (at 1 bar, 15 °C) is also necessary (*Messer Hungarogáz Kft*., 2021a), with which the daily oxygen consumption can be determined on a mass base. A value is generated with a measurement unit of g O_2 / (person*day). If it is multiplied by the number of people in the population of Hungary in 2019 (*KSH*, 2020), we will get the oxygen consumption of the population per day. To get the consumption per year, it will be multiplied by the number of days in a year.

As for the carbon dioxide:

- The total carbon dioxide emission produced by combusting the fuels used in the road transportation sector can be calculated theoretically with the help of two parameters. The first one is the quantity of consumed fuels in Hungary (*MÁSZ*, 2020), and the second one would be the later calculated CO_2 factors, separately for each fuel (Eqs.(9),(16)). Simple multiplication of these parameters would be the calculation method.

- Similarly to the oxygen, the carbon dioxide emission of a population can be determined in a simplified way as follows: the CO_2 emission value under room conditions for a person daily would be the first parameter (*ELTE*, 2020). Using a standard density of the CO_2 (at 1 bar, 15 °C) (*Messer Hungarogáz Kft.*, 2021b), the emission result can be got on a mass base with a measurement unit g CO_2 / (person*day). It will be multiplied by the number of people in the population (*KSH*, 2020), and the total CO_2 emission value is obtained for a day which will be multiplied by the number of days in a year.

The calculations have been made with simplification, and its method has been greatly simplified. But the aim was not to give exact numerical values, only to show the magnitudes and to draw attention.

3. Calculations

3.1. Otto-engine vehicle with gasoline

Liquid fuels used in vehicles of road transportations are built up of hydrocarbons. The theoretical oxidation process of these hydrocarbons can be described as follows (*Hartmann* and *Braun*, 1973):

$$\mathrm{C_nH_m} + \left(\mathrm{n} + \frac{\mathrm{m}}{4}\right)\mathrm{O_2} \rightarrow \mathrm{nCO_2} + \frac{\mathrm{m}}{2}\mathrm{H_2O} + Q\,, \tag{1}$$

where Q is heat (not relevant here).

That is, combustion of a hydrocarbon containing a given amount of carbon and hydrogen requires a certain amount of oxygen. The oxidation process also generates a certain amount of carbon dioxide, water, and heat. According to *Mollenhauer* and *Tschoke* (2010), commercially available gasoline consists of -2–300 kinds of hydrocarbons. It has to be simplified, thus octane is used for our calculations as a surrogate for real gasoline (*Heywood*, 1988). With the help of Eq.(1) the octane's oxidations process is the following:

$$\mathrm{C_8H_{18}} + 12.5\mathrm{O_2} \rightarrow 8\mathrm{CO_2} + 9\mathrm{H_2O}\,. \tag{2}$$

As Eq.(2) is based on a unit of amount of substance (mol, kmol), a transition of the equation is needed to get a mass base equation. Molecular weights of chemical elements are used like C=12 kg/kmol, H = 1 kg/kmol, O =16 kg/kmol for the conversation (*Hartmann* and *Braun*, 1973). The mass based chemical equation develops:

$$8\ \text{kmol} * 12\frac{\text{kg}}{\text{kmol}}\ (\text{C}) + 18\ \text{kmol} * 1\frac{\text{kg}}{\text{kmol}}\ (\text{H}) + 12.5\ \text{kmol} * 32\frac{\text{kg}}{\text{kmol}}\ (\text{O}_2) \rightarrow$$
$$\rightarrow 8\ \text{kmol} * \left(12\frac{\text{kg}}{\text{kmol}} + 32\frac{\text{kg}}{\text{kmol}}\right)(\text{CO}_2) + 9\ \text{kmol} * \left(2\frac{\text{kg}}{\text{kmol}} + 16\frac{\text{kg}}{\text{kmol}}\right)(\text{H}_2\text{O})\ . \quad (3)$$

After multiplying and merging Eq.(3), Eq.(4) arises:

$$114\ \text{kg}\ (C_8H_{18}) + 400\ \text{kg}\ (O_2) \rightarrow 352\ \text{kg}\ (CO_2) + 162\ \text{kg}\ (H_2O). \quad (4)$$

Two specific factors per unit mass of fuel can already be determined, from which the first would be the oxygen consumption. For combusting one unit of mass of octane, 3.51 kg of O_2 is needed:

$$\frac{400\ \text{kg}\ (\text{O}_2)}{114\ \text{kg}\ (\text{C}_8\text{H}_{18})} = \mathbf{3.51}\,\frac{\mathbf{kg\ (O_2)}}{\mathbf{kg\ (C_8H_{18})}}\ . \quad (5)$$

To determine the second parameter, which is the mass related CO_2 emission, Eq.(4) is used as well. The result in terms of per unit mass of fuel is the following:

$$\frac{352\ \text{kg}\ (\text{CO}_2)}{114\ \text{kg}\ (\text{C}_8\text{H}_{18})} = \mathbf{3.09}\ \frac{\mathbf{kg\ (CO_2)}}{\mathbf{kg\ (C_8H_{18})}}\ . \quad (6)$$

The specific fuel consumption related to distance traveled of the Otto-engine vehicle measured during a WLTC cycle is B_{gasoline} (volume) = 5.4 liters gasoline/100km (*Kraftfahrt Bundesamt*, 2020). That should be converted to a value containing fuel mass related to distance. To do so, an average density of the gasoline is needed, which is ρ = 0.75 kg/liter (*European Committee for Standardization*, 2008). We get the next equation:

$$B_{\text{gasoline}}(\text{mass}) = 5.4\frac{\text{liters}}{100\text{km}} * 0.75\frac{\text{kg}}{\text{liter}} = 4.05\frac{\text{kg}}{100\text{km}}. \quad (7)$$

Hereinafter the distance-related (100 km) O_2 consumption and CO_2 emission can be calculated for the Otto-engine vehicle:

$$4.05\frac{\text{kg (gasoline)}}{100\text{km}} * 3.51\frac{\text{kg}\ (\text{O}_2)}{\text{kg}\ (\text{C}_8\text{H}_{18})} = \mathbf{14.18}\frac{\mathbf{kg\ (O_2)}}{\mathbf{100km}}\ , \quad (8)$$

$$4.05\frac{\text{kg (gasoline)}}{\text{100km}} * 3.09\frac{\text{kg }(CO_2)}{\text{kg }(C_8H_{18})} = \mathbf{12.51}\frac{\mathbf{kg\ (CO_2)}}{\mathbf{100km}}\ . \tag{9}$$

3.2. *Diesel-engine vehicle with diesel*

According to the scientific literature (*Mollenhauer* and *Tschoke*, 2010), diesel consists of several more types of different hydrocarbons than it is in the case of gasoline. For theoretical calculation it must be simplified, which means a surrogate has to be chosen. This surrogate will be the cetane (hexadecane) (*Heywood,* 1988). Based on Eq.(1), the theoretical oxidation process of hexadecane is the following:

$$C_{16}H_{34} + 24.5O_2 \rightarrow 16\ CO_2 + 17\ H_2O\ . \tag{10}$$

After converting Eq.(10) to a mass base equation, which is followed by multiplying and merging, Eq.(11) arises:

$$226\text{ kg }(C_{16}H_{34}) + 784\text{ kg }(O_2) \rightarrow 704\text{ kg }(CO_2) + 306\text{ kg }(H_2O)\ . \tag{11}$$

Two specific factors per unit mass of fuel can already be determined, from which the first would be the oxygen consumption. For combusting one unit of mass of cetane, 3.12 kg of O_2 is needed as indicated in the following equation:

$$\frac{704\text{ kg }(O_2)}{226\text{ kg }(C_{16}H_{34})} = \mathbf{3.12}\frac{\mathbf{kg\ (O_2)}}{\mathbf{kg\ (C_{16}H_{34})}}\ . \tag{12}$$

To determine the CO_2 emission, Eq.(11) can be used as well. The result in terms of per unit mass of cetane is the following:

$$\frac{704\text{ kg }(CO_2)}{226\text{ kg }(C_{16}H_{34})} = \mathbf{3.16}\ \frac{\mathbf{kg\ (CO_2)}}{\mathbf{kg\ (C_{16}H_{34})}}. \tag{13}$$

The chosen Diesel-engine vehicle has a distance-related fuel consumption value which is B_{diesel} (volume) = 5.2 liters diesel/100 km (*Kraftfahrt Bundesamt*, 2020). With the help of an average density value of 0.85 kg/liter of diesel (*European Committee for Standardization*, 2005), fuel mass consumed can be calculated:

$$B_{\text{diesel}}\,(\text{mass}) = 5.2\ \text{liters/100km} * 0.85\ \text{kg/liter} = 4.42\ \text{kg/100km}\,. \quad (14)$$

Using Eqs. (12),(13), and (14), the distance-related oxygen consumption and the carbon dioxide emission can be quantified. These are shown in the following equations:

$$4.42\,\frac{\text{kg (diesel)}}{100\text{km}} * 3.12\,\frac{\text{kg}\,(\text{O}_2)}{\text{kg}\,(\text{C}_{16}\text{H}_{34})} = \mathbf{13.79}\,\frac{\mathbf{kg\,(O_2)}}{\mathbf{100km}}\,, \quad (15)$$

$$4.42\,\frac{\text{kg (diesel)}}{100\text{km}} * 3.16\,\frac{\text{kg}\,(\text{CO}_2)}{\text{kg}\,(\text{C}_{16}\text{H}_{34})} = \mathbf{13.97}\,\frac{\mathbf{kg\,(CO_2)}}{\mathbf{100km}}\,. \quad (16)$$

3.3. *Hydrogen fuel-cell vehicle*

In the fuel cell, which generates electricity using hydrogen, the following chemical process takes place (*Eichlseder* and *Klell*, 2010):

$$H_2 + \tfrac{1}{2}\,O_2 \rightarrow H_2O + Q, \quad (17)$$

that is, hydrogen is oxidized by oxygen from the air to form water. In this case, heat, indiced by *Q*, is also generated, but in our case, it is not relevant now. Using the molecular weights, we bring the equation on a mass basis:

$$2\text{kmol} * 1\,\frac{\text{kg}}{\text{kmol}}\ (\text{H}) + \frac{1}{2}\text{kmol} * 2 * 16\,\frac{\text{kg}}{\text{kmol}}\ (\text{O}) \rightarrow 1\text{kmol} * \left(2\,\frac{\text{kg}}{\text{kmol}} + 16\,\frac{\text{kg}}{\text{kmol}}\right)(\text{H}_2\text{O}). \quad (18)$$

By multiplying in Eq.(18), it will be:

$$2\ \text{kg}\ (H_2) + 16\ \text{kg}\ (O_2) \rightarrow 18\ \text{kg}\ (H_2O)\,. \quad (19)$$

Two specific factors per unit mass of fuel can already be determined. The result is shown in the following equation for e O_2, while CO_2 emission does not appear:

$$\frac{16\ \text{kg}\,(\text{O}_2)}{2\ \text{kg}\,(\text{H}_2)} = \mathbf{8}\ \frac{\mathbf{kg\,(O_2)}}{\mathbf{kg\,(H_2)}}\,. \quad (20)$$

Calculation of distance-related O_2 consumption of a hydrogen fuel-cell vehicle happens as follows. Firstly, fuel consumption is needed. It was determined in this case as well during a WLTC driving cycle: $B_{hydrogen}$ (mass)=0.8 kg hydrogen/100 km (*Kraftfahrt Bundesamt*, 2020). Using the above formula, we can calculate the specific oxygen consumption for the distance traveled (100 km):

$$0.8\,\frac{\mathrm{kg\,(H_2)}}{100\mathrm{km}} * 8\,\frac{\mathrm{kg\,(O_2)}}{\mathrm{kg\,(H_2)}} = \mathbf{6.40}\,\frac{\mathbf{kg\,(O_2)}}{\mathbf{100km}}\,. \tag{21}$$

3.4. *Calculation of human properties and characteristic of fuel combustion – total quantities*

Calculations have been conducted with the help of the method described in Subsection 2.3. The amount of oxygen consumed by combusting fuels is

$$\mathrm{m_{O_2\ consumed\ (gasoline)}} = \mathrm{m_{gasoline\ consumed}} \times \mathrm{O_2\ factor_{gasoline}} =$$
$$= 1\,114\,907\,107\ \mathrm{kg} \times 3.51\,\frac{\mathrm{kg\,(O_2)}}{\mathrm{kg\ gasoline}} = 3\,902\,174\,874\ \mathrm{kg}\,, \tag{22}$$

$$\mathrm{m_{O_2\ consumed\ (diesel)}} = \mathrm{m_{diesel\ consumed}} \times \mathrm{O_2\ factor_{diesel}} =$$
$$= 2\,068\,402\,409\ \mathrm{kg} \times 3.12\,\frac{\mathrm{kg\,(O_2)}}{\mathrm{kg\ diesel}} = 6\,412\,047\,468\ \mathrm{kg}\,, \tag{23}$$

$$\mathrm{m_{O_2\ consumed\ (total)}} = \mathrm{m_{O_2\ consumed\ (gasoline)}} + \mathrm{m_{O_2\ consumed\ (diesel)}} =$$
$$= 3\,902\,174\,874\ \mathrm{kg} + 6\,412\,047\,468\ \mathrm{kg} = 10\,314\,222\,342\ \mathrm{kg}\,. \tag{24}$$

Oxygen consumed by population:

$$\mathrm{m_{O_2\ consumed\ (population)}} = \mathrm{V_{\frac{O_2\ consumed}{person \times day}}} \times \rho_{\mathrm{O_2\ standard}} \times \mathrm{population} \times \mathrm{days} =$$
$$= 360\ \mathrm{dm^3} \times 1.337\,\frac{\mathrm{g}}{\mathrm{dm^3}} \times 9\,778\,371 \times 365 = 1\,717\,881\,818\ \mathrm{kg}\,. \tag{25}$$

O_2 consumption values are shown in *Table 2.* and will be discussed in the next section. The amount of carbon dioxide emitted by fuel combustion is

$$\mathrm{m_{CO_2\ emitted\ (gasoline)}} = \mathrm{m_{gasoline\ consumed}} \times \mathrm{CO_2\ factor_{gasoline}} =$$
$$= 1\,114\,907\,107\ \mathrm{kg} \times 3.09\,\frac{\mathrm{kg\,(CO_2)}}{\mathrm{kg\ gasoline}} = 3\,456\,212\,031\ \mathrm{kg}\,, \tag{26}$$

$$\mathrm{m}_{\mathrm{CO_2\ emitted\ (diesel)}} = \mathrm{m}_{\mathrm{diesel\ consumed}} \times \mathrm{CO_2\ factor}_{\mathrm{diesel}} = \\ = 2\ 068\ 402\ 409\ \mathrm{kg}\ \times 3.16\ \frac{\mathrm{kg\ (CO_2)}}{\mathrm{kg\ diesel}} = 6\ 412\ 047\ 468\ \mathrm{kg}\ , \qquad (27)$$

$$\mathrm{m}_{\mathrm{CO_2\ emitted\ (total)}} = \mathrm{m}_{\mathrm{CO_2\ emitted\ (gasoline)}} + \mathrm{m}_{\mathrm{CO_2\ emitted\ (diesel)}} = \\ = 3\ 456\ 212\ 031\ \mathrm{kg} + \ 6\ 412\ 047\ 468\ \mathrm{kg} = 9\ 868\ 259\ 499\ \mathrm{kg}\ . \qquad (28)$$

The amount of carbon dioxide emitted by population is

$$\mathrm{m}_{\mathrm{CO_2\ emitted\ (population)}} = \mathrm{V}_{\frac{\mathrm{CO_2\ emitted}}{\mathrm{person \times day}}} \times \ \rho_{\mathrm{CO_2\ standard}} \ \times \mathrm{population} \times \mathrm{days} \\ = 288\ \mathrm{dm}^3 \times 1.8474\ \frac{\mathrm{g}}{\mathrm{dm}^3}\ \times\ 9\ 778\ 371\ \ \times 365 = 1\ 898\ 946\ 819\ \mathrm{kg}\ . \qquad (29)$$

CO_2 emission values are shown in *Table 3* and will be discussed in the next section.

4. Results and discussion

4.1. Comparison of propulsions

The results of comparison of propulsions are shown in *Table 1*. This table consists of three table-sections. The top table-section summarizes the results regarding the oxidation of different fuels. The smaller the molecule which is oxidized, the more oxygen needed for the oxidation. Accordingly, the oxidation of hydrogen needs the most amount of oxygen, it is followed by the oxidation of gasoline, and the least is for diesel. As for the CO_2 formation, it is not produced during the combustion of hydrogen, because there is no carbon in the molecule. Octane which has carbon in its molecule formats CO_2 during oxidation, but this amount is less than in case of diesel, which has the most carbon in molecule.

In the middle table-section, the table deals with results realized during a WLTC cycle. Values of oxygen consumption show another tendency among fuels compared to the results of simple oxidation. This is because of the different energy content of fuels and the different efficiency of the propulsion calculated from heat power of fuel to the power of vehicle's wheel. The hydrogen fuel-cell vehicle has the lowest O_2 consumption, and the highest one belongs to the Otto-engine vehicle. In case of a Diesel-engine vehicle it is a bit lower compared to the vehicle using gasoline during a WLTC cycle. CO_2 emission is proportional to the carbon content of the fuel. Fuel-cell vehicle has zero emission. Diesel-engine vehicle has the highest CO_2 emission, while that is a bit lower for the Otto-engine vehicle compared to the diesel.

The lowest section of the table represents the results derived from the middle section's WLTC results. This sums up what has been said so far. There is a slight difference between Otto and Diesel. Oxygen consumption of fuel-cell vehicle is the half of those the two other propulsion conception. As far as the CO_2 emission is concerned it is not produced from the process of the fuel cell while diesel's value is slightly higher than that of the Otto-engine vehicle.

Table 1. Results of propulsions' comparison

O_2 consumption and CO_2 emission	Specific oxygen consumption $[\frac{\mathrm{kg}\ (\mathrm{CO}_2)}{\mathrm{kg}\ (\mathrm{C}_n\mathrm{H}_m\ \mathrm{or}\ \mathrm{H}_2)}]$	Specific carbon dioxide emission $[\frac{\mathrm{kg}\ (\mathrm{CO}_2)}{\mathrm{kg}\ (\mathrm{C}_n\mathrm{H}_m\ \mathrm{or}\ \mathrm{H}_2)}]$
Oxidation of octane	3.51	3.09
Oxidation of hexadecane	3.12	3.16
Oxidation of hydrogen	8	0
O_2 consumption and CO_2 emission	Specific oxygen consumption during a WLTC cycle $[\frac{\mathrm{kg}\ (\mathrm{O}_2)}{100\ \mathrm{km}}]$	Specific carbon dioxide emission during a WLTC cycle $[\frac{\mathrm{kg}\ (\mathrm{CO}_2)}{100\ \mathrm{km}}]$
Otto-engine vehicle	14.18	12.51
Diesel- engine vehicle	13.79	13.97
Hydrogen fuel-cell vehicle	6.40	0
Comparison of propulsions	Specific oxygen consumption during a WLTC cycle $[\frac{\mathrm{kg}\ (\mathrm{O}_2)}{100\ \mathrm{km}}]$	Specific carbon dioxide emission during a WLTC cycle $[\frac{\mathrm{kg}\ (\mathrm{CO}_2)}{100\ \mathrm{km}}]$
Otto-engine vehicle / Diesel-engine vehicle	1.03	0.91
Otto-engine vehicle / Hydrogen fuel-cell vehicle	2.22	NA
Diesel-engine vehicle / Hydrogen fuel-cell vehicle	2.15	NA

4.2. The relationship between human properties and characteristics of fuel combustion – total quantities

The results of the comparison with the humans' parameters are shown in *Tables 2* and *3*. Here, too, we would like to emphasize that the calculations have been made with a high degree of simplification, and its method has been greatly simplified. The aim was not to give exact numerical values, but only to show the magnitudes and to draw attention. The oxygen consumption of the combustion of fuels used in the road transportation in Hungary during a year was as much as the amount of oxygen used by the number of people meeting the Hungarian population for 6 years. In the same way, the number of people meeting the Hungarian population for 5.2 years realizes as much CO_2 emission as it is produced by combustion fuels in the road transport in Hungary for a year.

Table 2. O_2 quantities consumed by fuels and population

Fuel	**Fuel amount used [kg/year (2019)]**	**Amount of O_2 consumed by fuel [kg / year (2019)]**
Gasoline	1 114 907 107	3 902 174 874
Diesel	2 068 402 409	6 412 047 468
Total O_2 consumed by fuel		10 314 222 342
Amount of O_2 consumed by population [kg/year (2019)]		1 717 881 818
$\frac{\mathbf{O_2\ consumed\ by\ fuel}}{\mathbf{O_2\ consumed\ by\ population}}$ **[year]**		**6.00**

Table 3. CO_2 quantities emitted by combustion of fuels and population

Fuel	**Fuel amount used [kg / year (2019)]**	**CO_2 emitted by fuel combustion [kg / year (2019)]**
Gasoline	1 114 907 107	3 456 212 031
Diesel	2 068 402 409	6 412 047 468
Total CO_2 emitted by fuel combustion		9 868 259 499
CO_2 emitted by population [kg / year (2019)]		1 898 946 819
$\frac{\mathbf{CO_2\ emitted\ by\ fuel\ combustion}}{\mathbf{CO_2\ emitted\ by\ population}}$ **[year]**		**5.20**

5. Conclusions

In this article, different calculations have been conducted for two very important but together very rarely investigated gas phase components: O_2 and CO_2. First, different propulsions of vehicles were calculated and compared. In order to find the link between the human properties and the properties of the combustion of transportation's fuels regarding the two basic parameters (oxygen consumption and carbon dioxide emission), a second set of calculations were made. The following conclusions can be drawn:

- Comparisons between the propulsion systems during a WLTC cycle:
  - Vehicles with Otto-engine consume the most amount of oxygen. It is followed by the vehicles propelled by a Diesel-engine, and the lowest consumption showed by the fuel-cell vehicles.
  - A fuel-cell vehicle does not emit any CO_2, while the Diesel vehicles have the highest level of CO_2 emission, and the Otto-vehicles' result is in between.
- The O_2 demand for combusting the fuels used in road transport in Hungary is the same as the 6-year demand of a Hungarian population in the year 2019.
- As for the CO_2 emission, combustion of fuels used in road transport in Hungary emits the same as the emission of the Hungarian population during 5.2years.
- Results seem to be serious, although calculations are relating only to the road transport in a small country of the world.

5.1. Additional investigation options

In authors' opinion, the topic has been analyzed and represented above can be further investigated probably in the ways as follows:

- Examining how the real conditions could be approached as far as the combustion of fuels, the function of oxygen consumption, and the carbon dioxide emission in a human body are concerned.
- Investigation could be extended to other sectors (energy, industry, households, agriculture).
- Extensions can be made towards larger population and vehicle fleet.
- Examining the effects that can have this tendency (especially the oxygen) on the humans or living organisms on a long term.

References

Askanazi, J., Silverberg, P.A., Foster, R.J., Hyman, A.I., Milic-Emili, J., and *Kinney, J.M.*, 1980: Effects of respiratory apparatus on breathing pattern. *J. Appl. Physiol. 48*, 577–580. https://doi.org/10.1152/jappl.1980.48.4.577

Businessinseider, 2011: The 10 Biggest Problems In The World According To The EU. Available online: https://www.businessinsider.com/the-10-biggest-problems-in-the-world-according-to-the-eu-2011-10

Eichlseder, H. and *Klell, M.*, 2010: Wasserstoff in der Fahrzeugtechnik: Erzeugung, Speicherung, Anwendung. Springer-Verlag. (in German)

ELTE (Eötvös Lóránd Tudományegyetem), 2020: A légzési gázok szállítása, a légzőrendszer szerveződése. (in Hungarian) Available online: http://physiology.elte.hu/eloadas/bev_biol_3/Elettan6_legzes_2017.pdf

European Committee for Standardization, 2005: "EUROPEAN STANDARD EN 590 Automotive fuels. Diesel. Requirements and test methods" CEN-Euro-pean Committee for Standardization. Brussels, Belgium.

European Committee for Standardization, 2008: EUROPEAN STANDARD EN 228 Automotive fuels. Unleaded petrol. Requirements and test methods" CEN-European Committee for Standardization. Brussels, Belgium.

Fuge R., 2013: Anthropogenic Sources. In: (ed. *Selinus, O.*) Essentials of Medical Geology. Springer, Dordrecht. https://doi.org/10.1007/978-94-007-4375-5_4

Gallup International, 2020: World's most important problem. Available online: https://news.gallup.com/poll/1675/most-important-problem.aspx

Hartmann and *Braun*, 1973: Verbrennungstechnik. Hartmann and Braun AG (in German)

Hawkins, R.A. and *Mans A.M.*, 1983: Intermediary Metabolism of Carbohydrates and Other Fuels. In: (ed. *Lajtha, A.*) Metabolism in the Nervous System. Springer, Boston, MA. https://doi.org/10.1007/978-1-4684-4367-7_10

Heywood, J.B., 1988: Combustion engine fundamentals. 1ª Edição. Estados Unidos.

Ipsos, 2020: What-worries-world-january-2020. Available online: https://www.ipsos.com/en/what-worries-world-january-2020

Jacobsen, G.D., 2011: The Al Gore effect: an inconvenient truth and voluntary carbon offsets. *J. Environ. Econom. Manage. 61*, 67–78. https://doi.org/10.1016/j.jeem.2010.08.002

Kovács, F. and *Tompa, R.*, 2012: A klímaváltozás és az ipari széndioxid kapcsolatának kérdéseiről. *Műszaki Földtudományi Közlemények, 83*. 111–117. (in Hungarian)

KSH (Központi Statisztikai Hivatal), 2020: Összefoglaló táblák (STADAT) - Idősoros éves, területi adatok - Népesség, népmozgalom. Available online: https://www.ksh.hu/stadat_eves_6_1 (in Hungarian)

Kraftfahrt Bundesamt, 2020: CO_2-Emissions- und Kraftstoffverbrauchs-Typprüfwerte von Kraftfahrzeugen zur Personenbeförderung mit höchstens neun Sitzplätzen und Wohnmobilen (Klasse M1: Pkw, Wohnmobile) Stand: 15. März 2020 SV 2.2.2. Available online: https://www.kba.de/SharedDocs/Downloads/DE/SV/sv222_m1_kraft_pdf.pdf?_blob=publicationFileandv=2 (in German)

MÁSZ (Magyar Ásványolaj Szövetség), 2020: A MÁSZ tagvállalatok összesített üzemanyag értékesítései 2019. Available online: http://petroleum.hu/dokumentumok/uzemanyag-statisztikak/ (in Hungarian)

Messer Hungarogáz Kft., 2021a: Termékadatlapok: Oxigén 2.5. Available online: https://www.messer.hu/termekadatlapok (in Hungarian)

Messer Hungarogáz Kft., 2021b: Termékadatlapok: Szén-dioxid 2.8. Available online: https://www.messer.hu/termekadatlapok (in Hungarian)

Mollenhauer, K. and *Tschoke, H. (Eds.)*, 2010: Handbook of diesel engines (Vol. 1). Berlin: Springer.

Official Journal of the European Union, 2018: COMMISSION REGULATION (EU) 2018/1832 of 5 Nov. 2018 amending Directive 2007/46/EC of the Eur. Parliament and of the Council, Com.Regulation (EC) No 692/2008 and Com. Regulation (EU) 2017/1151 for the purpose of improving the emission type approval tests and procedures for light passenger and commercial vehicles, including those for in-service conformity and real-driving emissions and introducing devices for monitoring the consumption of fuel and electric energy. Available online: https://eur-lex.europa.eu/legal-content/HU/TXT/?uri=CELEX%3A32018R1832andqid=1648028563601

United Nations Economic Commission for Europe (UNECE), 2021: Uniform provisions concerning the approval of vehicles with regard to the emission of pollutants according to engine fuel requirements. Available online: https://unece.org/transport/vehicle-regulations-wp29/standards/addenda-1958-agreement-regulations-81-100

DOI:10.28974/idojaras.2022.2.5

IDŐJÁRÁS

Quarterly Journal of the Hungarian Meteorological Service
Vol. 126, No. 2, April – June, 2022, pp. 247–265

Selecting the best general circulation model and historical period to determine the effects of climate change on precipitation

Mostafa Yaghoobzadeh[1, 2]

[1]*Department of Water Engineering,*
University of Birjand, Birjand, Iran

[2]*Research Group of Drought and Climate change,*
University of Birjand, Birjand, Iran

Author E-mail: M.Yaghoobzadeh@birjand.ac.ir

(Manuscript received in final form March 1, 2022)

Abstract— Assessing the effects of climate change is a key component of the sustainable management of water resources and food security. In this paper, general circulation models (GCM) were evaluated using historical information for Birjand synoptic station, Iran. Modeling was performed using 35 models of the Fifth Climate Change Report for 27 historical periods. The results showed that longer annual periods are the most suitable periods for hydrological simulation when data are available. Therefore, the periods of 1960-1990 may be the most appropriate periods due to the adaptation to the observation data. To estimate rainfall, periods with more years showed a more accurate forecast of the future. Moreover, the results showed more changes in the RCP 8.5 scenario than in the RCP 4.5 scenario. According to the comparison of models, the NorESM1-M model with a root mean square error (RMSE) of 0.091 and the GISS-E2-R model with a low percent bias (PBIAS) can be an appropriate model for estimating rainfall.

Key-words: climate change, CIMP5, historical period, precipitation

1. Introduction

The practical activities for considering the climate change and drought effects on agriculture and water resources are recently increasing in the world (*Karasakal et al.,* 2020a, 2020b; *Tao et al.,* 2021; *Wang et al.,* 2021; *Xu et al.,* 2021; *Zhang et al.,* 2021). Climate change can affect various aspects of communities, including sustainable water management (*Huang et al.,* 2021), environmental protection

(*Rjoub et al.,* 2021; *Oladipupo et al*., 2022), energy supply (*Odugbesan* and *Rjoub*, 2020; *Hou et al*., 2021; *Adebayo et al.,* 2021a, 2021b, 2022), economic growth (*Lin et al.,* 2021), ecological footprint (*Ahmed et al*., 2021), and food security (*Gholamin* and *Khayatnezhad*, 2020, 2021).

As the Middle East is located in the arid region of the world, it has a lot of problems to deal with due to the limitation of the water resources in the region, the increasing demand for water due to the increase of urbanization, and the intensifying global warming (*Li et al*., 2021b; *Ma et al*., 2021; *Sun* and *Khayatnezhad*, 2021; *Zhu et al.,* 2021). Global warming, changes in spatial and temporal precipitation patterns, as well as changes in the prediction of these changes are likely to occur in the next century (*Godage et al.,* 2021). Temperatures, which have risen about 0.6 °C since 1860, are projected to rise from 2 to 4 °C until 2100 compared to the period from 1850 to 1950 (IPCC, 2007; *Zhang et al.,* 2019; *Zhao et al.,* 2021; *Chen et al*., 2022).

Climate change effects on natural ecosystems are one of the most critical consequences (*Wang et al*., 2022). It causes a change in the production and services of these resources and, ultimately, the benefits derived from them. Changes in the quality and quantity of water resources, the condition of forests and pastures, green space, wildlife, aquatic animals, etc. can be mentioned (*Ren* and *Khayatnezhad*, 2021).

Regarding the requirement for this vital substance in all human activities, one of the main concerns of experts in different science fields due to climate change is the effects on water resources (*Fung et al*., 2010). Any change in these variables can affect natural ecosystems' yield rate and structure since the variables of precipitation, temperature, and solar radiation are the most critical inputs of natural ecosystems, especially watersheds (*Tangonyire*, 2019; *Mahmood et al*., 2019; *Li et al.,* 2021a; *Yin et al*., 2022a). Undoubtedly, the available water in a watershed is the most sensitive and vital factor in the economic, social, environmental processes, which is affected by climate change. Therefore, investigating climate change effect on this vital substance has particular importance.

Atmospheric general circulation models (AOGCM) simulate the climatic system of Earth's evolution at any given time, including atmospheric, ocean, ice, sea, land, and atmospheric conditions (*D'Agata et al.,* 2020; *Rahman* and *Islam,* 2020; *Kong*, 2020; *Yin et al*., 2022b; *Quan et al*., 2022). To create and modify complex terrestrial climate variables, atmospheric circulation models describe how these components interact with each model. Therefore, they are known as a vital instrument to stimulate climate change and estimate the future (*Mogano* and *Mokoele*, 2019; *Nourani et al*., 2019; *Afshar et al*., 2021; *Guo et al*., 2021; *Sun et al.,* 2021).

Due to comparing climate change models, *Gregory et al.* (2001) compared ten models of the Third Climate Change Report, and *Samadi et al.* (2010) compared 11 models of the Fourth Climate Change Report. *Kamal* and *Massah*

Boani (2012) compared the impact of uncertainties of seven TAR models (Third Climate Change Report) including the CCSR, CGCM2, CSIRO-MK2, ECHAM4, GFDL-R30, HadCM3, NCAR-DOE PCM models and nine selected models from AR4 (Fourth Climate Change Report) including the CCSM3, CGCM3, CSIRO Mk3, GFDL CM2.1, GISS ER, HadCM3, ECHAM5, MIROC-med, PCM models under A2 release scenario on the runoff of Qarah su Basin in 2040–2069. Their results showed that using AR4 models with more management of uncertainty leads to more practical results than using TAR models.

The choice of the appropriate historical period affects climate change results and the importance of the type of selected GCM model. In the Fourth Climate Change Report, historical and future period data were presented simultaneously (*Yaghoobzadeh et al.*, 2017). For this reason, researchers such as *Mousavi et al.* (2016) used the 1980–2010 period to determine climate change effects by presenting the data of the Fifth Climate Change report. Based on their results, the separation of historical periods from future ones, the elective historical period should preferably be chosen by the 2005 year period. Choosing a historical period and the future one is very essential for climate change research. Choosing a historical period is very essential in choosing a future period. Despite global warming and rising temperatures, the historical period closer to the present shows more temperature changes than in the years before 2000, and these effects of temperature changes affect the goal of each researcher. On the other hand, in downscaling methods such as LARS-WG, and in particular the coefficient of variation of the coefficient of change factor, the number of historical and future periods should be as uniform as possible, which makes the need to consider periods with the appropriate number of years more obvious.

No specific research has been done so far on choosing a suitable historical period for assessing the future climate change effects. Hence, for the stations with more extended metering periods, it is always essential to choose a suitable historical period that responds well to future changes. Due to the Fourth Climate Change Report, the 1960–1990 period was selected as an appropriate period by the Intergovernmental Panel on Climate Change (IPCC), and the 1970–2000 period after the 1960–1990 period can be selected as an appropriate period (IPCC, 2007). According to the Fourth Climate Change Report, some researchers have chosen these periods as the appropriate historical period in their research. For example, the 1961-1990 period was used as a suitable period for many researchers to evaluate the variables of precipitation, and minimum and maximum temperature (*Alvankar et al.,* 2016; *Parracho et al.,* 2016; *Nourani et al*., 2020; *Oseke et al.,* 2021; *Nabipour et al*., 2020; *Sibuea et al*., 2021). Considering the fifth report, the 1986–2005 period was also discussed, and future changes compared to this period were examined. However, the 1970–2000 period was used as a training period (IPCC, 2013).

Each researcher has used a specific historical period in his research so that no suitable answer can be found for why he chose this period. *Shen et al.* (2018)

used the 1971–2000 historical period, and *Zhang et al.* (2018) used the 1961–1990 period to evaluate the effect of climate change effect on hydrological characteristics in future periods. Selecting the appropriate historical period also depends on appropriate data availability from the synoptic stations, which may be forced to use shorter periods due to a lack of data. Due to the synoptic data existence since 1992, *Weinberger et al.* (2017) used the 1992–2002 period to estimate temperatures in ten regions of the United States. However, in case of available data, choosing a 30-year-long period is better than other elective periods. *Sobhani et al.* (2017) used the 1970–1999 and the 1961–1990 periods to estimate precipitation and temperature variables in the future, respectively. Given the availability of the Fifth Reporting Period for all models up to 2005, choosing the post-2005 historical period for the Fifth Report data is fraught with errors, and researchers should use the early years of the future for the years after 2005. *Kouhestani et al.* (2016) used the long period of 1948–2014 as a historical period.

Selecting the AOGCM model and the appropriate historical period can express the results with -ranging changes. We tried to select the appropriate model from almost all CMIP5 models (Fifth Climate Change Report) to estimate precipitation parameters in the future period, and limit values, relative error percentages and meteorological parameters' uncertainty were calculated for all models and periods as well.

2. Material and methods

Precipitation values for 35 GCM models of the fifth report and 27 selected historical periods of Birjand synoptic station data were evaluated to select appropriate GCM models and historical periods for climate change research. The city of Birjand is located in eastern Iran and has an arid and semi-arid climate with an average rainfall of 170 mm per year (*Fig. 1*).

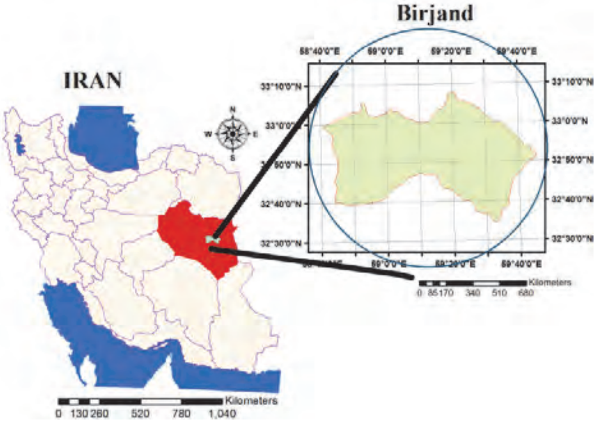

Fig. 1. Location of the study area.

In order to conduct this research, historical precipitation data of GCM models were first obtained from the IPCC site in the Fifth Climate Change Report. After collecting report data on meteorological variables resulting from GCM models that are monthly for Birjand, the selected periods were determined using the estimated months and years of the models and compared with the results of observation station periods using error estimation methods. *Tables 1* and *2* present the Fifth Climate Change Report's models and the selected periods used in this study, respectively.

Table 1. The models of the fifth climate change report presented in this research

ACCESS1	1.25° ×1.87°	Commonwealth Scientific and Industrial Research Organization, Australia
ACCESS1.3	1.25° ×1.87°	Commonwealth Scientific and Industrial Research Organization, Australia
BCC-CSM1.1	2.8° × 2.8°	Beijing Climate Center, China Meteorological Administration, China
BCC-CSM1-M	2.8° × 2.8°	Beijing Climate Center, China Meteorological Administration, China
BNU-ESM	2.8° × 2.8°	College of Global Change and Earth System Science, Beijing Normal University, China
CanESM2	2.8° × 2.8°	Canadian Centre for Climate Modeling and Analysis, Canada
CCSM4	1°× 1°	NCAR, University Corporation for Atmospheric Research, United States
CESM1-BGC	1°× 1°	National Science Foundation, United States
CESM1-CAM5	0.94° ×1.25°	National Science Foundation, United States
CMCC-CMS	3.71° ×3.75°	Centro Euro-Mediterraneo per I Cambiamenti Clamatici, Italy
CNRM-CM5	1.4° × 1.4°	Centre National de Recherches Météorologiques and Centre Européen de Recherché et Formation Avancées en Calcul Scientifique, France
CSIRO Mk3.6	1.8° × 1.8°	Commonwealth Scientific and Industrial Research Organization with Queensland Climate Change Center of Excellence, Australia
EC-EARTH	1.121° ×1.125°	EC-EARTH Consortium, Europe
FGOALS	2.8° × 2.8°	
FIO-ESM	2.8° × 2.8°	First Institute of Oceanography, China
GFDL-ESM2M		
GFDL CM3	2°× 2.5°	NOAA/Geophysical Fluid Dynamic Laboratory, United States
GFDL-ESM2G	2°× 2°	NOAA/Geophysical Fluid Dynamic Laboratory, United States
GISS-E2-H-CC	2°× 2.5°	NASA Goddard Institute for Space Studies, United States
GISS-ES-R	2°× 2.5°	NASA Goddard Institute for Space Studies, United States
GISS-E2-R-CC	2°× 2.5°	NASA Goddard Institute for Space Studies, United States
HadGEM2-ES	1.25°× 1.875°	Met Office Hadley Centre, United Kingdom
HADGEM2-CC	1.25°× 1.875°	Met Office Hadley Centre, United Kingdom
INM-CM4.0	1.5° × 2°	Institute of Numerical Mathematics, Russian Academy of Sciences, Russia
IPSL-CM5A-LR	2°× 4°	Laboratoire de Météorologie Dynamique and L'Institut Pierre-Simon Laplace, France
IPSL-CM5A-MR		Laboratoire de Météorologie Dynamique and L'Institut Pierre-Simon Laplace, France
IPSL-CM5B-LR		Laboratoire de Météorologie Dynamique and L'Institut Pierre-Simon Laplace, France

Table 1. Continued

MIROC5	1.4° × 1.4°	Atmosphere and Ocean Research Institute, National Institute for Environmental Studies, and Japan Agency for Marine-Earth Science and Technology, Japan
MIROC-ESM	3°× 3°	Atmosphere and Ocean Research Institute, National Institute for Environmental Studies, and Japan Agency for Marine-Earth Science and Technology, Japan
MIROC-ESM-CHEM		Atmosphere and Ocean Research Institute, National Institute for Environmental Studies, and Japan Agency for Marine-Earth Science and Technology, Japan
MPI-ESM-LR	1.8° × 1.8°	Max Planck Institute for Meteorology, Germany
MPI-ESM-MR		Max Planck Institute for Meteorology, Germany
MRI-CGCM3	1°× 1°	Meteorological Research Institute, Japan Meteorological Agency, Japan
NorESM1-M	2°× 2°	Norwegian Climate Centre, Norway

3. Downscaling

In this research, using bias correction and spatial disaggregation (BCSD) method, downscaling process is performed. In the BCSD technique, biases are removed using the quantitative mapping method. This kind of method is compared the simulated climate values and observed values at specific points in the statistical distribution. It can adjust the simulated values to match the observed values well. The adjustment amount is recorded and applied well to future simulations. Then, adjusted simulations are downscaled to a finer-resolution spatial scale utilizing a linear interpolation method. The downscaling method calculates the values among adjusted data points to match smaller-scale resolution using surrounding data point values and linear relationships on the distance among large- and small-scale historical data point locations (*Jafarzadeh et al*., 2018). The monthly precipitation value of GCMs were obtained for historical periods from 1960 to 2005 and future periods from 2020 to 2100 from the CMIP5 Climate and Hydrology Projections website downscaled by the BCSD approach (*Schwalm et al.,* 2013). The monthly precipitation values were extracted for 4 points surrounding the studied station.

4. Performance criteria

By testing the downscaled outputs of GCM against historical precipitation, the best GCMs performance among historical periods for a study area was identified. To evaluate the accuracy of methods, the following seven criteria were used root mean square error (RMSE, Eq.(1)), mean absolute error (MAE, Eq.(2)), relative error percentage (RD, Eq.(3)), average relative error of months of the year (MRDM, Eq.(4)), relative average error of month per year (RDMM, Eq.(5)), percent of bias (PBIAS, Eq.(6)), RMSE-observations standard deviation ratio

(PSR, Eq.(7)), and Nash–Sutcliffe formula(NS, Eq.(8)) (*Lalehzari* and *Boroomand-Nasab*, 2017; *Fang et al.,* 2021; *Chen et al.,* 2021*; Miao et al.,* 2022; *Xu et al.,* 2022).

The seven criteria are formulated as follows:

$$RMSE = \sqrt{\frac{\sum_{i=1}^{n}(x_i^{obs}-x_i^{sim})^2}{n}}, \tag{1}$$

$$MAE = \frac{\sum_{i=1}^{n}\left|x_i^{obs}-x_i^{sim}\right|}{n}, \tag{2}$$

$$RD = \left|\frac{x_i^{obs}-x_i^{sim}}{x_i^{obs}}\right|, \tag{3}$$

$$MRDM = \frac{\sum_{i=1}^{n}\left|\frac{x_{i-mean}^{obs}-x_{i-mean}^{sim}}{x_{i-mean}^{obs}}\right|}{n}, \tag{4}$$

$$RDMM = \frac{\sum_{i=1}^{n}\left(\sum_{J=1}^{12} RD_J\right)_i}{n}, \tag{5}$$

$$PBIAS = \frac{\sum_{i=1}^{n} 100(X_i^{obs}-X_i^{sim})}{\sum_{i=1}^{n} X_i^{obs}}, \tag{6}$$

$$RSR = \frac{RMSE}{STDEV_{obs}} = \frac{\sqrt{\sum_{i=1}^{n}(X_i^{obs}-X_i^{sim})^2}}{\sqrt{\sum_{i=1}^{n}(X_i^{obs}-X_{i-mean}^{obs})^2}}. \tag{7}$$

$$NS = 1 - \frac{\sum_{i=1}^{n}(x_i-x_{obs})^2}{\sum_{i=1}^{n}(x_{obs}-\overline{x_{obs}})^2} \tag{8}$$

where x_i^{sim} are the predicted values by GCM models, x_i^{obs} are the measured values at the synoptic station, x_{i-mean}^{sim} is the average of predicted values by GCM models among the months of year, X_{i-mean}^{obs} is the average of measured values at the synoptic station among the months of year, RD_J is the relative error of the month in question, *n* is the number of models used in the research, and *J* is the number of the months of year.

5. Results

Since the selection of the future period in research strongly depends on the choice of the historical period, as in the methods of dynamic downscaling, the number of years of the historical period and the future period must be the same. Therefore, the requirement for choosing the right period is even more important for the historical period. Thus, 27 historical periods were selected for each of the 35 GCM models from long-term periods such as 1960–2005 to short-term ones such as 1995–2005. According to *Table 2*, the long-term historical periods such as 1960–2005 and 1960–2000 have a lower percentage of RMSE and MAE error compared to other periods, and the 1965–1990 historical period is among the periods with less than 30 years being in a good agreement with the precipitation data from the synoptic station. According to the PBIAS coefficient, which indicates the overestimation or underestimation of the observed value, the periods with less years produced higher overestimation. However, the period 1960–1990 that had lower PBIAS coefficient and RSR could be used as a suitable period. Also, in the Fifth Climate Change Report, the IPCC has selected the period 1985–2005 as the appropriate historical period. The period 1985–2005 can be a very good period to choose as a historical period due to the low relative error rate and PBIAS. Since the two periods of 1960–1985 and 1990–2005 have a lower PBIAS coefficient due to underestimation and overestimation compared to observed data, using only one error coefficient cannot indicate good results from that period and these periods had higher RSR coefficient compared to other periods. Table 3 shows more data matching the model and synoptic station in a longer historical period. Shorter historical periods such as 1970–1990 compared to 1975–2005 period had a lower error. The 1960–1995, 1960–2005 and 1960–2000 periods had lower relative error rates. There were periods such as 1960–1980, which had a lower average relative error of month (4.131), but they had a higher average of relative error (142.334). Therefore, both percentages of relative error must be considered.

Table 2. Percentage of error of different selected historical periods compared to the observation period

period	**Years number**	**RSR**	**PBIAS**	**RDMM**	**MRDM**	**MAE**	**RMSE**
1960–1999	40	0.032	4.104	34.233	4.306	-0.019	0.064
1965–2004	40	0.035	3.202	36.768	3.488	-0.015	0.068
1960–1989	30	0.058	2.548	33.969	4.021	-0.012	0.087
1970–1999	30	0.101	8.462	43.137	8.381	-0.033	0.113
1975–2004	30	0.086	6.393	40.973	6.673	-0.017	0.136
1965–1989	25	0.056	3.803	37.914	3.855	-0.018	0.085
1975–1999	25	0.118	9.686	44.445	9.188	-0.011	0.049
1980–2004	25	0.135	3.766	44.820	4.348	-0.048	0.171
1970–1989	20	0.086	5.135	41.639	6.638	-0.025	0.107
1980–1999	20	0.199	9.93	48.213	9.640	-0.036	0.162
1985–2004	20	0.195	2.034	47.682	3.877	-0.030	0.201

The results of climate change effects could be different due to multiple kinds of models. *Table 3* presents the models which bear the most similarity to the historical period or the lowest error percentage to daily precipitation data from the synoptic stations. According to this table, the NorESM1-M model was more consistent with the observational data than to other AOGCM models with the lowest RMSE value (RMSE = 0.091) and PBIAS value (PBIAS = 1.401). The GISS-E2-R model with low PBIAS value can be suitable model for precipitation research. The appropriate model can be selected based on the purpose and importance of research topic in the future.

Table 3. Determining the best model of the fifth report from comparing Birjand station data with precipitation data of climate change models

number	Model	R^2	NS	MAE	RMSE
1	NorESM1-M	0.971	0.959	0.007	0.091
2	HADGEM2-CC	0.981	0950	0.023	0.095
3	GFDL-ESM2G	0.974	0.941	0.015	0.098
4	GFDL-ESM2M	0.962	0.937	0.015	0.102
5	GISS-E2-R	0.955	0.937	0.008	0.106
6	MPI-ESM-LR	0.962	0.931	0.014	0.106
7	CANESM2	0.968	0.933	0.017	0.107
8	BNU-ESM	0.966	0.928	0.009	0.108
9	CSIROMK3.6	0.974	0.925	0.025	0.109
10	IPSL-CM5A	0.955	0.921	0.005	0.139
11	CANESM2	0.961	0.923	-0.024	0.140
12	MPI-ESM-LR	0.955	0.921	-0.016	0.140
13	CMCC-CM	0.973	0.922	-0.056	0.141
14	CNRM-CM5	0.966	0.916	-0.016	0.142
15	MRI-CGCM3	0.940	0.918	-0.024	0.143
16	GISS-E2-R-CC	0.951	0.913	-0.016	0.147
17	CESM1-CAM5	0.961	0.899	-0.054	0.156
18	inmcm4	0.959	0.904	-0.013	0.156
19	GISS-E2-H-CC	0.939	0.903	-0.035	0.157
20	BCC-CSM1-M	0.966	0.899	-0.040	0.159
21	CESM1-BGC	0.947	0.896	-0.007	0.160
22	MIROC5	0.958	0.895	-0.043	0.163
23	IPSL-CM5B	0.954	0.891	-0.031	0.164
24	GFDL-CM3-PR	0.942	0.882	-0.038	0.170
25	MIROC-ESM	0.934	0.867	-0.057	0.172
26	FGOALS	0.948	0.883	-0.038	0.172

Table 3. Continued

number	Model	R^2	NS	MAE	RMSE
27	FIO-ESM	0.920	0.872	-0.005	0.174
28	CCSM4	0.963	0.883	-0.078	0.174
29	IPSL	0.949	0.878	-0.050	0.176
30	ACCESS1	0.932	0.874	-0.009	0.176
31	MIROC-ESM-CHEM	0.952	0.878	-0.025	0.182
32	HADCM3	0.905	0.964	-0.018	0.183
33	BCC-CSM1-1	0.911	0.838	-0.037	0.198
34	HADGEM2	0.910	0.837	-0.007	0.201
31	MIROC-ESM-CHEM	0.952	0.878	-0.025	0.182
32	HADCM3	0.905	0.964	-0.018	0.183
33	BCC-CSM1-1	0.911	0.838	-0.037	0.198
34	HADGEM2	0.910	0.837	-0.007	0.201

Fig. 2 shows the growth ratio from the future periods to the historical period for two scenarios of RCP 4.5 and RCP 8.5 in different AOGCM models. This figure shows that different models had different precipitation estimations in future periods than to the historical period. For the RCP 4.5 scenario, CESM1-CAM5 and ACCESS1-3 models showed the largest changes, and the IPSL model the lowest changes in the estimation of the precipitation changes for the next period. For the RCP 8.5 scenario, CANEM2 and CESM1-CAM5 models showed the most changes, and IPSL-CM5A-LR and FGOALS-S2 models showed the lowest changes. Model changes for future periods in the RCP 4.5 scenario reached a maximum of 1.1 in the value of the growth ratio in the historical period, while these changes in the RCP 8.5 scenario in some models reached 1.45 in the historical period in some models.

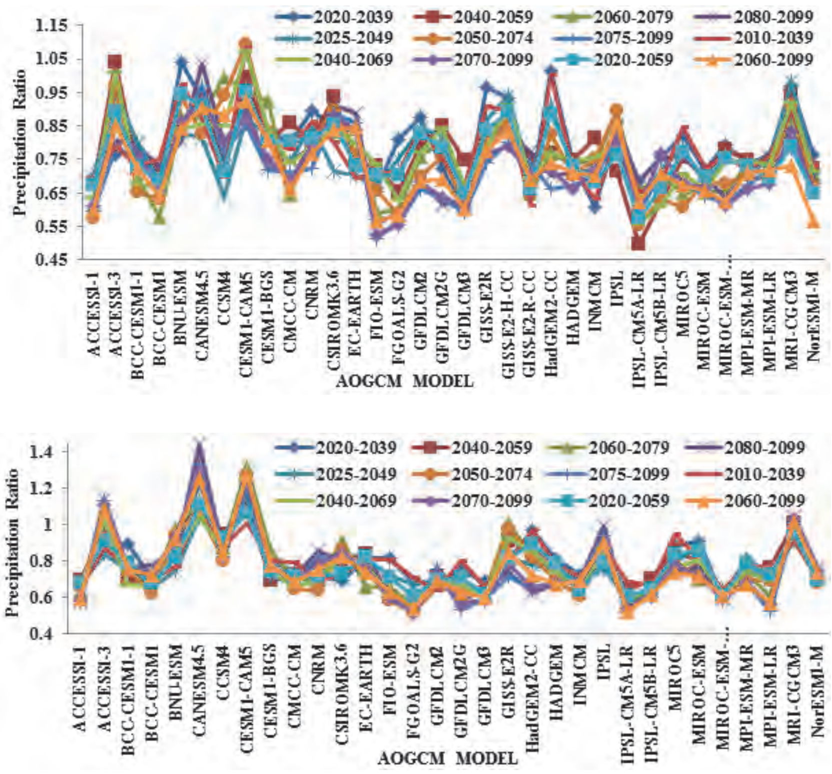

Fig. 2. Precipitation ratios of future periods to historical period for the RCP 4.5 (upper panel) and RCP 8.5 (lower panel) scenarios for different AOGCM models.

There are many differences between historical periods with different time intervals. There was a significant difference due to rainfall by choosing different historical periods with several time series in the future. Considering a historical period with more number of years leads to a decrease in the annual rainfall over time. Until 2100 AD, the annual amount of precipitation values for different historical periods vary from 165 mm for 20-year-long periods to 158 mm for the 25- and 30-year-long periods (*Fig. 3*). These changes in the RCP 8.5 scenario ranged from 163 to 151 mm. More accurate forecast in the future will be expected with lower historical periods by several years. For example, the historical period with 25 and 30 years easily indicate changes in the precipitation up to 2100 AD. The overall results showed more changes in the RCP 8.5 scenario than in the RCP 4.5 scenario. Scenario RCP 8.5 showed changes of about 153 mm, while scenario RCP 4.5 showed 158 mm. *Farzaneh et al.* (2012) and *Singh et al.* (2019) showed that in the 1951–2100 period, there was a high variation in precipitation.

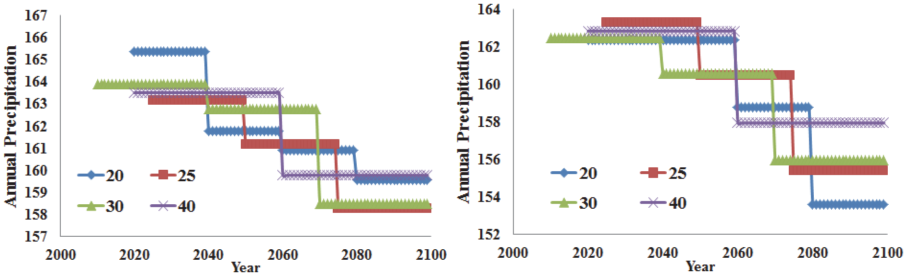

Fig. 3. The effect of the length of the historical period on annual precipitation changes 2100 AD for the RCP 4.5 (left) and RCP 8.5 (right) scenarios.

Fig. 4 shows the changes in future periods compared to the historical periods. These graphs show the effect of selecting incorrect of the historical period on changes in future periods. According to the *Fig. 4*, the historical periods 1980–2000 and 1985–2005 have the lowest changes in RCP 4.5 and RCP 8.5 scenarios compared to periods with the other 20 years. In the case of the 25-year-long historical periods and the RCP 4.5 scenario, the changes in the future period of precipitation value compared to the historical period 1975–2000 periods was lower than other historical periods, while the RCP 8.5 scenario for the 1980–2005 period had the lowest changes in precipitation value than other periods. For precipitation changes in the future periods with 30 years, the changes in the historical period 1975–2005 were lower than the other two periods (30 years) for RCP 4.5 and RCP 8.5 scenarios. The changes of RCP 4.5 scenario were also less than the RCP 8.5 scenario which shows more certainty of the results of this scenario. Regarding changes in the next 40-year-long periods, the 1960–2000 historical period had a smaller range of changes than the 1965–2005 period, and it might be due to the increased rainfall in the period of 2005 compared to the period of 2000. Also, these graphs show that the range of changes distant future years for all graphs has been less than in near future. It shows a decrease in precipitation in the late 21st century for the studied region.

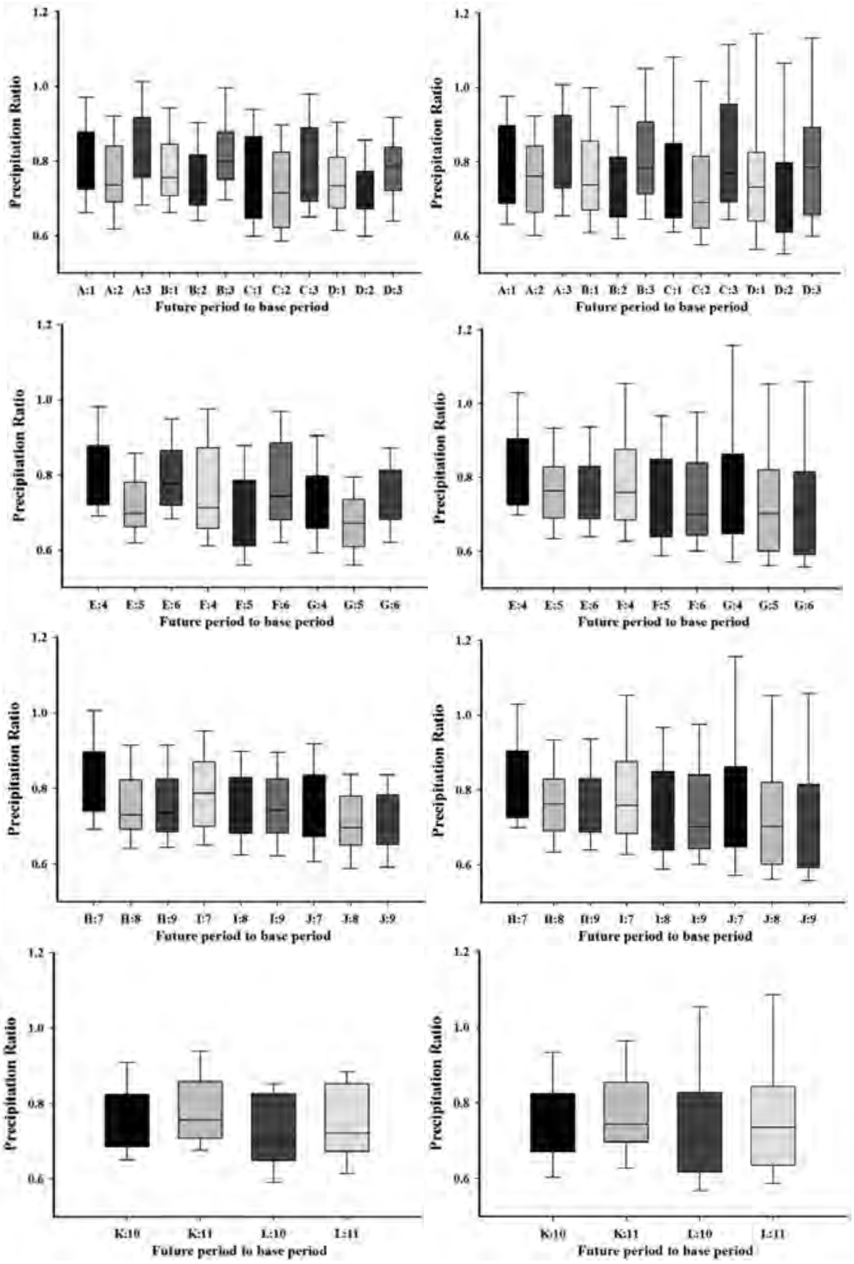

Fig. 4 Changes in the ratio of the annual rainfall in the future periods (2020-2039: A, 2040-2059: B, 2060-2079: C, 2080-2099: D, 2025-2049: E, 2050-2074: F, 2075-2099: G, 2010-2039: H, 2040-2069: I, 2070-2099: J, 2020-2059: K, 2060-2099: L) to the historical period (1970-1990: 1, 1980-2000: 2, 1985-2005: 3,1965-1990: 4, 1975-2000: 5, 1980-2005: 6, 1960-1990: 7, 1970-2000: 8, 1975-2005: 9, 1960-2000: 10, 1965-2005) for the scenario RCP4.5 (left) and RCP8.5 (right).

Fig. 5 shows the range of annual rainfall changes in different GCM models from 2020 to 2100 AD for the two scenarios (RCP 4.5 and RCP 8.5). The results of scenario RCP 4.5 showed that MPI-ESM-MR and HADGEM models had the lowest range of precipitation changes by 2100. Both models had estimated precipitation about 160 mm by 2100. Most models had rainfall estimation of about 170 mm. Among the models, FIO-ESM, FGOALS-G2, and MIROC-ESM-CHEM models had a rainfall estimation of about 130 mm, and BNU-ESM and MRI-CGCM3 models estimated a rainfall from 190 to 200 mm for the studied station by 2100. The results of scenario 8.5 showed that IPSL-CM5B-LR and CANESM2 models would have the lowest and highest precipitation changes by 2100, respectively. CANESM2 and FGOALS-G2 models had the highest (about 265 mm) and the lowest (85 mm per year) annual rainfall estimations, respectively. The results of rainfall changes in scenario RCP 8.5 showed that all models estimated an average of about 150 mm from rainfall per year up to 2100 AD.

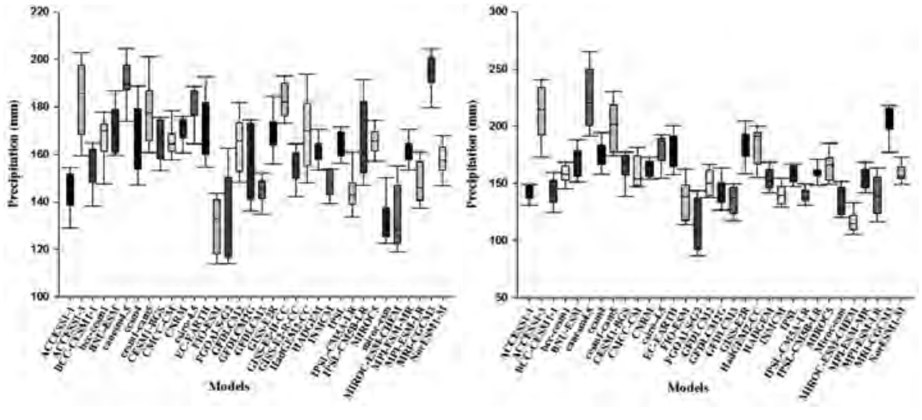

Fig. 5. Box diagrams of precipitation changes of GCM models during the years 2020 to 2100 AD for the scenario RCP4.5 (left) and RCP8.5 (right).

6. Conclusion

Selecting the suitable climate models and historical periods for predicting the future rainfall variations compared to the previous periods could be an important analysis technique. This may be due to different GCM models and historical periods and their impact on research results. Therefore, a comparison was made between 35 GCM models and 27 selected historical periods from long-term period's like1960–2005 to short-term ones like the 1995–2005 period. The results showed that long-term historical periods such as 1960–2005 and 1960–2000 have lower RMSE and MAE error rates than other periods. Furthermore, the historical period 1965–1990 was among periods under 30 years and it was in good agreement with the precipitation data from the synoptic stations. Periods with less years were overestimated. Nevertheless, the 1960–1990 period had lower PBIAS and RSR coefficients than that could be used as a suitable period. The proposed period of 1985–2005 from the IPCC can also be a suitable period to choose as a historical period considering the low relative error rate and PBIAS. The results showed that with longer historical period, there was more agreement between model precipitation data and synoptic stations. The results of climate change effects could be varied based on the different models. The NorESM1-M model was more consistent with the observational data than other AOGCM models with the lowest RMSE and PBIAS values. The GISS-E2-R model with low PBIAS value can be a suitable model for rainfall estimation. Depending on the purpose and importance of research topic in the future, a suitable model should be selected. Different models had several estimates of precipitation in the future periods compared to the historical period. In the RCP 4.5 scenario, CESM1-CAM5 and ACCESS1-3 models had the biggest changes and IPSL models had the lowest estimate for precipitation changes for the future periods. For the RCP 8.5 scenario, CANEM2 and CESM1-CAM5 models had the biggest changes, and IPSL-CM5A-LR and FGOALS-S2 models had the smallest changes. Model changes for the future periods in the RCP 4.5 scenario have reached a maximum of 1/1 of the historical periods, while these ratios have reached 1.45 in the RCP 8.5 scenario in some models.

References

Adebayo, T.S., Awosusi, A.A., Odugbesan, J.A., Akinsola, G.D., Wong, W.K., and *Rjoub, H.,* 2021a: Sustainability of energy-induced growth nexus in Brazil: do carbon emissions and urbanization matter? *Sustainability 13*(8), 4371. https://doi.org/10.3390/su13084371

Adebayo, T.S., Coelho, M.F., Onbaşıoğlu, D.Ç., Rjoub, H., Mata, M.N., Carvalho, P.V., and *Adeshola, I.* 2021b: Modeling the dynamic linkage between renewable energy consumption, globalization, and environmental degradation in South Korea: does technological innovation matter?. *Energies 14*(14), 4265. https://doi.org/10.3390/en14144265

Adebayo, T.S., Rjoub, H., Akinsola, G.D., and *Oladipupo, S.D.,* 2022: The asymmetric effects of renewable energy consumption and trade openness on carbon emissions in Sweden: new evidence from quantile-on-quantile regression approach. *Environ. Sci. Pollut. Res. 29*, 1875–1886. https://doi.org/10.1007/s11356-021-15706-4

Afshar, A., Khosravi, M., and *Molajou, A.,* 2021: Assessing adaptability of cyclic and non-cyclic approach to conjunctive use of groundwater and surface water for sustainable management plans under climate change. *Water Resour. Manage. 35*, 3463–3479. https://doi.org/10.1007/s11269-021-02887-3

Ahmed, Z., Ahmad, M., Rjoub, H., Kalugina, O.A., and *Hussain, N.,* 2021: Economic growth, renewable energy consumption, and ecological footprint: Exploring the role of environmental regulations and democracy in sustainable development. *Sust. Develop*. https://doi.org/10.1002/sd.2251

Alvankar, S.R., Nazari, F., and *Fattahi, E.* 2016: The Intensity and Return Periods of Drought under Future Climate Change Scenarios in Iran. *J. Spatial Anal. Environ. 3*, 99–120. https://doi.org/10.18869/acadpub.jsaeh.3.2.99

Chen, X., Quan, Q., Zhang, K., and *Wei, J.,* 2021: Spatiotemporal characteristics and attribution of dry/wet conditions in the Weihe River Basin within a typical monsoon transition zone of East Asia over the recent 547 years. *Environ. Model. Software. 143,* 105116. https://doi.org/10.1016/j.envsoft.2021.105116

Chen, Z., Liu, Z., Yin, L., and *Zheng, W.,* 2022: Statistical analysis of regional air temperature characteristics before and after dam construction. *Urban Climate 41*. https://doi.org/10.1016/j.uclim.2022.101085

D'Agata, C., Diolaiuti, G., Maragno, D., Smiraglia, C., and *Pelfini, M.,* 2020:) Climate change effects on landscape and environment in glacier zed Alpine areas: retreating glaciers and enlarging forelands in the Bernina group (Italy) in the period 1954–2007. *Geol. Ecol. Landscapes 4*, 71–86. https://doi.org/10.1080/24749508.2019.1585658

Fang, X., Wang, Q., Wang, J., Xiang, Y., Wu, Y., and *Zhang, Y.,* 2021: Employing extreme value theory to establish nutrient criteria in bay waters: A case study of Xiangshan Bay. *J. Hydrol. 603*, 127146. https://doi.org/10.1016/j.jhydrol.2021.127146

Farzaneh, M.R., Eslamian, E., Samadi, S.Z., and *Akbarpour, A.,* 2012: An appropriate general circulation model (GCM) to investigate climate change impact. *Int. J. Hydrol. Sci. Technol. 2,* 34–47. https://doi.org/10.1504/IJHST.2012.045938

F*ung, C.F., Lopez, A.,* and *New, M.,* 2011: Modelling the impact of climate change on water resources. John Wiley & Sons. https://doi.org/10.1002/9781444324921

Gholamin, R. and *Khayatnezhad, M.,* 2021: Impacts of PEG-6000-induced drought stress on Chlorophyll content, relative water content (RWC), and RNA content of peanut (Arachis hypogaea L.) roots and leaves. *Biosci. Res. 18*, 393–402.

Gholamin, R. and *Khayatnezhad, M.,* 2020: The Effect of Dry Season Stretch on Chlorophyll Content and RWC of Wheat Genotypes (Triticum Durum L.). *Biosci. Biotech. Res. Comm. 13*(4).

Godage, R.S.W., Gajanayake, B., and *Jayasinghe-Mudalige, U.K.,* 2021: Coconut Growers Knowledge, Perception and Adoption on Impacts of Climate Change in Gampaha and Puttalam Districts in Sri Lanka: An Index-Based Approach. Current Research in Agricultural Sciences, 8(2), 97–109.

Gregory, J.M., Church, J.A., Boer, G.J., Dixon, K.W., Flato, G.M., Jackett, D.R., Lowe, J.A., Farrell, S.P., Roeckner, E., Russell, G.L., Stouffer, R.J., and *Winton, M.,* 2001: Comparison of results from several AOGCMs for global and regional sea-level change 1900–2100. *Climate Dynam. 18,* 225–240. https://doi.org/10.1007/s003820100180

Guo, L.N., She, C., Kong, D.B., Yan, S.L., Xu, Y.P., Khayatnezhad, M., and *Gholinia, F.,* 2021: Prediction of the effects of climate change on hydroelectric generation, electricity demand, and emissions of greenhouse gases under climatic scenarios and optimized ANN model. *Energy Rep. 7*, 5431–5445.

Hou, R., Li, S., Wu, M., Ren, G., Gao, W., Khayatnezhad, M., and *Gholinia, F*., 2021: Assessing of impact climate parameters on the gap between hydropower supply and electricity demand by RCPs scenarios and optimized ANN by the improved Pathfinder (IPF) algorithm. *Energy 237*, 121621.

Huang, D., Wang, J., and *Khayatnezhad, M.* 2021: Estimation of actual evapotranspiration using soil moisture balance and remote sensing. *Iranian J. Sci. Technol. Transact. Civil Engin. 45,* 2779–2786. https://doi.org/10.1007/s40996-020-00575-7

IPCC, 2007: The physical science basis. In: (Eds. *Solomon, S., Qin, D., Manning, M., Chen, Z., Marquis, M., Averyt, K., Tignor, M., Miller, H.*), Contribution of Working Group I to the Fourth Assessment Report of the Intergovernmental Panel on Climate Change. Cambridge University Press, Cambridge, UK.

IPCC, 2013: The physical science basis. In: (Eds. *Stocker, T.F., Qin, D., Plattner, G.K., Tignor, M., Allen, S.K., Boschung, J., Nauels, A., Xia, Y., Bex, V., Midgley, P.M.*), Contribution of Working Group I to the Fifth Assessment Report of the Intergovernmental Panel on Climate Change. Cambridge University Press, Cambridge.

Jafarzadeh, A., Pourreza-Bilondi, M., Aghakhani Afshar, A.H., Khashei-Siuki, A., and *Yaghoobzadeh, M.,* 2018: Estimating the reliability of a rainwater catchment system using the output data of general circulation models for the future period (case study: Birjand City, Iran). *Theor. Appl. Climatol. 137*, 1975-1986. https://doi.org/10.1007/s00704-018-2714-z.

Kamal, A. and *Massah Bavani, A.*, 2012: Comparison of future uncertainty of AOGCM-TAR and AOGCM-AR4 models in the projection of runoff basin. *J. Earth Space Phys. 38*,175–188.

Karasakal, A., Khayatnezhad, M., and *Gholamin, R.,* 2020a: The durum wheat gene sequence response assessment of Triticum durum for dehydration situations utilizing different indicators of water deficiency. *Biosc. Biotech. Res. Comm. 13*, 2050–2057. https://doi.org/10.21786/bbrc/13.4/62

Karasakal, A., Khayatnezhad, M., and *Gholamin, R.,* 2020b: The effect of saline, drought, and Presowing Salt Stress on Nitrate Reductase Activity in Varieties of Eleusine coracana (Gaertn). *Biosc. Biotech. Res. Comm. 13,* 2087–2091. https://doi.org/10.21786/bbrc/13.4/68

Kong, Q., 2020: The dilemma and way of fighting climate change in coastal areas in China in the view of ecological justice. *J. Coastal Res., 103(sp1)*, 500–505. https://doi.org/10.2112/SI103-101.1

Kouhestani, S.H., Eslamian, S.S., Abedi-Koupai, J., and *Besalatpour, A.A.,* 2016: Projection of climate change impacts on precipitation using soft-computing techniques: A case study in Zayandeh-rud Basin, Iran. *Glob. Planet. Change 144*:158–170. https://doi.org/10.1016/j.gloplacha.2016.07.013

Lalehzari, R. and *Boroomand-Nasab, S.* 2017: Improved volume balance using upstream flow depth for advance time estimation. *Agric. Water Manage. 186,* 120–126. https://doi.org/10.1016/j.agwat.2017.03.005

Li, A., Mu, X., Zhao, X., Xu, J., Khayatnezhad, M., and *Lalehzari, R.,* 2021a: Developing the non-dimensional framework for water distribution formulation to evaluate sprinkler irrigation. *Irrigat. Drainage 70,* 659–667. https://doi.org/10.1002/ird.2568 https://doi.org/10.1002/ird.2568

Li, X, Zhang, K., Gu, P., Feng, H., Yin, Y., Chen, W., and *Cheng, B.,* 2021b: Changes in precipitation extremes in the Yangtze River Basin during 1960–2019 and the association with global warming, ENSO, and local effects. *Sci. Total Environ. 760*, 144244. https://doi.org/10.1016/j.scitotenv.2020.144244

Lin, X., Zhao, Y., Ahmad, M., Ahmed, Z., Rjoub, H., and *Adebayo, T.S.,* 2021: Linking innovative human capital, economic growth, and CO2 emissions: an empirical study based on Chinese provincial panel data. *Int. J. Environ. Res. Public Health 18*(16), 8503. https://doi.org/10.3390/ijerph18168503

Ma, A., Ji, J., and *Khayatnezhad, M.,* 2021: Risk-constrained non-probabilistic scheduling of coordinated power-to-gas conversion facility and natural gas storage in power and gas based energy systems. *Sust. Energy, Grids Networks 26*:100478. https://doi.org/10.1016/j.segan.2021.100478

Mahmood, G.G., Rashid, H., Anwar, S., and *Nasir, A.* 2019: Evaluation of climate change impacts on rainfall patterns in Pothohar region of Pakistan. *Water Conservat. Manage. 3*, 1–6. https://doi.org/10.26480/wcm.01.2019.01.06

Miao, R., Liu, Y., Wu, L., Wang, D., Liu, Y., Miao, Y., and *Ma, J.,* 2022: Effects of long-term grazing exclusion on plant and soil properties vary with position in dune systems in the Horqin Sandy Land. *Catena* (IF5.198). https://doi.org/10.1016/j.catena.2021.105860

Mogano, P. and *Mokoele, N.,* 2019: South African Climate Change Adaptation Politics: Urban Governance Prospects *Int. J. Social Sci. Humanity Studies 11*, 68–83.

Mousavi, S.S., Karandish, F., and *Tabari, H.,* 2016: Temporal and spatial variation of rainfall in Iran under climate changes until 2100. *Irrig. Water Engin. J. 25*,152–165.

Nabipour, N., Mosavi, A., Hajnal, E., Nadai, L., Shamshirband, S., and *Chau, K.W.* 2020: Modeling climate change impact on wind power resources using adaptive neuro-fuzzy inference system. *Engineer. Appl. Computat. Fluid Mech. 14*, 491–506. https://doi.org/10.1080/19942060.2020.1722241

Nourani, V., Razzaghzadeh, Z., Baghanam, A.H., and *Molajou, A.,* 2019: ANN-based statistical downscaling of climatic parameters using decision tree predictor screening method. *Theor. Appl. Climatol. 137*, 1729–1746. https://doi.org/10.1007/s00704-018-2686-z

Nourani, V., Rouzegari, N., Molajou, A., and *Baghanam, A.H.,* 2020: An integrated simulation-optimization framework to optimize the reservoir operation adapted to climate change scenarios. *J. Hydrol. 587*, 125018. https://doi.org/10.1016/j.jhydrol.2020.125018

Odugbesan, J.A. and *Rjoub, H.,* 2020: Relationship among economic growth, energy consumption, CO2 emission, and urbanization: evidence from MINT countries. *Sage Open 10*(2), 2158244020914648. https://doi.org/10.1177/2158244020914648

Oladipupo, S.D,, Rjoub, H., Kirikkaleli, D., and *Adebayo, T.S.* 2022: Impact of Globalization and Renewable Energy Consumption on Environmental Degradation: A Lesson for South Africa. International *J. Renew. Energy Develop. 11*, 145–155. https://doi.org/10.14710/ijred.2022.40452

Oseke, F.I.E., Anornu, G.K., Adjei, K.A., and *Eduvie, M.O.,* 2021: Predicting the impact of climate change and the hydrological response within the Gurara reservoir catchment, Nigeria. *J. Water Land Develop. 51*, 129–143.

Parracho, A.C., Melo-Gonçalves, P., and *Rocha, A.*, 2016: Regionalization of precipitation for the Iberian Peninsula and climate change. *Phys. Chem. Earth, Parts A/B/C 94*,146–154. https://doi.org/10.1016/j.pce.2015.07.004

Quan, Q., Liang, W., Yan, D., and *Lei, J.*, 2022: Influences of joint action of natural and social factors on atmospheric process of hydrological cycle in Inner Mongolia, China. *Urban Climate 41*, 101043. doi: 10.1016/j.uclim.2021.101043

Rahman, M.M. and *Islam, I.* 2020: Exposure of urban infrastructure because of climate change-induced flood: lesson from municipal level planning in Bangladesh. *Ecofeminism Climate Change* 1(3), 107–125. https://doi.org/10.1108/EFCC-05-2020-0011

Ren, J. and *Khayatnezhad, M.,* 2021: Evaluating the storm water management model to improve urban water allocation system in drought conditions. *Water Supply 21,* 1514–1524. https://doi.org/10.2166/ws.2021.027

Rjoub, H., Odugbesan, J.A., Adebayo. T.S., Wong, W.K. 2021: Sustainability of the moderating role of financial development in the determinants of environmental degradation: evidence from Turkey. *Sustainability 13*(4), 1844.

Samadi, S.Z., Sagareswar, G., and *Tajiki, M.,* 2010: Comparison of General Circulation Models: methodology for selecting the best GCM in Kermanshah Synoptic Station, Iran. *Int. J. Global Warming 2*, 347–365. https://doi.org/10.1504/IJGW.2010.037590

Schwalm, C.R., Huntinzger, D.N., Michalak, A.M., Fisher, J.B., Kimball, J.S., Mueller, B., and *Zhang, Y.,* 2013: Sensitivity of inferred climate model skill to evaluation decisions: a case study using CMIP5 evapotranspiration. *Environ. Res. Lett. 8*(2), 24028. doi: 10.1088/1748-9326/8/2/024028

Shen, M., Chen, J., Zhuan, M., Hua Chen, H., Xu, C.H., and *Xiong, L.,* 2018: Estimating uncertainty and its temporal variation related to global climate models in quantifying climate change impacts on hydrology. *J. Hydrol. 556*, 10–24.

Sibuea, M.B., Sibuea, S.R., and *Pratama, I.,* 2021: The impact of renewable energy and economic development on environmental quality of ASEAN countries. *AgBioForum 23*(1), 12–21.

Singh, V., Jain, S.K., and *Singh, P.K.,* 2019: Inter-comparisons and applicability of CMIP5 GCMs, RCMs and statistically downscaled NEX-GDDP based preci134-pitation in India. *Sci. Total Environ. 697*,134–163.

Sobhani, B., Eslahi, M., and *Babaeian, I.,* 2017: Comparison of statistical downscaling in climate change models to simulate climate elements in Northwest Iran. *Phys. Geograp. Res. 49*, 301–325.

Sun, Q., Lin, D., Khayatnezhad, M., Taghavi, M., 2021: Investigation of phosphoric acid fuel cell, linear Fresnel solar reflector and organic ranking cycle polygene ration energy system in different climatic conditions. *Proc. Safety Environ. Protect. 147*, 993–1008.

Sun, X. and *Khayatnezhad, M.* 2021: Fuzzy-probabilistic modeling the flood characteristics using bivariate frequency analysis and α-cut decomposition. *Water Supply 21*, 4391–4403. https://doi.org/10.2166/ws.2021.186

Tangonyire, D.F., 2019: Impact of climate change on farmers in the Talensi District of the upper east region of Ghana. *Malaysian J. Sustain. Agricult. 3*(2), 35–45.

Tao, Z., Cui, Z., Yu, J., and *Khayatnezhad, M.,* 2022: Finite difference modeling of groundwater flow for constructing artificial recharge structures. *Iranian J. Sci. Technol. Transact. Civil Engin*. 46, 1503-1514. https://doi.org/10.1007/s40996-021-00698-5

Wang, C., Shang, Y., and *Khayatnezhad, M.,* 2021: Fuzzy stress-based modeling for probabilistic irrigation planning using Copula-NSPSO. *Water Res. Manage.* 35, 4943–4959. https://doi.org/10.1007/s11269-021-02981-6

Wang, H., Khayatnezhad, M., and *Youssefi, N.,* 2022: Using an optimized soil and water assessment tool by deep belief networks to evaluate the impact of land use and climate change on water resources. *Concur. Comput. 34*, e6807. https://doi.org/10.1002/cpe.6807

Weinberger, K.R., Haykin, L., Eliot, M.N., Schwartz, J.D., Gasparrini, A., and *Wellenius, G.A.,* 2017: Projected temperature-related deaths in ten large U.S metropolitan areas under different climate change scenarios. *Environ. Int. 107*,196–204. https://doi.org/10.1016/j.envint.2017.07.006

Xu, J., Zhou, L., Hu, K., Li, Y., Zhou, X., and *Wang, S.,* 2022: Influence of wet-dry cycles on uniaxial compression behavior of fissured loess disturbed by vibratory loads. *KSCE J. Civil Engineer. 26*, 2139–2152. https://doi.org/10.1007/s12205-022-1593-0

Xu, Y.P., Ouyang, P., Xing, S.M., Qi, L.Y., Khayatnezhad, M., and *Jafari, H.,* 2021: Optimal structure design of a PV/FC HRES using amended Water Strider Algorithm. *Energy Rep. 7*, 2057–2067. https://doi.org/10.1016/j.egyr.2021.04.016

Yaghoobzadeh, M., Ahmadi, M., Seyyed Kaboli, H., Zamani, Gh.R., and *Amirabadizadeh, M.,* 2017*:* The Evaluation Of Effect Of Climate Change On Agricultural Drought Using ETDI And SPI Indexes. *J. Water Soil Convers. 24*(4), 43–61.

Yin, L., Wang, L., Keim, B.D., Konsoer, K., and *Zheng, W.,* 2022a: Wavelet analysis of dam injection and discharge in three gorges dam and reservoir with precipitation and river discharge. *Water 14*(4), 567. https://doi.org/10.3390/w14040567

Yin, L., Wang, L., Zheng, W., Ge, L., Tian, J., Liu, Y., and *Liu, S.* 2022b: Evaluation of empirical atmospheric models using swarm-C satellite data. *Atmosphere 13*(2), 294. https://doi.org/10.3390/atmos13020294

Zhang, H., Khayatnezhad, M., and *Davarpanah, A.,* 2021: Experimental investigation on the application of carbon dioxide adsorption for a shale reservoir. *Energ. Sci. Engin. 9*, 2165–2176. https://doi.org/10.1002/ese3.938

Zhang, L., Nan, Z., Yud, W., Zhao, Y., and *Xu. Y. 2018:* Comparison of baseline period choices for separating climate and land use/land cover change impacts on watershed hydrology using distributed hydrological models. *Sci. Total Environ*. 622–623, 1016–1028.

Zhang, K., Wang, S., Bao, H., and *Zhao, X.,* 2019: Characteristics and influencing factors of rainfall-induced landslide and debris flow hazards in Shaanxi Province, China. *Nat. Hazards Earth Syst. Sci. 19*(1), 93–105. https://doi.org/10.5194/nhess-19-93-2019

Zhao, X., Xia, H., Pan, L., Song, H., Niu, W., Wang, R., and *Qin, Y.,* 2021: Drought monitoring over Yellow River Basin from 2003–2019 using reconstructed MODIS Land Surface Temperature in google earth engine. *Remote sens. 13*(18), 3748. https://doi.org/10.1002/ese3.938

Zhu, P., Saadat,i H., Khayatnezhad, M., 2021: Application of probability decision system and particle swarm optimization for improving soil moisture content. *Water Supply. 21*, 4145–4152. https://doi.org/10.2166/ws.2021.169

DOI:10.28974/idojaras.2022.2.6

IDŐJÁRÁS

Quarterly Journal of the Hungarian Meteorological Service
Vol. 126, No. 2, April – June, 2022, pp. 267–284

Mean annual totals of precipitation during the period 1991–2015 with respect to cyclonic situations in Slovakia

Jakub Mészáros*[,1], **Martin Halaj**[2], **Norbert Polčák**[3], and **Milan Onderka**[4]

[1]*Institute of Hydrology*
Slovak Academy of Sciences
Dúbravská cesta 9, 841 04 Bratislava, Slovakia

[2] *Slovak Hydrometeorological Institute*
Zelená 5, 974 04 Banská Bystrica, Slovakia

[3] *Slovak Hydrometeorological Institute*
Jeséniova 17, 833 15 Bratislava, Slovakia

[4]*Earth Science Institute of the Slovak Academy of Sciences*
Dúbravská cesta 9, 840 05 Bratislava, Slovakia

** Corresponding Author e-mail: hydrjaku@savba.sk*

(Manuscript received in final form February 4, 2021)

Abstract— Atmospheric precipitation during cyclonic situations was analyzed using weather types classification. Based on data from the period 1991 to 2015, the observed cyclonic situations were analyzed in terms of their frequency of days with a given weather type. Cyclonic situations with airflow direction from the west and northwest, north and northeast, east and southeast, and south and southwest were analyzed. We identified a declining number of days that can be classified as cyclonic situations. The distributions of the mean annual precipitation totals for these cyclonic situations have been investigated. The highest mean annual precipitation totals occurred during the west cyclonic, northeast cyclonic, and east cyclonic weather types. The lowest mean annual precipitation totals were identified during the southwest cyclonic (with fronts moving from north to northeast) and north cyclonic weather types. The percentage of the individual cyclonic weather types and supertypes in the mean annual precipitation total was calculated. The directional supertype west + northwest with the west cyclonic type occurred with the highest percentage, although variations may arise due to windward and leeward effects.

Key-words: atmospheric precipitation, cyclonic situations, mean precipitation totals, Carpathian Mountains, Pannonian Plain

1. Introduction

The landscape can be supplied with water from the oceans and seas, glaciers, groundwater aquifers, or rivers. Central Europe is an inland region, and although glaciers have been more prevalent here in the past, the main source of water now are aquifers and rivers, which are formed by atmospheric precipitation. Because water is important for all forms of life, its resources require special attention. Here we focused on water from atmospheric precipitation and its distribution. Although the region of Central Europe is not physically surrounded by oceans, precipitation falls mostly during westerly and northwesterly cyclonic situations originating in the Atlantic Ocean, but occasionally also from cyclonic situations from the Mediterranean or the Black Sea.

Slovakia is a country with a wide range of altitudes varying from 94 m a.s.l. up to 2655 m a.s.l. The ridges of the Western and partly also the Eastern Carpathians stretch from west to east forming a significant barrier to the arriving air masses. The southwest and southeast parts of the country are mostly lowlands and are part of the Pannonian Basin (*Fig. 1*). In terms of the Köppen climate classification, the territory of Slovakia is a continental climate region with dry winters and warm summers. The climate is characterized by regular alternation of four seasons and variable weather, affected by pressure centers located in the Azores High and Icelandic Low. In Slovakia, the prevailing westerly winds and the relief enhance precipitation totals on windward slopes, causing the highest annual precipitation totals exceeding 1200 mm (occasionally even more than 1500 mm) in the mountainous northern region. The lowest precipitation totals of 550 mm per year are observed in lowlands and about 650 mm in depressions located in rain shadows of the surrounding mountains (*Fig. 2*). Precipitation is unevenly distributed throughout the year, some 40% of precipitation falls in summer, 25% in the spring, 20% in the autumn, and 15% in the winter (*SHMÚ*, 2009).

Fig. 1. Location and relief of Slovakia.

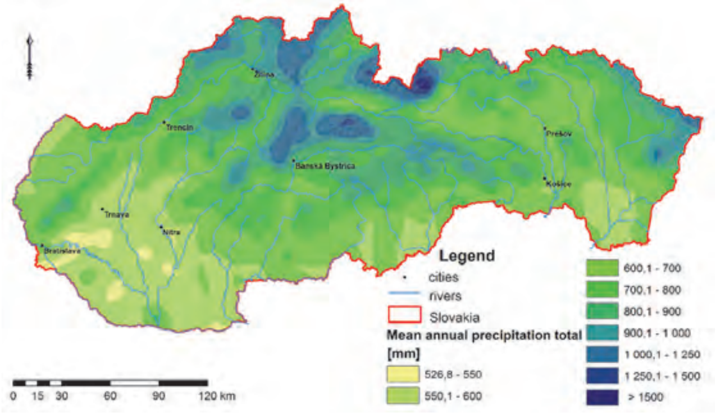

Fig. 2. Mean annual precipitation totals in Slovakia for the period 1991–2015.

In this paper, we deal with cyclonic situations that bring precipitation to the territory of Slovakia and are related to various directions of airflow. Our goal is to identify areas in Slovakia that are the most and the least affected by these cyclonic situations. These findings can improve our knowledge of the currently highly debated topic: the climate change. Although, it must be admitted that even a 25-year period may not be sufficiently long from climate change perspective, the analyses described herein can improve our knowledge about, e.g., circulation trends or intensity of precipitation. It is also important to know how the occurrence of weather types changes throughout the year. This can explain the temporal evolution of mean annual precipitation totals.

2. Materials and methods

Precipitation was measured within the network of precipitation gauges in Slovakia. Daily (24-hour) precipitation totals were registered only on days when precipitation exceeded 0.1 mm (the lowest total registered by the gauge). The analyzed precipitation data cover the period between 1991 and 2015. There are various schemes that can be applied in the classification of weather types in the region of Central Europe. The best known is the "Katalog der Grosswetterlagen Europas" (*Hess* and *Brezowsky*, 1977). In Germany, the "Objective weather types classification of the German Weather Service" is used (*Bissolli* and *Dittmann*, 2001). Poland uses the synoptic classification according to *Niedźwiedź* (2013) – known as the "Calendar of circulation types, air masses and fronts for Southern Poland". In Hungary, the classification according to *Péczely* (1983) is summarized in the "Catalog of the macro-synoptic types for Hungary". In the Czech Republic and Slovakia, the first "Catalog of Weather Situations for the Territory of the Czechoslovak Socialist Republic" was published by the national hydrometeorological service in 1968 (*Brádka et al,* 1968). The first synoptic situations were classified for the year 1946. After bilateral discussions and consensus between meteorologists from both countries in 1991, the catalog summarizes weather types separately for Slovakia and the Czech Republic. Classification of weather types was carried out by the Slovak Hydrometeorological Institute (SHMI) between 1991 and 2015 from the calendar of weather type situations that is available on the SHMI website (*SHMÚ*, 2020) First, days with cyclonic situations related to different directions of the prevailing atmospheric airflow and different position of the low and high pressure areas were selected.

Records extracted from the calendar of weather type situations (*SHMÚ*, 2020) were used to select days with cyclonic weather situations. The duration of cyclonic situations in the analyzed period 1991–2015 ranged from 1 to more than 10 days. Using the Catalog of Weather Situations (*Brádka et al.*, 1968), the synoptic situations were selected according to the nature of cyclonality and the predominant airflow direction. In order to increase the sample size, the weather types were grouped into ''supertypes'' according to their cyclonality and the dominant direction of airflow following the procedure of *Beranová* and *Huth* (2005) (*Table 1*). The synoptic situations with directions W + NW, N + NE, E + SE, S + SW (*Fig. 3*) were retained for further analysis. A list of cyclonic situations from the period 1991–2015 was created for the purposes of this paper; i.e., the number of days with a certain type of cyclonic situation during 5-year periods was extracted from the database.

Data from more than 600 precipitation gauges covering a period of 25 years were processed. The data contained information on the indicative of the precipitation gauge (station ID), location name, date, and the precipitation total measured in the rain gauge. The data were sorted into groups with given weather type of cyclonic situation. The precipitation totals were first processed for all cyclonic situations with certain airflow direction, and then they were interpolated in the ArcGIS 10. The interpolation procedure described in *Polčák* and *Mészáros* (2019) was adopted in this study. We used the Topo to Raster method, since according to *Šercl* (2008), the Topo to Raster method is suitable for interpolating point-measured precipitation. This method estimates interpolated values from four adjacent points using an iterative method of finite differences. The isolines created by this method resemble well the isolines that an expert would draw manually on a paper map. The greatest advantage of this interpolation tool is that it enables the user to define the boundary of the territory within which the interpolation is to be carried out and also to assign the lowest value used in interpolation. In this way, areas between stations with zero totals are not interpolated into physically unrealistic negative values, since precipitation total has to be always positive or equal to zero. This interpolation technique was used for each of the cyclonic situations. The individual precipitation fields were summed up for each type of cyclonic situation in the ArcGIS 10 by Raster Calculator. The sums were subsequently divided by the number of years to get precipitation fields of mean annual totals separately for each of the individual types of cyclonic situations.

Table 1. List of synoptic types and their merging into groups (supertypes) according to cyclonality and prevailing airflow. Source*: Beranová* and *Huth* (2005).

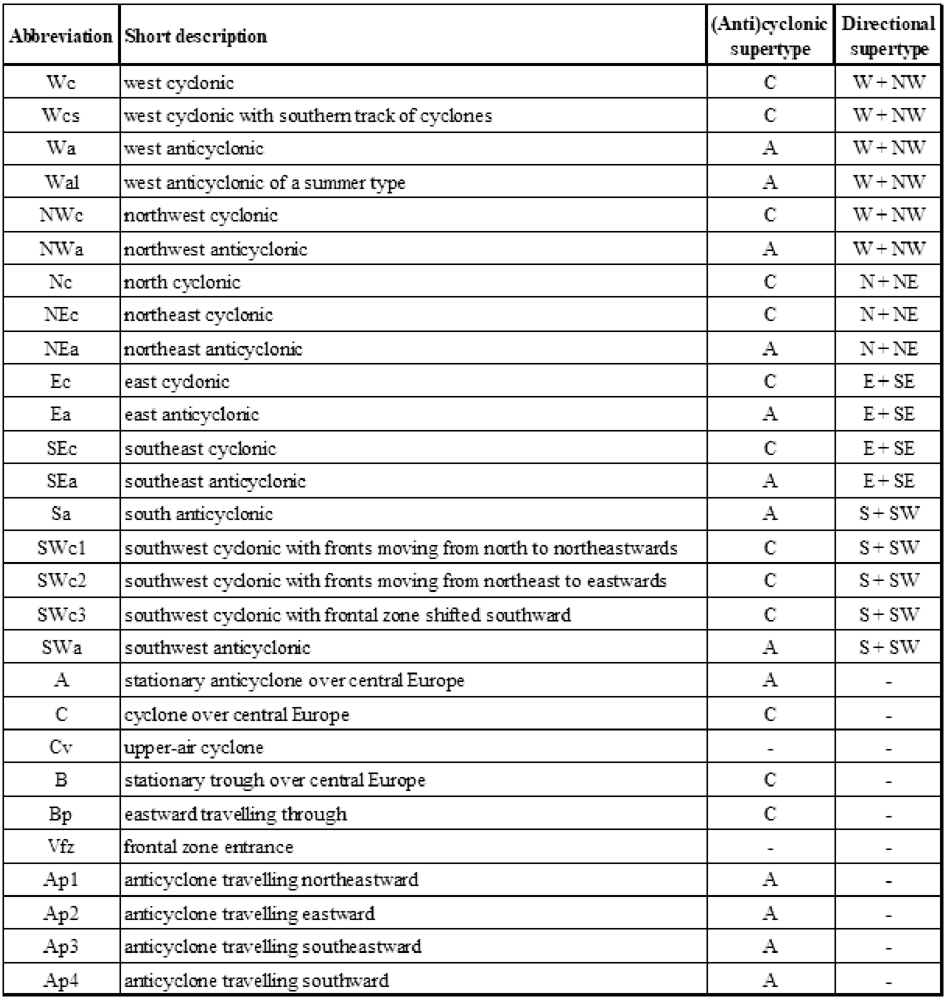

Abbreviation	**Short description**	**(Anti)cyclonic supertype**	**Directional supertype**
Wc	west cyclonic	C	W + NW
Wcs	west cyclonic with southern track of cyclones	C	W + NW
Wa	west anticyclonic	A	W + NW
Wal	west anticyclonic of a summer type	A	W + NW
NWc	northwest cyclonic	C	W + NW
NWa	northwest anticyclonic	A	W + NW
Nc	north cyclonic	C	N + NE
NEc	northeast cyclonic	C	N + NE
NEa	northeast anticyclonic	A	N + NE
Ec	east cyclonic	C	E + SE
Ea	east anticyclonic	A	E + SE
SEc	southeast cyclonic	C	E + SE
SEa	southeast anticyclonic	A	E + SE
Sa	south anticyclonic	A	S + SW
SWc1	southwest cyclonic with fronts moving from north to northeastwards	C	S + SW
SWc2	southwest cyclonic with fronts moving from northeast to eastwards	C	S + SW
SWc3	southwest cyclonic with frontal zone shifted southward	C	S + SW
SWa	southwest anticyclonic	A	S + SW
A	stationary anticyclone over central Europe	A	-
C	cyclone over central Europe	C	-
Cv	upper-air cyclone	-	-
B	stationary trough over central Europe	C	-
Bp	eastward travelling through	C	-
Vfz	frontal zone entrance	-	-
Ap1	anticyclone travelling northeastward	A	-
Ap2	anticyclone travelling eastward	A	-
Ap3	anticyclone travelling southeastward	A	-
Ap4	anticyclone travelling southward	A	-

The mean annual precipitation total for the individual stations was calculated from the monthly mean precipitation totals. The mean annual totals were interpolated in ArcGIS 10. Using the precipitation fields created in this way, the percentage of individual types of cyclonic situations with respect to the total mean annual precipitation total was expressed for the period 1991–2015. The procedure is described in detail by *Mészáros* (2019).

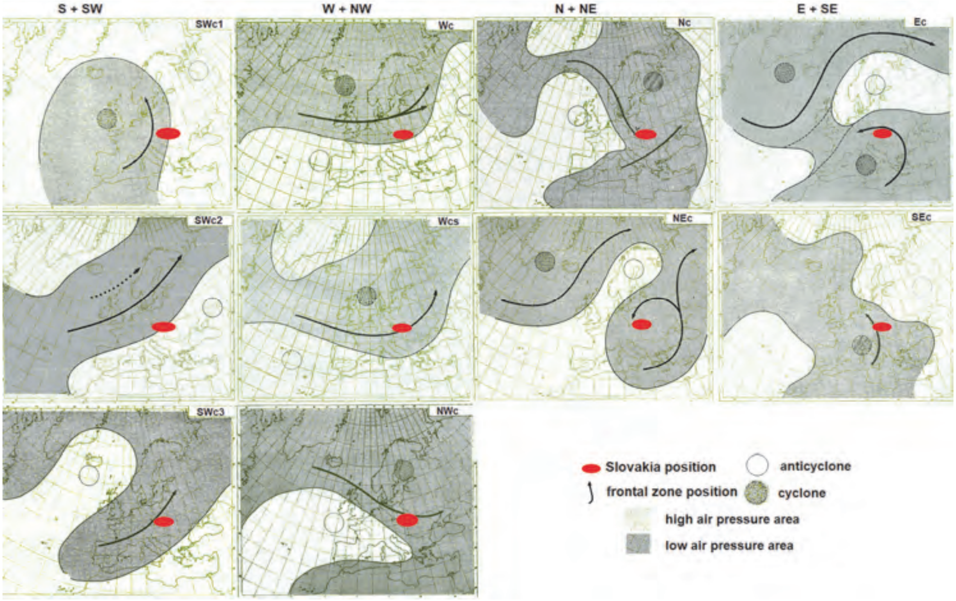

Fig. 3. Schematic layout of cyclonic situations. Types in each column create directional supertypes.

3. Results

The occurrence of individual cyclonic weather types based on their prevailing airflow direction was analyzed for the period 1991–2015. The number of days with all cyclonic weather types, the number of days with cyclonic weather types in 5-year periods and the mean precipitation total per day with cyclonic weather types in 5-year periods, are displayed in *Fig. 4*. The spatial distribution of the mean annual precipitation totals corresponding to the individual weather types of cyclonic situations is shown in *Fig. 5*. The precipitation fields for the cyclonic supertypes are shown in *Fig. 6*. The contribution of the individual weather types of cyclonic situations to the mean annual precipitation total is shown in *Fig. 7*, while the contribution of supertypes during the period 1991–2015 is shown in *Fig. 8*. Mean, minimum, and maximum values of mean annual precipitation totals during the individual weather types of cyclonic situations along with the contribution of the individual weather types and cyclonic supertypes to the mean annual precipitation total are summarized in *Table 2*. (In this table, mean total is the areal mean value of the average annual precipitation total, min total is the areal minimum value of the average annual precipitation total, max total is the areal maximum value of the average annual precipitation total, mean percentage is the areal mean value of the contribution to the mean annual precipitation total for all weather types, min percentage is the areal minimum value of the contribution to the mean annual precipitation total for all weather types, max percentage is the areal maximum value of the contribution to the mean annual precipitation total for all weather types. Values were obtained from precipitation fields calculated by interpolating precipitation data).

3.1. Occurrence of cyclonic situations (period 1991–2015)

From the selected weather types, the Wc type was the most frequent one, with 26 days per year, on average. This confirms that westerly cyclonic flow prevails in Slovakia. The second most frequent was the NEc type occurring 24 days per year. The NWc type occurred 18 days per year. The days with SWc3 and Wcs types occurred 10 times per year, while days with types SWc1 and SEc occurred only 9 times per year. All selected weather types had a declining trend, except for the types SWc2 and NWc. However, perhaps more important than the number of days per year is to identify the season of the year when the days with a given type occur. For example, during the winter 2012–2013 and the early spring of 2013, an anomalously large number of Mediterranean cyclones was observed in the Carpathian Basin (*Zsilinszki et al.*, 2019). These cyclonic situations led to floods in the southern half of Slovakia (*SHMÚ*, 2014).

One of the indicators of the activity of cyclonic situations is their frequency of occurrence during the period of observation. This allows us to investigate the annual fluctuations in cyclonic situations. The 1990s were rich in the number of days with cyclonic situations. In the early 2000s, the number of days with a cyclonic situation fluctuated considerably. There were years with less than 200 days (e.g., the dry year of 2003) but also with almost 250 days with a cyclonic situation (e.g., the wet year of 2010). During the last years of the observation period, the absolute number of days with cyclonic situations did not exceed 200. The general trend in the form of a 5-year moving average clearly indicates a slight decrease in the activity of cyclonic situations in the investigated territory. The frequency of occurrence of days with cyclonic situation declined in most weather types (*Fig. 4* top and middle). However, this decline is not observed in the precipitation amount. The total amount of precipitation per year in Slovakia did not decrease significantly (*Markovič et al.*, 2016) despite the facts that there have been fewer days with cyclonic situations. This means that precipitation totals during cyclonic situations increased (*Fig. 4* down), and convective precipitation has increased during days with other weather situations. The investigation of *Markovič et al.* (2016) confirms a higher proportion of storm showers in the mean annual total precipitation in the recent years.

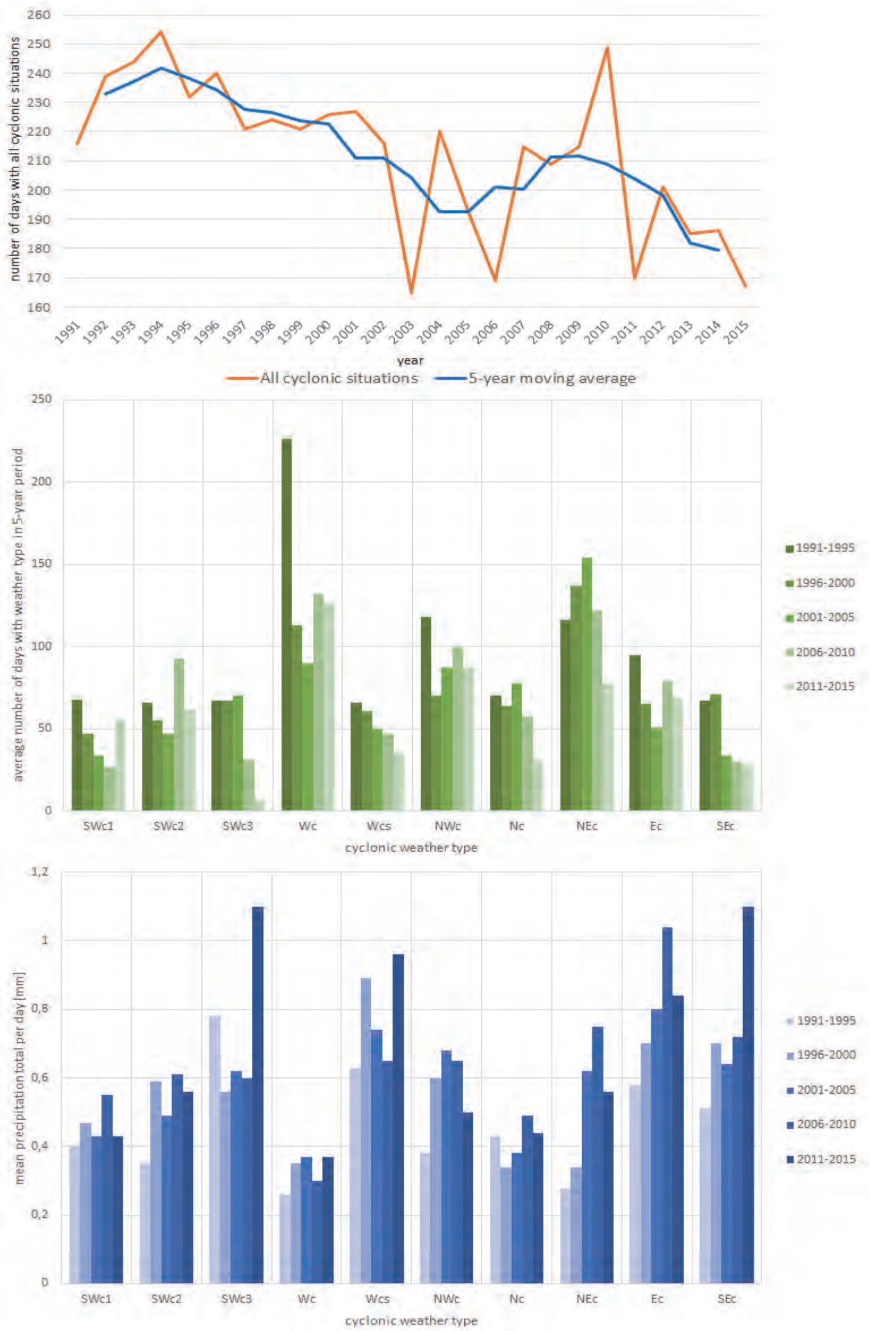

Fig. 4. Top: The number of days with all cyclonic situations in the period 1991–2015 and the 5-year moving average. Middle: The number of days with cyclonic weather types in 5-year periods. Bottom: Mean precipitation total per day with cyclonic weather type in 5-year periods.

3.2. *Mean annual precipitation totals during individual weather types of cyclonic situations and cyclonic supertypes with different airflow direction (period 1991–2015)*

Directional cyclonic supertype S + SW

During this supertype, the mean annual totals ranged from 52 to 174 mm. The mean precipitation total was 87 mm. The highest totals (> 150 mm) were observed on the windward southern slopes of the Western Carpathians in the central part of the territory, on the highest summits of the Western Carpathians in the northern part of the territory, and in the Eastern Carpathians in the eastern part of the territory. The lowest totals (< 70 mm) were observed in the Western Pannonian and Eastern Pannonian Plain. In general, precipitation totals increase with altitude, and therefore, the totals in the lowlands were lower. The Western Pannonian Plain lies in the rain shadow of the Alps, and the Eastern Pannonian Plain is located in the rain shadow of the North Hungarian Mountains. Also, low precipitation totals (< 80 mm) were observed in the basins in the northern part of the territory, which are located in the lee of the Carpathian arch, and in the basins located in the southern part of the territory, which are in the lee of the North Hungarian Mountains. Precipitation fields were similar in all types belonging to this directional supertype (SWc1, SWc2, SWc3). Only the type SWc1 differed from types SWc2 and SWc3 in that there were no higher totals in the Eastern Carpathians. Maximum of the mean annual total was investigated for the SWc2 type (74 mm) and minimum for the SWc1 type (12 mm).

Directional cyclonic supertype W + NW

This supertype was characterized by the widest range of mean annual totals from 65 to 518 mm. The mean value of the total was 159 mm. The windward effect was very strong here, thus the highest precipitation (> 400 mm) fell in the Western Carpathians in the northwestern part of the territory. The lowest precipitation (< 100 mm) fell in the southern and eastern parts of the territory in a significant rain shadow. Types from this supertype (Wc, Wcs, NWc) had a similar territorial distribution of precipitation. The difference was in the amount of the precipitation total. Maximum was for the Wc type (200 mm) and minimum for the Wcs type (40 mm). The Wc type (prevailing in Slovakia) had the highest mean annual precipitation total (69 mm) from all selected weather types.

Directional cyclonic supertype N + NE

During this supertype, the average precipitation total was 38 to 323 mm per year. The mean value of the precipitation total was 87 mm. The highest precipitation totals (> 200 mm) were observed on the windward northern slopes of the Western Carpathians in the northernmost part of the territory and the Eastern Carpathians in the northeasternmost. The lowest totals (< 60 mm) were observed in the western third of the territory and in the southern half of the central part of the territory.

This part was protected by the Carpathian Mountains from precipitation arriving from the north and northeast. In both types belonging to this directional supertype (Nc, NEc), high precipitation totals (> 150 mm) occurred mainly in the north during the NEc type, and partially also in the east. Low precipitation totals (< 20 mm) occurred in the southern half of the territory and a rain shadow was observed in the south of the highest summits of the Carpathians during the Nc type and in almost the entire western half of the territory during the NEc type.

Directional cyclonic supertype E + SE

This supertype was characterized by the smallest range of mean annual precipitation totals ranging from 49 to 155 mm. The mean precipitation total was 89 mm. A great contrast was discernible between the southern and northern parts of the territory induced by the windward effect on the southern slopes of the Western Carpathians. The maximum precipitation totals (> 150 mm) were observed in the highest elevations of the Western Carpathians. A rain shadow was observed in the northern and eastern parts of the territory. The Ec type had higher characteristics of precipitation totals (mean 53 mm, maximum 103 mm, minimum 26 mm) than the SEc type (mean 33 mm, maximum 69 mm, minimum 16 mm). Very interesting is the precipitation field in the eastern part of the territory during the Ec type due to the rain shadow of the Ukrainian Eastern Carpathians from the east and rain shadow in the north of the territory during the SEc type, while further northern part the height of the mean annual precipitation total decreased. The only exceptions were the highest summits of the Western Carpathians.

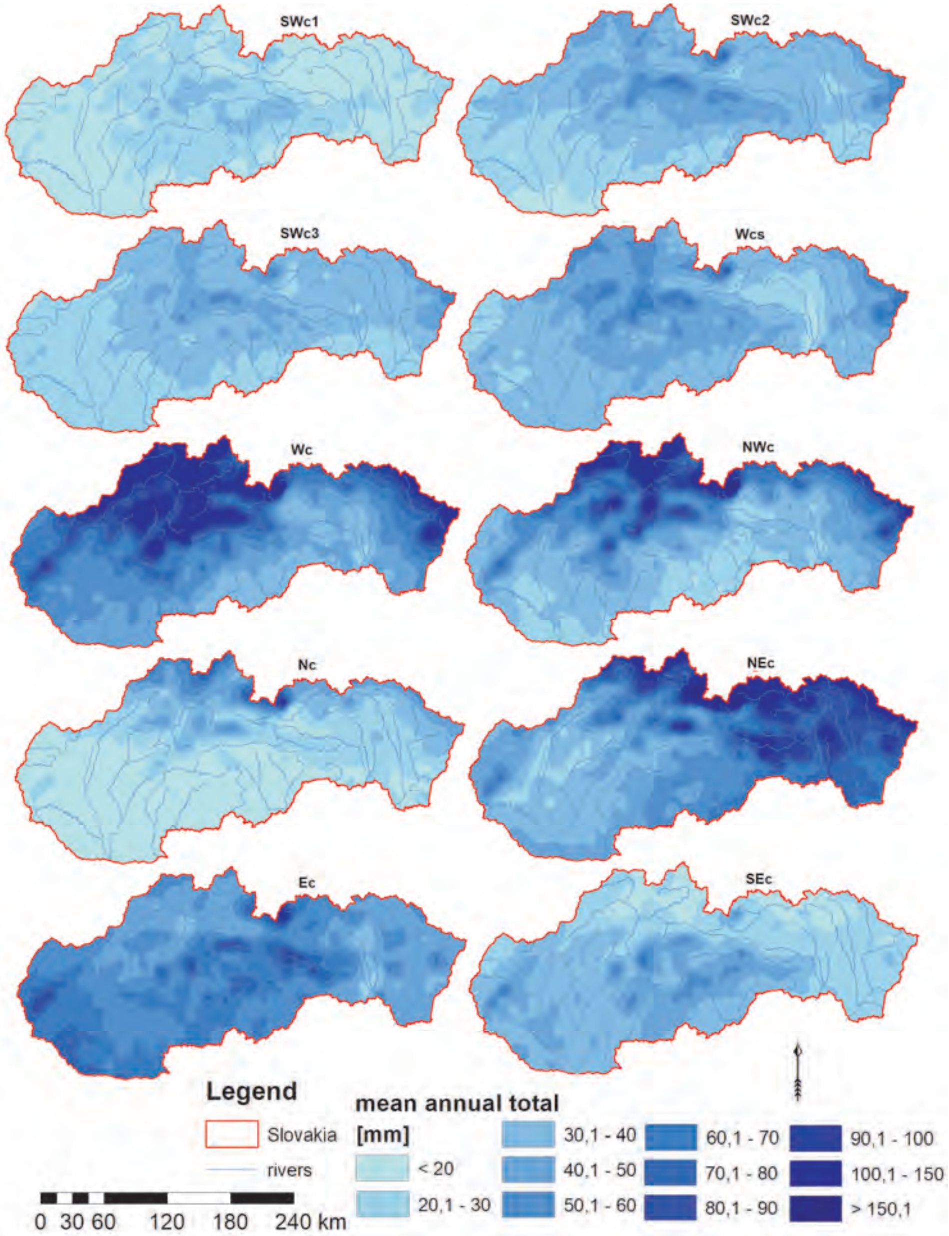

Fig. 5. Mean annual precipitation total in Slovakia during individual types of cyclonic situations for the period 1991–2015.

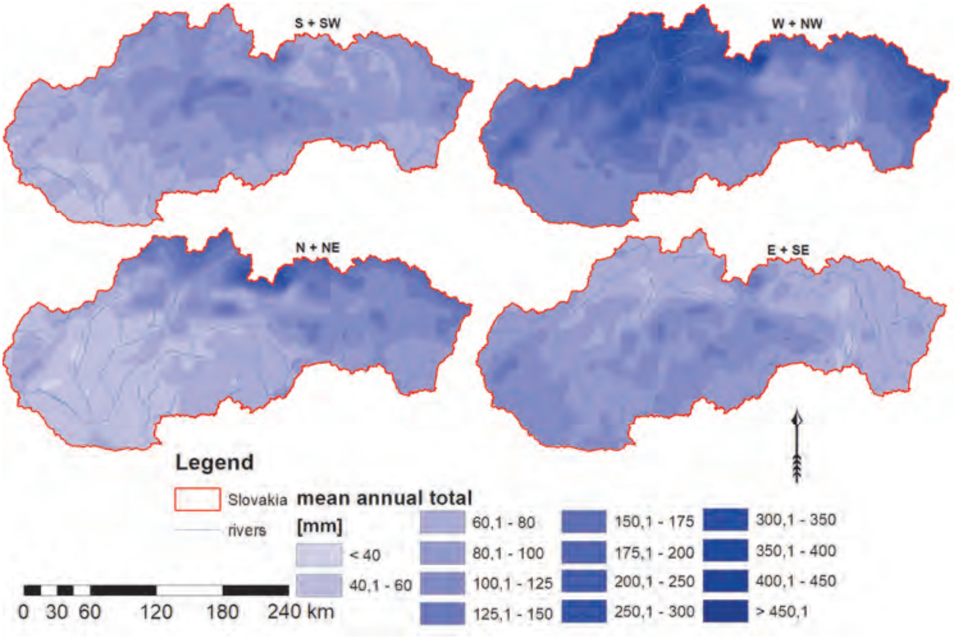

Fig. 6. Mean annual precipitation total in Slovakia during cyclonic supertypes from the mean annual precipitation total for the period 1991–2015.

3.3. *Percentage of the mean precipitation total fallen during individual weather types of cyclonic situations and cyclonic supertypes with different airflow directions from the mean annual precipitation total (period 1991–2015)*

The spatial expression of the percentage contribution of precipitation in individual parts of the territory is important from the point of view, that we can identify in which part which cyclonic type (or supertype) had the largest or smallest share in the mean annual precipitation total.

Directional cyclonic supertype S + SW

This supertype was represented in the mean annual total by 9 to 15%, with an average 12%. Above 14%, it was in the southern half of the central part of the territory. Up to 10% were totals in the northernmost, but also in the southwestern part of the territory. The individual types SWc1, SWc2 and SWc3 had little significant contribution, with maximum 6% during the SWc3 type.

Directional cyclonic supertype W + NW

This supertype was characterized by the highest percentage (from 11 to 36%) with an overall mean of 21%. The largest percentage (> 30%) was observed in the mountains located in the northwestern part of the territory. The smallest percentage (approx. 14%) was observed in the eastern part of the territory. The Wc type is the most significant direction for the Western Carpathians in the northwestern part of the territory (> 30%). The NWc type had a high contribution in northern part of the territory.

Directional cyclonic supertype N + NE

Precipitation from this supertype contributed to the mean annual total by 6 to 24% (12% on average). They had the largest percentage in the northern and northeastern parts of the territory, over 20%. Up to 8% was in the southern half of the western and central parts of the territory. The Nc type had over 6% in the northernmost part of the territory, and the NEc type had above 16% in the very north of the territory in the highest locations of the Western Carpathians and above 10% in a large area in the eastern part of the territory.

Directional cyclonic supertype E + SE

This supertype was characterized by a range of percentage from 6 to 21%, with an average of 13%. The lowest percentage (< 8%) was observed in the northern and northeastern parts of the territory. The largest percentage (> 18%) was observed in the southwestern and southern parts of the territory. The Ec type had the highest percentage in the Western Pannonian Plain and the southwestern part of the territory. The same holds for the SEc type, but in this case the percentage was lower.

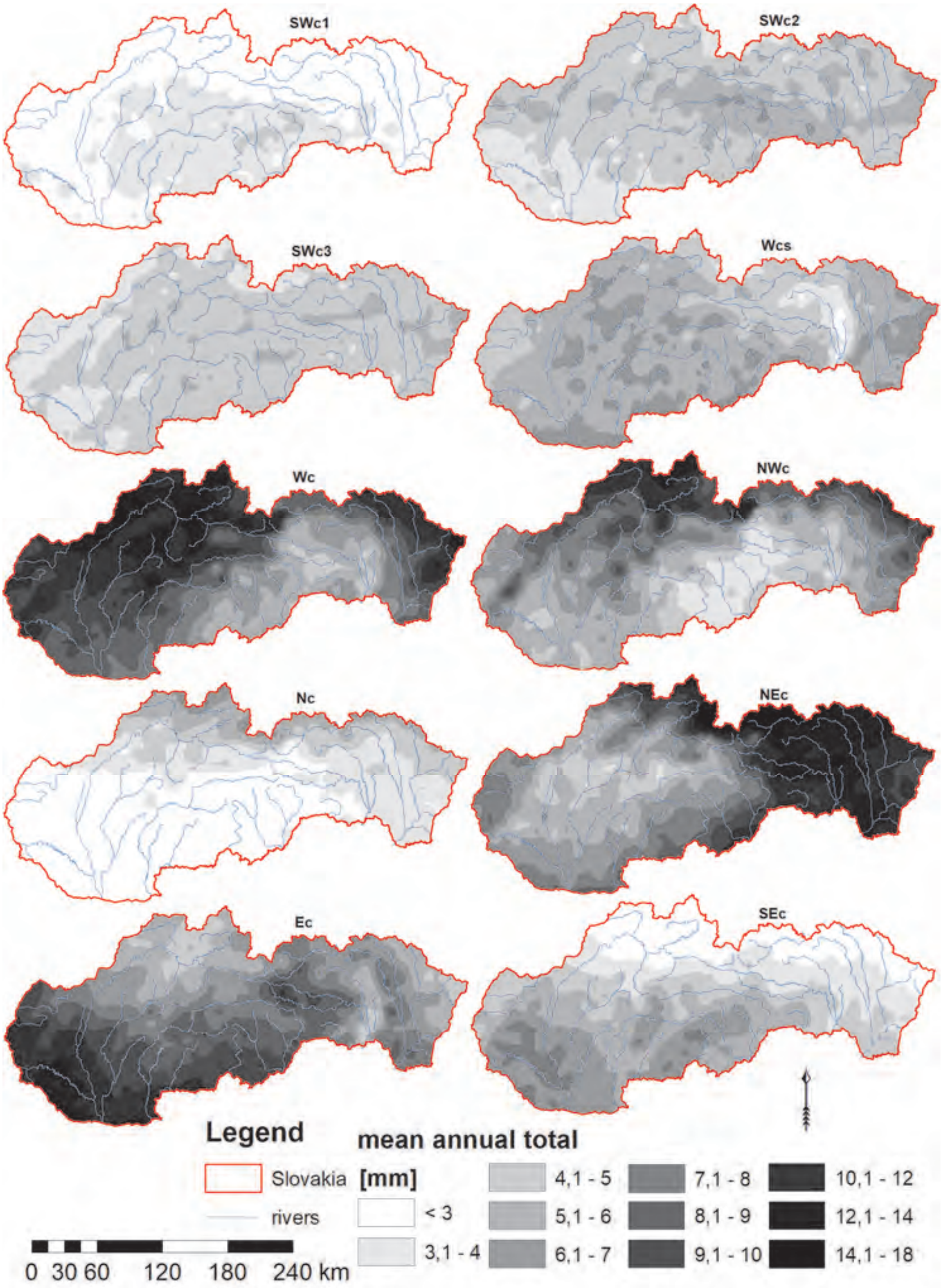

Fig. 7. Percentage of the mean annual precipitation fallen during individual types of cyclonic situations to the mean annual total precipitation in Slovakia for the period 1991–2015.

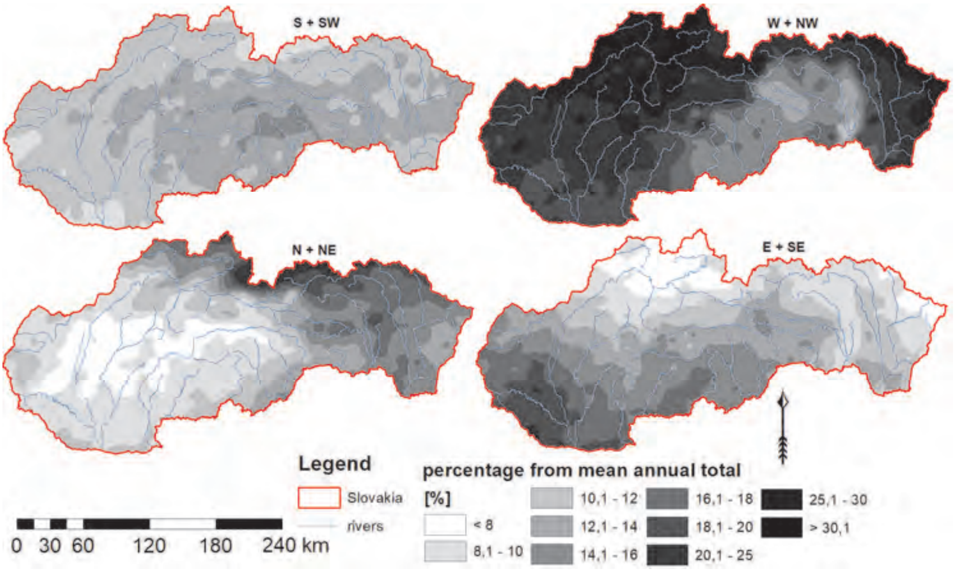

Fig. 8. Percentage of the mean annual precipitation fallen during individual cyclonic supertypes to the mean annual total precipitation in Slovakia for the period 1991–2015.

Table 2. Statistical values of mean annual precipitation totals for individual types of cyclonic situations and cyclonic supertypes for the period 1995–2015, and their contribution to the mean annual precipitation total for all weather types.

Type	Total [mm]			Percentage [%]		
	Mean	Min	Max	Mean	Min	Max
SWc1	21	12	40	3	1	4
SWc2	30	17	74	5	3	6
SWc3	32	18	63	4	3	6
Wc	69	24	200	9	4	17
Wcs	40	17	82	5	3	7
NWc	51	19	236	7	3	14
Nc	25	10	111	3	2	7
NEc	62	24	239	8	4	18
Ec	53	26	103	8	4	13
SEc	33	16	69	5	2	8

Supertype	Total [mm]			Percentage [%]		
	Mean	Min	Max	Mean	Min	Max
S + SW	87	52	174	12	9	15
W + NW	159	65	518	21	11	36
N + NE	87	38	323	12	6	24
E + SE	89	49	155	13	6	21
All directional cyclonic types	422	277	1150	57	46	72
All weather types	733	527	1757	-	-	-

4. Conclusion

During the period 1991–2015, the most frequent weather type in Slovakia was the Wc, followed by the NEc and NWc types. Days with SWc1, SEc, SWc3, and Wcs types were less frequent. During the analyzed period, a decrease in the incidence of days with cyclonal synoptic situation was observed. Nevertheless, the mean annual precipitation did not decrease. As the surface runoff is inherently linked to the precipitation (*Petrow et al*., 2009), it would be interesting to carry out an additional research in the future and focus on changes in runoff due to the altered occurrence of weather types.

This study showed that the mean annual precipitation totals were highest during the types Wc (69 mm), NEc (62 mm), and Ec (53 mm). The lowest mean annual precipitation totals were observed during the types SWc1 (21 mm) and Nc (25 mm). These types of cyclonic situations were accompanied with the lowest overall annual mean precipitation totals. Up to 15 mm of precipitation fell in the south of the territory during the Nc type, and up to 15 mm during the SWc1 type in the Western Pannonian and Eastern Pannonian Plains and in the basins in the northern part of the territory. The maximum annual totals occurred during the NEc type with almost 240 mm on the windward northern slopes of the Western and Eastern Carpathians in the northernmost and northeastern parts of the territory, and during the NWc type in the highest locations of the Western Carpathians in the very north. Regarding cyclonic supertypes, i.e., considering airflow directions, the highest mean annual precipitation totals fell during situations from the directional supertype W + NW and the lowest from the directional supertype N + NE, although maximum annual totals were observed during the NEc type (supertype S + SW had a mean annual total higher by only 0.3 mm). As the most common cyclonic situation type is not always responsible for the greatest floods (*Bednorz et al.,* 2019), it would be interesting to study which type, or supertype, of cyclonic situations is responsible for major floods. On the other hand, it has been shown that a deficiency of some cyclonic weather types can cause drought (*Stahl* and *Demuth,* 1999).

In terms of the contribution of the precipitation total associated with a certain type of cyclonic situation and airflow direction on the mean annual precipitation total, types with the highest percentages were: Wc with 9%, NEc with 8%, and Ec with 8%. The least significant ones, were the SWc1 and Nc types, both with 3% contribution. In terms of locations with the highest contribution to annual precipitation totals, locations in the highest parts of the Western Carpathians contributed with 18% during the NEc type, in the northwestern part of the territory with 17% during the Wc type, and in the northwestern and northern parts of the territory with 14% during the NWc type. The SWc1 type contributed only with 1% in the northernmost part of the territory. The Nc type contributed with 2% in the western and central part of the southern half of the territory, and the SEc type contributed with 2% in the northern part of the territory.

Our analyses allowed us to identify the most and the least affected regions by precipitation arising from a given type of cyclonic situation (supertype). Windward and leeward locations were identified as well. In general, it can be concluded that the investigated territory of Slovakia had its maximum precipitation mainly during the supertype W + NW (mean percentage for the area is 21%). In the northern and eastern parts of the territory, precipitation from supertype N + NE was significant. An important agricultural area and the most densely populated part of the territory in the Western Pannonian Plain received high percentage of precipitation totals originating in the E + SE supertype situations.

In this paper, we analyzed atmospheric precipitation, which is the main source of water in our country. The presented results are beneficial for the country's agriculture, tourism, industry, but they will be most appreciated by experts in climatology, meteorology, and hydrology. The frequency of weather types occurrence is influenced by the North Atlantic Oscillation (*Fernández-González et al.*, 2012). Therefore, our research avenue for the near future is to investigate the dependence of weather types on the positive or negative values of the NAO index. It will be necessary to process a longer period. Then, we will be able to predict which locations will be above or below average in terms of precipitation during the next season.

Acknowledgements: This work was supported by the projects Doktogrant APP087 and VEGA 2/0004/19.

References

Bednorz, E., Wrzesiński, D., Tomczyk, A.M., and *Jasik, D.,* 2019: Classification of synoptic conditions of summer floods in Polish Sudeten Mountains. *Water 11*, 1450. https://doi.org/10.3390/w11071450

Beranová, R. and *Huth,* 2005: *R.* Long-term changes in heat island of Prague under different synoptic conditions. *Theor. Appl. Climatol. 28*, 113–118.https://doi.org/10.1007/s00704-004-0115-y

Bissolli, P. and *Dittmann, E.,* 2001: The objective weather types classification of the German Weather Service and its possibilities of application to environmental and meteorological investigations. *Met. Zeitschr. 10*, 253–260. https://doi.org/10.1127/0941-2948/2001/0010-0253

Brádka, J., et al., 1968: Katalog povětrnostních situací pro území ČSSR. Praha: Hydrometeorologický ústav, 94 pp. (in Czech)

Fernandez-Gonzalez, S., del Rio, S., Castro, A., Penas, A., Fernandez-Raga, M., Calvo, A., and *Fraile, R.,* 2012: Connection between NAO, weather types and precipitation in León, Spain (1948–2008). *Int. J. Climatol. 32*, 2181–2196. https://doi.org/10.1002/joc.2431

Hess, P. and *Brezowsky, H.,* 1977*:* Katalog der Großwetterlagen Europas 1881–1976. 3. verbesserte und ergänzte Aufl. *Ber. Dt. Wetterd. 15* (113). (in German)

Markovič, L., Faško, P., and *Bochníček, O.,* 2016: Zmeny dlhodobých priemerných mesačných a ročných úhrnov atmosférických zrážok na Slovensku. *Acta Hydrologica Slovaca, 2*, 235–242. (in Slovak)

Mészáros, J., 2019: Priestorové zákonitosti rozloženia atmosferických zrážok na Slovensku pri južných cyklonálnych situáciách za obdobie rokov 1991–2015. Bratislava: Prírodovedecká fakulta

UK, 108 pp. [online]. [cit. 2021-01-11]. Available on the internet: http://opac.crzp.sk/?fn=docviewChild000DCC77 (in Slovak)

Niedźwiedź, T., 2013: Calendar of circulation types, air masses and fronts for Southern Poland. [online]. [cit. 2020-01-09] Available on the internet: http://klimat.wnoz.us.edu.pl/

Péczely G., 1983: Magyarország makroszinoptikus helyzeteinek katalógusa (1881-1983). Budapest: OMSZ Kisebb kiadványok 53. (In Hungarian)

Polčák, N. and *Mészáros,* J., 2019: The effect of relief on the distribution of atmospheric precipitation in Slovakia in the southern cyclonic situations. Geografický časopis 70, 259–272. (In Czech) https://doi.org/10.31577/geogrcas.2018.70.3.14

SHMÚ, 2009: Klimatické pomery Slovenskej republiky. 2009 [online]. [cit. 2017-11-09]. Available on the internet: http://www.shmu.sk/sk/?page=1064. (In Slovak)

SHMÚ, 2014: Správa o povodniach za rok 2013. 2014 [online]. [cit. 2020-06-11]. Available on the internet: http://www.shmu.sk/File/HIPS/Povodnova_sprava2013.pdf (In Slovak)

SHMÚ. 2020: Typy poveternostných situácií. 2020 [online]. [cit. 2020-05-23]. Available on the internet: http://www.shmu.sk/sk/?page=8. (In Slovak)

Stahl, K. and *Demuth, S., 1999:* Linking streamflow drought to the occurrence of atmospheric circulation patterns. *Hydrol. Sci. J. . 44,* 467–482. https://doi.org/10.1080/02626669909492240

Šercl, P. 2008: Hodnocení metod odhadu plošných srážek. *Meteorologické zprávy 61*. 33–43. (in Czech) https://doi.org/10.17221/1902-CJGPB

Petrow, T. Zimmer, J., and *Merz, B.,* 2009: Changes in the flood hazard in Germany through changing frequency and persistence of circulation patterns. *Nat. Hazards Earth Syst. Sci. 9*, 1409–1423. https://doi.org/10.5194/nhess-9-1409-2009

Zsilinszki A., Dezső Z., Bartholy J., and *Pongrácz R.,* 2019: Synoptic-climatological analysis of high level air flow over the Carpathian Basin. *Időjárás 123*, 19–38. https://doi.org/10.28974/idojaras.2019.1.2

DOI:10.28974/idojaras.2022.2.7

IDŐJÁRÁS

Quarterly Journal of the Hungarian Meteorological Service
Vol. 126, No. 2, April – June, 2022, pp. 285–295

Short Contribution

On the correction of multiple minute sampling rainfall data of tipping bucket rainfall recorders

Tibor Rácz

Doctoral School of Environmental Sciences
at the Hungarian University of Agriculture and Life Sciences
Páter Károly utca 1, Gödöllő, 2100, Hungary

Author *E-mail: raczt167@gmail.com*

(Manuscript received in final form February 8, 2021)

Abstract— In the last decades of the 1900s, the tipping bucket rainfall gauges (TBG) were used to record the sub-daily rainfall data. In the first period of the rainfall data recording, as a result of the lack of efficient data storage and data transmission, the sampling period of the TBG devices was chosen in a magnitude of 10–20 minutes. Consequently, there are historical datasets characterized by several minutes long sampling periods. Since the turn of the 2000s, the data handling has been revolutionized; the sampling period has diminished to one minute. There is a systematic error of the TBG technique which has been investigated since the middle of the 1900s. Between 2004 and 2008, a comprehensive research was performed to determine the correction equation for several TBG devices. These results can be utilized for the short sampling period measurements (one minute sampling), but for longer sampling period data, further corrections are needed. In this paper, a supplementary correction is presented. On the base of the mathematical determination of the correction factor, simple estimation will be proposed to be able to execute the necessary correction. After the presentation of the correction factor, a general correction factor is proposed for larger geographical regions and wide time span of the measurements. The revision of the historical rainfall data recorded by TBG devices can be important in several issues, such as the re-evaluation of intensity-duration-frequency (IDF) curves, and in other fields.

Key-words: historical rainfall data, tipping bucket gauge, rainfall recorder, rainfall intensity, data correction

1. Introduction

The measurement of the rainfall intensities has great importance in providing key data of engineering hydrology for the design works of drainage systems or flood protection interventions. Although the measurement of the rainfall intensity has a 300-year-long history (*Kurytka*, 1953), the importance of the rainfall intensity was recognized in its significance only in the middle of the 19th century, after Mulvany has worked out the rational method (*Mulvany*, 1851). First, the rainfall intensity measurement was performed by rainfall writers, detecting the changing water level in the tank of the device. Their dominance was evident till the 1970s. Because of the simpler electronic data recording and ready-to-process data format, the water level writing gauges got behind the simpler, smaller TBG devices in the practice. These devices have a long history; Sir Christopher Wren built the first tipping bucket gauge in the second half of the 1600s, in an early phase of the development of modern rainfall measurement devices. In the following centuries, there were several arrangements of these kinds of gauges. The appearance of the electronic data registration and the quite simple processing option of the data performed by TBG units have made the technology wide-spreading.

As every measurement technique, the TBG has its systematic error. Beyond the usual sources of error, such as the wind-caused uncertainty of the data, there are structural sources of errors, the so-called local random errors (*Habib et al.*, 2013). The nature of these errors are explained comprehensively in the related papers, and there are several correction methods to diminish or exclude it (*Marsalek,* 1981; *Adami* and *Da Deppo* 1985; *Niemczynovicz,* 1986; *Habib et al.*, 2001; *Luyckx* and *Berlamont,* 2001; *Frankhauser,* 1997; *Vuerich et al.,* 2009; *Duchon* and *Biddle,* 2010). These solutions are fundamental for the short sampling period (characteristically one-minute) measurements. However, for an old time series having longer sampling period, n times longer than the one-minute unit interval (so n-minute-long), a further correction method is required. In this paper, a proposal for a supplementary correction is presented, for 5–10 minutes or longer intervals data.

2. Methods

The proposed correction for longer sampling periods is based on the results of the measurements and elaborated correction formulae of Vuerich and his colleagues (*Vuerich et al.,* 2009), using power function between the measured and reference data, as

$$i_c = a \cdot i_m^b, \tag{1}$$

where i_c is the corrected value of the rainfall intensity (or reference intensity during the calibration process), i_m is the measured value of the rainfall intensity, and a, b are parameters related to the TBG rainfall gauge.

The rainfall intensity is the function of time and space, and it is a volumetric flux, so the $V(t)$ volume flows through an A unit surface in a unit time interval, $i = i(t, x, y)$. The surface can be written as $A = A(x, y)$ and $dA = dx \cdot dy$, so the intensity can be determined as

$$i(t, x, y) = \frac{d}{dA}\frac{dV(t)}{dt}. \tag{2}$$

The volume of rainfall onto the unit surface in a $t = [T_1, T_2]$ interval can be expressed as

$$V(t) = \iint i(t)dAdt = \int_{T_1}^{T_2} i(t)dt, \tag{3}$$

but the unit of the rainfall intensity conserves the [volume/(area·time)] character.

In the practice, the measurement of the rainfall intensity by the TBG device occurs in finite time units (or sampling periods), in the last decades in one minute. The TBG device counts the number of rainfall volumes equal to the volume of the bucket in one sampling period. Assuming a longer measuring period of several minutes, where the t-long period is n times longer than a supposed unit interval (so the measuring period is n units long), the rainfall volume on a unit area can be calculated as the sum of the unit rainfall volumes of the unit interval, and it can be expressed with the unique intensities of the unit intervals too, so

$$V = \sum_{j=1}^{n} V_j = \sum_{j=1}^{n} \left(i_j \cdot \frac{t}{n}\right), \tag{4}$$

where n is the number of the sub-intervals when the $t = [T_1, T_2]$ interval is divided to shorter intervals with equal lengths, and i_j is the rainfall intensity of the given $\frac{t}{n}$-long interval.

Since the $i_{m,t}$ average intensity of the t-long interval can be expressed with the intensities of the $\frac{t}{n}$ sub-intervals as

$$i_{m,t} = \sum_{j=1}^{n} \frac{i_j}{n}, \tag{5}$$

the V volume can be determined with the average intensity of the t interval as well:

$$V = i_{m,t} \cdot t. \tag{6}$$

The volumes of the Eqs. (4) and (6) must be equal.

However, there is the fact that the TBG device measures rainfall together with its systematic error, so it must be corrected. Applying the correction formula Eq.(1) for Eqs.(4) and (6), the corrected volumes will be different in most of the cases. The question is on the one hand the measure of the difference, which depends on the a and b correction parameters and the t length of the sampling period, and on the other hand, the demanded value of the supplementary correction.

For the empirical investigation of correction factors, the time series were chosen from the German Weather Service’s (DWD’s) one-minute rain depth database. (Source is: https://opendata.dwd.de/climate_environment/CDC/observations_germany/climate/1_minute/precipitation/historical/2016/)

3. Results and discussion

The measure of the supplementary correction will be shown for the t-long sampling period datasets, where in the practice the intensities of shorter intervals are not available, but now, a one-minute sampling period data will be used for the demonstration. For the first, a mathematical explanation will be shown, and then the supplementary correction will be presented using real data. Eq.(1) shows the method of the correction of a one-minute long sampling period rainfall data. If there is a t>1 minimal interval between the two measured data, the fallen rainfall volume (onto a unit area) can be calculated using the before mentioned two ways.

The first is a one-step correction on the base of the average rainfall intensity (see Eq.(6)), on the base of the available data of the t sampling period; this is signed in the further part of this paper with the subscript “A”. The corrected rainfall volume of the t sampling period can be calculated as

$$V_{c,(A)} = a \cdot i_{m,t}^{b} \cdot t = a \cdot t \left(\sum_{j=1}^{n} \frac{i_j}{n}\right)^{b} = \frac{a \cdot t}{n^{b}} \left(\sum_{j=1}^{n} i_j\right)^{b}. \tag{7}$$

The other way (signed with “B”) is the calculation of the sum of corrected n sub-volumes (see Eq.(4)). This step cannot be done when data originate from a measurement with longer sampling period, since the sub-units are not available, but to point out the ratio of these volumes, its formulation must be done:

$$V_{c,(B)} = \sum_{j=1}^{n} \left(a \cdot i_j^{b} \cdot \frac{t}{n}\right) = \frac{a \cdot t}{n} \sum_{j=1}^{n} \left(i_j^{b}\right). \tag{8}$$

The intensity of the jth sub-interval can be expressed with a c_j weighting factor, so

$$i_j = c_j \cdot i_{m,t} \,, \tag{9}$$

where c_j is the a positive weighting factor for the jth sub-interval, and so with Eq.(5)

$$i_{m,t} = \frac{\sum_{j=1}^{n} i_j}{n} = \frac{\sum_{j=1}^{n} c_j \cdot i_{m,t}}{n} = i_{m,t} \cdot \frac{\sum_{j=1}^{n} c_j}{n}, \tag{10}$$

The consequence of Eq.(10) is that $\sum_{j=1}^{n} c_j = n$.

Eqs.(7) and (8) – using Eq.(9) – can be written as

$$V_{c,(A)} = \frac{a \cdot t}{n^b} \left(\sum_{j=1}^{n} i_j\right)^b = \frac{a \cdot t}{n^b} \left(\sum_{j=1}^{n} c_j \cdot i_{m,t}\right)^b = \frac{a \cdot t \cdot {i_{m,t}}^b}{n^b} \left(\sum_{j=1}^{n} c_j\right)^b, \tag{11}$$

$$V_{c,(B)} = \sum_{j=1}^{n} \left(i_{c,j} \cdot \frac{t}{n}\right) = \frac{t}{n} \sum_{j=1}^{n} \left(a \cdot i_{r,j}^b\right) = \frac{a \cdot t}{n} \sum_{j=1}^{n} \left((c_j \cdot i_{m,t})^b\right) = \frac{a \cdot t \cdot {i_{m,t}}^b}{n} \sum_{j=1}^{n} \left(c_j^b\right). \tag{12}$$

The ratio of the two volumes is, using that $\left(\sum_{j=1}^{n} c_j\right)^b = n^b$,

$$\frac{V_{c,(B)}}{V_{c,(A)}} = \frac{\sum_{j=1}^{n} \left(c_j^b\right)}{n} = CF_t. \tag{13}$$

This is the CF_t correction factor which should be used to get the realistic $V_{c,(B)}$ multiplying the volume $V_{c,(A)}$ derivable from the available dataset, so the supplementary correction is

$$V_{c,(B)} = \frac{\sum_{j=1}^{n} \left(c_j^b\right)}{n} V_{c,(A)}. \tag{14}$$

The same is true for the intensities, as well, since the V_c volumes are the $i_{m,t}$ multiplied with t, and expressing the average intensities in both sides of Eq.(14), t will fall out with a simplification, so the adjusted intensity (case “B”)

$$i_{m,t,(B)} = \frac{\sum_{i=1}^{n} \left(c_i^b\right)}{n} \cdot i_{m,t,(A)} = \frac{\sum_{i=1}^{n} \left(c_i^b\right)}{n} \cdot a \cdot i_{m,t}^b. \tag{15}$$

If the intensity is not constant, i.e., when the c_j values are different, then the value of Eq.(13) depends on the distribution of the c_j^b weights (with a constant b). The number of this kinds of distributions can be infinite, however, the estimation of the $\sum_{j=1}^{n} \left(c_j^b\right)$ is possible, as it will be performed a little bit later. Before proposing an estimation method, a short discussion is needed to learn the main characteristics of the CF_t values.

As Eq.(9) shows, if the i_j intensity is constant in the t interval, $c_j = 1$ for every j; in this case the CF_t will get its lowest value, 1.

The weight numbers have an upper limit, as well. The highest value can be calculated if there is only one minute in the investigated interval when the rain depth differs from zero. In this case the only weight different from zero must be n, meanwhile the sum of the bth power of the weights is going to be $\sum_{j=1}^{n}\left(c_j^b\right) = n^b$ and the CF_t value is to be n^{b-1}. So, the CF_t values will be always in the $[1, n^{b-1}]$ bounded interval.

In the major part of the cases, the consecutive intensities are not really different, so their ratio varies not too much, and their values are characteristically near to 1. The highest values of the weights are at the transient period towards the very intensive rainfall, and after the peak, in the returning phase to the lower values. Interestingly, the periods of lower rainfall depths and intensities can be characterized with relatively higher CF_t values. This is the consequence of the greater possibility of the varying of the rainfall intensities in these parts of the rainfall (it is simpler to change a lot from a low base value).

The frequency of the CF_t values is strongly right tailed, and the mean and median of the CF_t values are close to the lower limit.

From practical point of view, there is an issue with the low intensity data of the rainfall intensities. In the low intensity periods, there can be several 0 values, where the TBG device could have detect zero rain depths for several minutes, and there is one or some few measurements in the actual interval. This case demands a careful investigation, since if there was so slight rainfall that the tipping bucket could have been filled only after several minutes, the rain depth and intensity would show 0 values, despite of the continuous rain. In this case the $c_j$values will show 0, however, their values should have been somewhere at 1, and there will be one weight with a high value, which should have been close to the other weights. This phenomenon is caused by the rainfall less intensive than the lowest measurable intensity in one minute. Intervals, which can be characterized by 70–80% 0 values of rainfall are not proposed to the calculation of CF_t values, especially if the non-zero values are only the lowest measurable intensities. The main features of the CF_t values with $b = 1.042$ for 5-minute intervals can be seen in *Fig. 1*. The source of data is the open database of 1-minute rainfall data of the DWD. The station is in Abtsgmünd-Untergröningen, and the rainfall was detected in June 11, 2018. (https://opendata.dwd.de/climate_environment/CDC/).

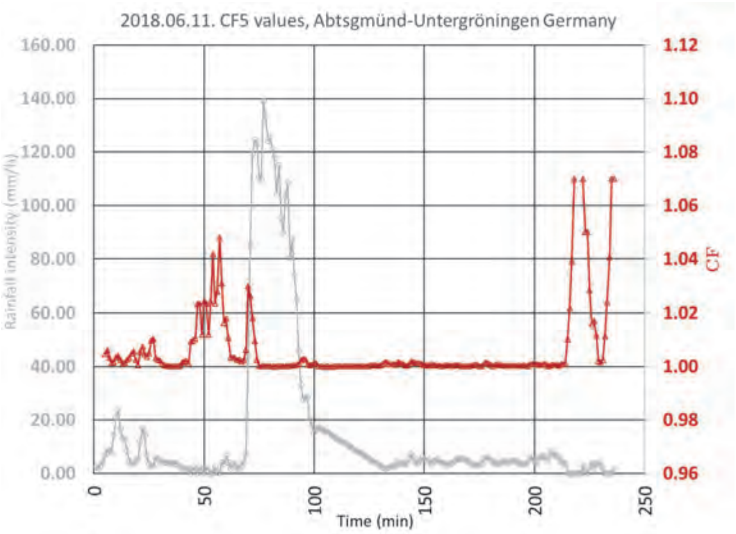

Fig. 1. The main characteristics of CF_5 values in the data of an intensive rainfall, b=1.042.

The above written characteristics of the CF_5 values can be observed in the *Fig. 1*. In the first 25 minutes of the rainfall, the one-minute sampling has resulted in continuously non-zero data, but with fluctuating intensity. The related CF_5 values show fluctuation, as well. Between the 44–57th and the 215–236th minutes, the rainfall intensity was so low that the bucket of the TBG device was not tipped for several minutes, and it resulted in several 0 mm rain depth and rainfall intensities, while despite of these, the rainfall was probably continuous; however, it is impossible to check anymore. Because of the nulls, several high CF_5 values can be observed, but probably these data are caused by the abovementioned issue of the low intensity that is below the intensity measurement resolution of the device; thus, these data are not confirmed. The most intensive part of the rainfall started in the 70th minute, where the fast rising of the rainfall intensity caused a high value in the CF_5 curve. In the highest range of the rainfall intensity – despite of a strong absolute fluctuation – the CF_5 values are low, and they rise again with the decreasing rainfall intensities. The next significant peaks can be found in the 215–236th minutes, as it was mentioned. There were some sections where the length of the null value series was longer than the interval, here the correction factor was not allowed to be calculated (division by zero value of the 5-minute average intensity).

On the base of the experiences, the question marked intervals were not taken into consideration for further calculations. In the next part, the 10-, 20-, 30- and 60-minute CF_5 data will be investigated (*Fig. 2*).

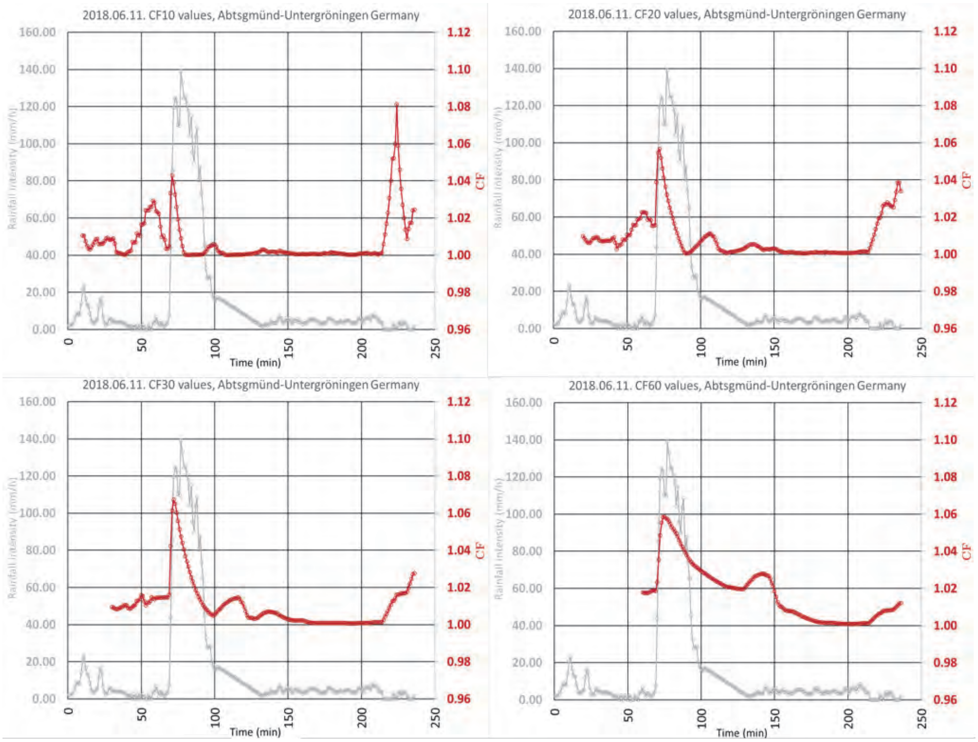

Fig. 2. The main characteristics of CF_{10} (top left), CF_{20} (top right), CF_{30} (bottom left), and CF_{60} (bottom right) values.

As the resulted values show, the magnitude of the correction is greater in longer sampling period cases. This is a logical consequence of the fact that as the sampling period is longer, the high values start to appear as peaks in the plain of the low intensity values, and their effect is longer, since the intervals are longer too. The highest demand of correction can be observed in the plot of the 60-minute data.

The minimum values of CF_t are 1.00. The highest possible correction is influenced by the b exponent. As the value of the exponent b is less than 1.15 for the generally used TBG devices (*Vuerich et al.*, 2009), the maximums of the CF_t values can be calculated. The maximum values are presented in *Table 1*. The magnitude of the possible maximum correction can be significant, but this is a theoretical value, as it was pointed out a little bit earlier, and it can occur in realistic cases rarely.

Table 1. Maximum values of CF_t for various b values and some practical sampling periods

b exponent	**Sampling period**				
	5 min	**10 min**	**20 min**	**30 min**	**60 min**
***b*=1.00**	1.000	1.000	1.000	1.000	1.000
***b*=1.05**	1.084	1.122	1.162	1.185	1.227
***b*=1.10**	1.175	1.259	1.349	1.405	1.506
***b*=1.15**	1.273	1.413	1.567	1.666	1.848

Let us take a look at the averages of the CF_t values of the sample time series. *Table 2* shows the average values of the given sampling periods, in case of $b = 1.042$. For the data of the 5-minute sampling period, the range of high fluctuating CF_t values were excluded, where the measurement showed several consecutive nulls of rainfall intensities, so the maximum value is lower than in *Fig. 1*. As the data show, the average of the CF_t values are relatively low, mainly in the shorter sampling periods. The correction can have significance in the 10-minute sampling periods and over, and mainly if the exponent is greater than 1.10, but for higher sampling periods, the correction can be verified even if the exponent has lower value.

Table 2. Average CF_t values of the sample rainfall with a supposed b=1.042 exponent

***b* exponent**	**Sampling period**				
	5 min	**10 min**	**20 min**	**30 min**	**60 min**
***b*=1.00**	1.000	1.000	1.000	1.000	1.000
***b*=1.05**	1.002	1.009	1.010	1.012	1.021
***b*=1.10**	1.004	1.018	1.022	1.026	1.044
***b*=1.15**	1.007	1.028	1.034	1.040	1.069

The basic question is that in a t sampling period with unknown c_j weights, what is the value of the CF_t. As there are no data for the weights in a realistic case, an estimation is needed, and if it is possible, a generalized value should be used for the corrections in a certain geographic and/or climatic region.

For the determination of a generalized (or generalizable) value for the CF_t, the steadiness of its value is important, both in space and time. For this surmise, some initial hypothesis must be done. The first is that CF_t values can 294haracterize a greater geographic region. This assumption is based on a likely steadiness of the c_j weights, which can be similar in a wider region, independently from the kinds of rainfall, since even and quite varying weight distributions occurs in intensive and less intensive rainfalls, as well. The other hypothesis is that the weight characteristics of the rainfall were steady in time, so the distribution of weights were similar in the past, statistically. This surmise can be right, since there were similar types of rainfalls in the past, and as it was shown, the weights are sensible to the high ratio of the consecutive rainfall intensities, independently from their absolute value. Of course, these statements must be verified with the analysis of a great number of rainfalls in more geographic regions.

4. Conclusion

In the paper, a method was presented as a simple tool for the correction of systematic biases of earlier measured long sampling period rainfall data, recorded by some known type of TBG rainfall gauges, where the sampling period was in the magnitude of 5, 10, 20, 30, and 60 minutes. The procedure was based on mathematical consideration, and the lack of detailed data was managed with the introduction of the generalized correction factor, the GCF_t, which can be calculated from short sampling period rainfall data (one minute), on the base of the supposed steadiness of the weight characteristics of consecutive one-minute rainfall intensities. It can be a good base of the correction presumably for wider geographical regions and longer time domain of measurements, since the method is based on the temporal distribution of weights of rainfall intensities in a unique sampling interval, without using the actual rainfall intensity values. The correction has significance in the 10-minute sampling period data, if the exponent of the correction equation of the TBG gauge is greater than 1.10, and for longer sampling periods, even for values greater than 1.05. The proposed method can help to clear the historical databases to make them a better reference for the investigation of IDF curves, and to make them a better reference for the analysis of the climate change relating to the rainfall intensities, and other parameters.

References

Adami, A. and *Da Deppo, L.*, 1985: On the systematic errors of tipping bucket recording rain gauges. Proc. Int. Workshop on the Correction of Precipitation Measurements, Zurich. 1985. 1–3.

Duchon, C.E. and *Biddle C.J.*, 2010: Undercatch of tipping-bucket gauges in high rain rate events. *Adv. Geosci. 25*, 11–15. https://doi.org/10.5194/adgeo-25-11-2010

Frankhauser, R., 1997: Measurement properties of tipping bucket raingauges and their influence on urban runoff simulation. *Wat. Sci. Tech. 36,* 7–12. https://doi.org/10.2166/wst.1997.0636

Habib, E., Krajewsky, W.K., and *Kruger, A.,* 2001: Sampling errors of tipping bucket rain gauge measurements. *J. Hydraul. Engin.6,* 159–166. https://doi.org/10.1061/(ASCE)1084-0699(2001)6:2(159)

Habib, E., Lee, G., and *Ciah, G.J.*, 2013: Ground-based direct measurement. In Rainfall: The State of Science, Washington: American Geographical Union, 61–78. https://doi.org/10.1029/2010GM000953

Kurytka, J.C. 1953. Precipitation measurements study. Urbana, Illinois, USA: State of Illinois, State Water Survey Division, Dpt of Education and Registration.

Luyckx, G. and *Berlamont, P.,* 2001: Simplified method to correct rainfall measurements from tipping bucket rain gauges. World Water Resources & Environmental Resources Congress, Orlando, 20-24 May 2001. Reston Va. USA: ASCE Publications. https://doi.org/10.1061/40583(275)72

Marsalek, J., 1981: Calibration of tipping-bucket raingage. *J. Hydrol. 53,* 343–354. https://doi.org/10.1016/0022-1694(81)90010-X

Mulvany, T., 1851: On the use of self registering rain and flood gauges in making observations of the relation of rainfall and flood discharges in given catchment. *Trans.Inst.Cio,Engrs.Ire, 4*, 18–33.

Niemczynowicz, J., 1986: The dynamic calibration of tipping bucket raingauges. *Nordic Hydrol. 17*, 203–214. https://doi.org/10.2166/nh.1986.0013

Vuerich, E., Monesi ,C., Lanza, L.G., Stagi, L., and *Lanzinger, E.,* 2009: WMO field intercomparison of rainfall intensity gauges. World Meteorological Organisation. Geneve.

INSTRUCTIONS TO AUTHORS OF *IDŐJÁRÁS*

The purpose of the journal is to publish papers in any field of meteorology and atmosphere related scientific areas. These may be

- research papers on new results of scientific investigations,
- critical review articles summarizing the current state of art of a certain topic,
- short contributions dealing with a particular question.

Some issues contain "News" and "Book review", therefore, such contributions are also welcome. The papers must be in American English and should be checked by a native speaker if necessary.

Authors are requested to send their manuscripts to

Editor-in Chief of IDŐJÁRÁS
P.O. Box 38, H-1525 Budapest, Hungary
E-mail: journal.idojaras@met.hu

including all illustrations. MS Word format is preferred in electronic submission. Papers will then be reviewed normally by two independent referees, who remain unidentified for the author(s). The Editor-in-Chief will inform the author(s) whether or not the paper is acceptable for publication, and what modifications, if any, are necessary.

Please, follow the order given below when typing manuscripts.

Title page should consist of the title, the name(s) of the author(s), their affiliation(s) including full postal and e-mail address(es). In case of more than one author, the corresponding author must be identified.

Abstract: should contain the purpose, the applied data and methods as well as the basic conclusion(s) of the paper.

Key-words: must be included (from 5 to 10) to help to classify the topic.

Text: has to be typed in single spacing on an A4 size paper using 14 pt Times New Roman font if possible. Use of S.I. units are expected, and the use of negative exponent is preferred to fractional sign. Mathematical formulae are expected to be as simple as possible and numbered in parentheses at the right margin.

All publications cited in the text should be presented in the *list of references*, arranged in alphabetical order. For an article: name(s) of author(s) in Italics, year, title of article, name of journal, volume, number (the latter two in Italics) and pages. E.g., *Nathan, K.K.,* 1986: A note on the relationship between photosynthetically active radiation and cloud amount. *Időjárás 90,* 10–13. For a book: name(s) of author(s), year, title of the book (all in Italics except the year), publisher and place of publication. E.g., *Junge, C.E.,* 1963: *Air Chemistry and Radioactivity.* Academic Press, New York and London. Reference in the text should contain the name(s) of the author(s) in Italics and year of publication. E.g., in the case of one author: *Miller* (1989); in the case of two authors: *Gamov* and *Cleveland* (1973); and if there are more than two authors: *Smith et al.* (1990). If the name of the author cannot be fitted into the text: *(Miller,* 1989); etc. When referring papers published in the same year by the same author, letters a, b, c, etc. should follow the year of publication. DOI numbers of references should be provided if applicable.

Tables should be marked by Arabic numbers and printed in separate sheets with their numbers and legends given below them. Avoid too lengthy or complicated tables, or tables duplicating results given in other form in the manuscript (e.g., graphs). *Figures* should also be marked with Arabic numbers and printed in black and white or color (under special arrangement) in separate sheets with their numbers and captions given below them. JPG, TIF, GIF, BMP or PNG formats should be used for electronic artwork submission.

More information for authors is available: journal.idojaras@met.hu

Published by the Hungarian Meteorological Service

Budapest, Hungary

ISSN 0324-6329 (Print)

ISSN 2677-187X (Online)